SILVER NANOPARTICLE-MODIFIED CELLULOSE NANOCRYSTALS FOR FOULING CONTROL IN MEMBRANE DISTILLATION

Josephine Tshepiso Mpala

Student number: 731264

MASTER OF SCINCE

in

School of Chemistry, Faculty of Science, University of the Witwatersrand

Supervisors: Dr. Lebea Nthunya; Dr. Heidi Richards and Dr. Anita Etale

DECLARATION

I declare that this thesis is my own, unaided work. It is being submitted for the Degree of Master of Science at the University of the Witwatersrand, Johannesburg. It has not been submitted before for any degree or examination at any other University.

J.T. Mpala (Signature)

08 day of June 2023 at Wits University

ABSTRACT

A global reduction in water resources and the growing demand for fresh water has motivated the quest for the development of sustainable water-augmenting technologies. Membrane distillation (MD) is envisaged as an attractive desalination technology, surpassing cost challenges faced by conventional desalination technologies. Yet, its industrial commercialization faces multiple limitations, including the production of low water fluxes, membrane wetting and membrane fouling. This study sought to investigate the performance of silver nanoparticles (AgNPs) embedded on cellulose nanocrystals (CNCs) (CNC-capped AgNPs) to lessen the impact of biofouling in MD. This was conducted through coating the polyvinylidene fluoride (PVDF) membrane with CNCcapped AgNPs. Prior to coating with CNC-capped AgNPs, PVDF membrane properties were improved (for MD suitability) through blending with polyvinylpyrrolidone (PVP) and functionalized carbon nanotubes (f-CNTs). The resulting membrane had an improved overall porosity, and a respective increase in surface roughness (75%) and mechanical strength (45%). Pristine CNC-capped AgNPs' characterization presented stable AgNPs with minimal leaching. Transmission electron microscopy (TEM) micrographs revealed a uniform dispersion of spherically shaped AgNPs exhibiting 13.3 ± 3.4 nm average diameter. The presence of AgNPs on the surface of CNCs afforded excellent thermal stability and good anti-microbial activity, mainly against E. coli, P. aeruginosa, S. aureus, S. epidermis, and S. saprophyticus. Following membrane modification, preliminary anti-bacterial tests conducted on the CNC/AgNP-modified PVDF membrane revealed a 98.7%, 52.3%, 78.0%, 53.9% and 93.3% reduction of E. coli, P. aeruginosa, S. aureus, S. epidermis, and S. saprophyticus cells, respectively, demonstrating its ability to control biofouling. Although the CNC/AgNP-modified PVDF membrane exhibited improved membrane properties, such as high surface roughness, high liquid entry pressure (LEP), and good hydrophobicity, its performance in MD (with artificial seawater as the feed stream) was poor, producing the lowest average water flux (0.179 ± 0.0303 kg/m2 /hr) compared to the unmodified PVDF membrane (0.528 ± 0.0838

kg/m2 /hr), mainly due to pore blockage. However, upon spiking the artificial seawater with a monoculture of *G. Stearothermophilus*, the CNC/AgNP-modified PVDF membrane displayed the most stable water flux while the unmodified PVDF membrane's water flux decreased by 79.3% over the 24-hour (h) period. This was attributed to the formation of a biofouling layer on the PVDF membrane which was absent on the CNC/AgNP-modified PVDF membrane. The AgNPs on the surface of the membrane afforded minimal bacterial deposition during operation. These results ascertain the possibility of biofouling minimization in MD using CNC-capped AgNPs, contributing to MD's body of work for its ultimate realization for up-scaling.

DEDICATION

I dedicate this dissertation to my late aunt, Rakgadi Tiny Mabel Ntlatleng, for upholding our family with love and humility.

“Forever in our hearts.”

ACKNOWLEDGEMENTS

Immense appreciation firstly to God for His tremendous mercy and love. He carried me through and provided health, strength, and wisdom. Thank you to my supervisors; Dr Lebea, Dr Heidi, and Dr Anita – for affording me the opportunity to become a part of the analytical and environmental chemistry group, for providing technical assistance and for offering support. I will always be thankful for the time I spent and the overall impact it had. A special thank you to Dr Lebea for assisting step by step and showing the way. This work would not have been half its quality without his input. Massive gratitude to Dr Heidi and Dr Anita as well, for offering well-thoughtful suggestions. Immense thanks to Prof Hope from UJ for opening the doors of her lab for us to do our microbial work.

A special thanks to Indira for the insightful and enlightening chats around our work in the lab. Massive thank you as well to the postgraduates within our research group for assistance and motivation. A special thanks to Ms. Mokgaetji for assistance with safety assurance in the lab and equipment training and to Dr. Oranso Mahlangu from UNISA for assistance with membrane characterization. Thank you to the MMU department for assistance during characterization. Lastly, thank you to the School of Chemistry and Wits University for affording me the opportunity to complete my studies.

I remain eternally grateful to my parents for their support, the patience, and the love that they have shown me throughout my life. Embarking on an MSc journey would have remained a dream without them. To my sister, Dineo, who's words of affirmation became my strength, words are not enough. I want to thank her for offering an ear to listen when I needed it. To the Mpala and Ntlatleng clan – my maternal and paternal – it takes a village, and I am immensely grateful for everything. A titanic thank you to my best friends, Lerato and Uni, for being my biggest cheerleaders. I want to thank them for encouraging me to do this degree and for being my inspiration. Massive thank you to the National Research Foundation (NRF) for providing financial assistance.

PUBLICATIONS AND PRESENTATIONS

List of presentations:

July 2022 – Gradflash presentation: Silver nanoparticle-modified cellulose nanocrystals for fouling control in membrane distillation, Cross Faculty Symposium, Wits University.

September 2022 – Poster presentation: Silver nanoparticle-modified cellulose nanocrystals for fouling control in membrane distillation, MSc poster presentations, Wits University.

List of publications:

Published:

Tshepiso J. Mpala, Heidi Richards, Anita Etale and Lebea N. Nthunya. Biofouling phenomena in membrane distillation: mechanisms and mitigation strategies. *Environmental Science Advances.* **2022**; DOI: 10.1039/d2va00161f. A review article forming part of Chapter 2.

Tshepiso J. Mpala, Heidi Richards, Anita Etale, Hope Serepa-Dlamini and Lebea N. Nthunya. Cellulose nanocrystal-mediated synthesis of silver nanoparticles via microwave assisted method for biofouling control in membrane distillation. *Materials today communications.* **2022**; 34, 105028. A research article forming part of Chapter 3 and 4.

Submitted:

Tshepiso J. Mpala, Heidi Richards, Anita Etale, Oranso T. Mahlangu, and Lebea N. Nthunya. Preparation of nanoparticle enhanced PVDF membrane for improved performance in membrane distillation*. Frontiers in membrane science and technology.* A research article forming part of Chapter 5.

In press:

Tshepiso J. Mpala, Heidi Richards, Indira Chimanlal, Anita Etale, and Lebea N. Nthunya. Hybrid membrane processes equipped with a crystallization unit for the simultaneous recovery of freshwater and minerals from saline wastewater. A book chapter forming part of a book titled*: "Innovative trends in removal of Refractory pollutants from Pharmaceutical wastewater*." *Elsevier*

In preparation:

Tshepiso J. Mpala, Heidi Richards, Anita Etale, Oranso T. Mahlangu, and Lebea N. Nthunya. Biofouling control in membrane distillation using CNC/AgNP- modified PVDF membranes. *In preparation.* A research article forming part of Chapter 6.

TABLE OF CONTENTS

LIST OF FIGURES

LIST OF TABLES

LIST OF ABBREVIATIONS

PVDF – Polyvinylidene fluoride

PVP – Polyvinyl pyrrolidone

CNCs – Cellulose nanocrystals

AgNPs – Silver nanoparticles

MD – Membrane distillation

DCMD – Direct contact membrane distillation

RO – Reverse Osmosis

LEP – Liquid entry pressure

TP – Temperature polarization

CP – Concentration polarization

PTFE – Polytetrafluoroethylene

PP – Polypropylene

MWCNTs – Multi-walled carbon nanotubes

POTS – 1H, 1H, 2H, 2H-perfluoro-octyltriethoxysilane

f-CNTs – Functionalized carbon nanotubes

NIPS – Non induced phase inversion

EPS – Extracellular polymeric substance

SLM – Soluble microbial products

MNPs – Metal nanoparticles

FTIR – Fourier transform infrared spectroscopy

TEM – Transmission electron microscopy

SEM – Scanning electron microscopy

AFM – Atomic force microscopy

XRD – X-ray diffraction

ICP-MS – Inductively coupled plasma – mass spectroscopy

Chapter 1: Introduction

1.1 Background and motivation

The demand for potable water is predicted to exceed supply by 2030 (Prins *et al.*, 2022), a projection necessitating the development of well-thoughtful water-augmenting strategies. The importance of water accessibility stems from its ability to enhance economic growth and advance agricultural activities, which have a direct impact on food security (Liu, 2022). Moreover, the basic survival of a human being requires freshwater (White *et al.*, 2010). However, freshwater accessibility is deteriorating at an alarming rate (Wang *et al.*, 2019). It is estimated that about 2.7 billion people are affected by this deterioration annually (Barrios *et al.*, 2020). According to a study by Giri *et al.,* (2022), diarrhea caused by inadequate clean water and sanitation is a major cause of death among children. Worse, predictions by the world bank project a water deficit (in 2050) where approximately 5 billion people in developing countries will be affected (Dhakal *et al.*, 2022). Therefore, global urgent responses are required to tackle water related challenges.

Currently, strategies presented to lessen the impact of water shortage include saving water, increasing water reuse, transporting water to semi-arid areas and desalination (recovery of fresh water from seawater). Although desalination is considered the last resort owing to its high cost of operation; its independence on climate change, river flows and reservoir levels has enhanced its advancement in research and development (Dhakal *et al.*, 2022). As of 2022, the total desalination capacity is estimated to be 115 Mm^3/d (Dhakal *et al.*, 2022). Desalinations' consideration for application is further enhanced by the abundance of seawater (Castro-Muñoz, 2020). In particular, seawater constitutes 97% of the total water on earth (Biswas, 2016). The remaining 3% constitutes freshwater, with 1.74% accounting for water locked up in glaciers/ice-caps and 1.75% accounting for water in lakes, rivers and groundwater (Balasubramanian, 2015). Through desalination, independent remote areas near the coast can be supplied with fresh water (Schwantes *et al.*, 2013). Several techniques aimed at seawater desalination exist,

including reverse osmosis (RO), multi effect distillation (MED), multi stage flash (MSF), and membrane distillation (MD), amongst others (Nthunya *et al.*, 2022). The main drawback of RO includes overcoming the hurdle of disposing brine concentrates in the environment, which pollute existing water systems and impact negatively on fauna and flora, especially in regions on the coast (Kiefer, Präbst and Sattelmayer, 2019). Given the need to meet global environmental integrity and zero liquid discharge (ZLD), thermal desalination technologies have emerged, including MD, MED and MSF (Ruiz-Aguirre, Andrés-Mañas and Zaragoza, 2019). While MED and MSF are able to treat highly concentrated brine, MD is reported to exhibit better energy efficiency compared to the two (Choudhury *et al.*, 2019). In addition, MD exhibits less sensitivity to the concentration of solutes in the feed solution (due to its driving force), achieves exceptional separation efficiencies (>99%) and requires moderate conditions (i.e., pressure) for operation (Alkhudhiri *et al.,* 2012; Lalia *et al.*, 2014). Indeed, MD displays superior features. The implications of a MD system operating under moderate conditions include the possibility of commercializing a decentralized system due to a decrease in system complexity (Bogler and Bar-Zeev, 2018). In addition, less rigid membrane mechanical properties are required (Liu, Zhu and Chen, 2020b). With MD, alternative energy sources such as solar energy and geothermal energy can be considered for use during operation (Sarbatly and Chiam, 2013; Guillen-Burrieza *et al.*, 2014). Factors affecting seawater desalination in MD include: (1) hydrodynamic conditions of the system, (2) feed solution properties, and (3) membrane properties.

MD achieves freshwater recovery through the use of a hydrophobic/microporous membrane, where volatile substances are transferred from the feed compartment to the distillate compartment across the membrane (Teoh *et al.*, 2021). Membranes often require modification to operate optimally, with substantial work being done on certain nanoparticles (NPs) to exploit them for use during membrane modification. CNTs are NPs consisting of rolled-up sheets of graphene and are largely used during membrane synthesis due to their high mechanical strength and excellent aspect ratio (Gao *et al.*, 2020). CNTs are further able to lower membrane surface energy when surface

functionalized with fluorosilanes. This is because these have low surface tension and low polarity (Zheng *et al.*, 2016). This work involved the use of CNTs during PVDF synthesis.

The main drawback of a hydrophobic membrane during MD operation is the tendency for membrane fouling, which refers to the adherence of unwanted contaminants on the membrane surface and within its pores (Tripathi, 2020). Amongst other fouling types, microbial accumulation (i.e., biofouling) has proven to be the most intricate and the severest, inducing biofilm development through elaborate pathways (Bogler, Lin and Bar-Zeev, 2017). Little has been known about biofouling in MD through the years as minimal microbial deposition was anticipated, given the high temperatures and the high saline conditions under which the system operates (Liu, Zhu and Chen, 2020a). However, reports of biofouling in MD have been on the rise and have attracted significant research attention (Costa *et al.*, 2021).

1.2 Problem statement

Challenges associated with biofouling include considerable microbial deposition on the surface of the membrane, leading to the formation of a biofilm. Biofilms cause a severe irreversible reduction in water flux through impeding the maximum transfer of the vapor produced, largely as a result of an increase in the restriction of flow (Bogler, Lin and Bar-Zeev, 2017). Moreover, these microbial contaminants pollute the distillate stream. The production of extracellular polymers (EPS) by bacteria following microbial adsorption cause a decrease in membrane hydrophobicity, inducing membrane wetting and a subsequent decrease in the salt rejection efficiency (Bogler and Bar-Zeev, 2018). According to previous reports, operational costs are increasingly affected by biofouling (Wang *et al.*, 2019; Jafari *et al.*, 2021). A rise in energy consumption has been witnessed when the driving force (i.e., vapor pressure) in MD plummets due to biofouling. Therefore, the large scale application of MD has been limited by biofouling, among other factors (Krivorot *et al.*, 2011). With an increase in efficiency losses and a reduction in membrane lifespan, biofouling eradication has become a key research concern. This project focused on the exploitation of an environmentally benign and renewable resource, cellulose, to

immobilize AgNPs on PVDF to prevent microbial deposition and accumulation. Limiting biofouling in MD will ensure that higher fluxes are realized, and pure freshwater is recovered.

1.3 Aims and Objectives

The main aim of this study was to investigate the performance of CNC-capped AgNPs embedded on the PVDF membrane for biofouling resistance in MD. This was achieved through small work packages, each related to a specific objective:

1. Synthesis and characterization of CNC-capped AgNPs
2. Synthesis and characterization of flat sheet pristine and modified PVDF membranes
3. Preliminary assessment of the antimicrobial properties of CNC-capped AgNPs and CNC/AgNP-modified PVDF membrane
4. Assessment of the performance of flat sheet pristine and modified PVDF membranes towards biofouling minimization in a laboratory-scale MD system.

1.4 References

1. Balasubramanian, A. (2015) ‘the World ’ S Water Crisis’, *Research Gate*, 44(0).
2. Alkhudhiri, A., Darwish, N. and Hilal, N. (2012) ‘Membrane distillation: A comprehensive review’, *Desalination*, 287, pp. 2–18. doi: 10.1016/j.desal.2011.08.027.
3. Barrios, A. C. *et al.* (2020) ‘Prolonging the antibacterial activity of nanosilver-coated membranes through partial sulfidation’, *Environmental Science: Nano*, 7(9), pp. 2607–2617. doi: 10.1039/d0en00300j.
4. Biswas, A. K. (2016) ‘Water Availability and Use’, *Water Resources of North America*, (April 2018), pp. 163–174. doi: 10.1007/978-3-662-10868-0_19.
5. Bogler, A. and Bar-Zeev, E. (2018) ‘Membrane Distillation Biofouling: Impact of

Feedwater Temperature on Biofilm Characteristics and Membrane Performance', *Environmental Science and Technology*, 52(17), pp. 10019–10029. doi: 10.1021/acs.est.8b02744.

6. Bogler, A., Lin, S. and Bar-Zeev, E. (2017) 'Biofouling of membrane distillation, forward osmosis and pressure retarded osmosis: Principles, impacts and future directions', *Journal of Membrane Science*, 542, pp. 378–398. doi: 10.1016/j.memsci.2017.08.001.
7. Castro-Muñoz, R. (2020) 'Breakthroughs on tailoring pervaporation membranes for water desalination: A review', *Water Research*, 187, p. 116428. doi: 10.1016/j.watres.2020.116428.
8. Choudhury, M. R. *et al.* (2019) 'Fouling and wetting in the membrane distillation driven wastewater reclamation process – A review', *Advances in Colloid and Interface Science*, 269, pp. 370–399. doi: 10.1016/j.cis.2019.04.008.
9. Costa, F. C. R. *et al.* (2021) 'Biofouling in membrane distillation applications - a review', *Desalination*, 516(July). doi: 10.1016/j.desal.2021.115241.
10. Dhakal, N. *et al.* (2022) 'Is Desalination a Solution to Freshwater Scarcity in Developing Countries ?', (Figure 1), pp. 1–15.
11. Gao, C. *et al.* (2020) 'Superhydrophobic electrospun PVDF membranes with silanization and fluorosilanization co-functionalized CNTs for improved direct contact membrane distillation', *Engineered Science*, 9, pp. 35–43. doi: 10.30919/es8d905.
12. Giri, M. *et al.* (2022). 'Water, Sanitation, and Hygiene Practices and Their Association With Childhood Diarrhoea in Rural Households of Mayurbhanj District, Odisha, India', *Cureus*, *14*(10). https://doi.org/10.7759/cureus.29888.
13. Guillen-Burrieza, E. *et al.* (2014) 'Membrane fouling and cleaning in long term plant-scale membrane distillation operations', *Journal of Membrane Science*, 468, pp. 360–372. doi: 10.1016/j.memsci.2014.05.064.
14. Jafari, M. *et al.* (2021) 'Cost of fouling in full-scale reverse osmosis and nanofiltration installations in the Netherlands', *Desalination*, 500, p. 114865. doi: 10.1016/j.desal.2020.114865.

15. Kiefer, F., Präbst, A. and Sattelmayer, T. (2019) ‘Membrane scaling in Vacuum Membrane Distillation - Part 2: Crystallization kinetics and process performance’, *Journal of Membrane Science*, 590, pp. 1–10. doi: 10.1016/j.memsci.2019.117293.
16. Krivorot, M. *et al.* (2011) ‘Factors affecting biofilm formation and biofouling in membrane distillation of seawater’, *Journal of Membrane Science*, 376(1–2), pp. 15–24. doi: 10.1016/j.memsci.2011.01.061.
17. Lalia, B. S. *et al.* (2014) ‘Nanocrystalline cellulose reinforced PVDF-HFP membranes for membrane distillation application’, *Desalination*, 332(1), pp. 134–141. doi: 10.1016/j.desal.2013.10.030.
18. Liu, C., Zhu, L. and Chen, L. (2020a) ‘Biofouling phenomenon of direct contact membrane distillation (DCMD) under two typical operating modes: Open-loop mode and closed-loop mode’, *Journal of Membrane Science*, 601. doi: 10.1016/j.memsci.2020.117952.
19. Liu, C., Zhu, L. and Chen, L. (2020b) ‘Effect of salt and metal accumulation on performance of membrane distillation system and microbial community succession in membrane biofilms’, *Water Research*, 177, p. 115805. doi: 10.1016/j.watres.2020.115805.
20. Liu, X. (2022) ‘Global Agricultural Water Scarcity Assessment Incorporating Blue and Green Water Availability Under Future Climate Change Earth ’ s Future’. doi: 10.1029/2021EF002567.
21. Nthunya, L. N. *et al.* (2022) ‘Fouling, performance and cost analysis of membrane-based water desalination technologies: A critical review’, *Journal of Environmental Management*, 301, p. 113922. doi: 10.1016/j.jenvman.2021.113922.
22. Prins, F. X. *et al.* (2022) ‘Water scarcity and alternative water sources in South Africa: can information provision shift perceptions?’, *Urban Water Journal*, 00(00), pp. 1–12. doi: 10.1080/1573062X.2022.2026984.
23. Ruiz-Aguirre, A., Andrés-Mañas, J. A. and Zaragoza, G. (2019) ‘Evaluation of distillate quality in pilot scale membrane distillation systems’, *Membranes*, 9(6), pp. 1–14. doi: 10.3390/membranes9060069.

24. Sarbatly, R. and Chiam, C. K. (2013) ‘Evaluation of geothermal energy in desalination by vacuum membrane distillation’, *Applied Energy*, 112, pp. 737–746. doi: 10.1016/j.apenergy.2012.12.028.
25. Schwantes, R. *et al.* (2013) ‘Membrane distillation: Solar and waste heat driven demonstration plants for desalination’, *Desalination*, 323, pp. 93–106. doi: 10.1016/j.desal.2013.04.011.
26. Teoh, G. H. *et al.* (2021) ‘Impacts of PVDF polymorphism and surface printing micro-roughness on superhydrophobic membrane to desalinate high saline water’, *Journal of Environmental Chemical Engineering*, 9(4), p. 105418. doi: 10.1016/j.jece.2021.105418.
27. Tripathi, B. P. (2020) ‘Encyclopedia of Membranes’, *Encyclopedia of Membranes*, pp. 1–3. doi: 10.1007/978-3-642-40872-4.
28. Wang, Wenyi *et al.* (2019) ‘Palygorskite/silver nanoparticles incorporated polyamide thin film nanocomposite membranes with enhanced water permeating, antifouling and antimicrobial performance’, *Chemosphere*, 236, p. 124396. doi: 10.1016/j.chemosphere.2019.124396.
29. White, M. *et al.* (2010) ‘Blue space: The importance of water for preference, affect, and restorativeness ratings of natural and built scenes’, *Journal of Environmental Psychology*, 30(4), pp. 482–493. doi: 10.1016/j.jenvp.2010.04.004.
30. Zheng, L. *et al.* (2016) ‘Preparation of PVDF-CTFE hydrophobic membranes for MD application: Effect of LiCl-based mixed additives’, *Journal of Membrane Science*, 506, pp. 71–85. doi: 10.1016/j.memsci.2016.01.044.

Chapter 2: Literature Review

In this chapter, an in-depth review of MD is given as well as its application in water purification. First, the history of MD and its mechanism of operation is presented, followed by conditions under which separation occurs and the pressing concerns around membrane biofouling. Later, literature relating to solutions regarding biofouling prevention are offered.

2.1 Membrane distillation

The process of MD was originally described and patented in 1963 by Bodell, with no presentation of quantitative data (Bodell, 1968). Having developed an apparatus that could circulate brine water and produce distillate vapor, Bodell's idea of the "structure" that was liquid impermeable and vapor permeable was unclear (Lawson & Lloyd, 1997). The discovery of a porous hydrophobic membrane was reported by Weyl, (1967), proposing that the minimization of energy consumption was possible by means of directly contacting the feed solution and distillate solution with a hydrophobic membrane. Reportedly, water fluxes reaching 1 kg m^{-2} h^{-1} were attained. However, MD water fluxes remained critically low compared to the widely explored RO desalination processes (70 kg m^{-2} h^{-1}), causing the technique to lose traction (Lawson & Lloyd, 1997). It was only in the late 1980s that the availability of a hydrophobic membrane that exhibited better properties was attained (Nakoa, Date and Akbarzadeh, 2015). Subsequently, MD research grew exponentially, displaying major advances in its configurations (El-Bourawi *et al.*, 2006).

Currently, four different MD configurations have been reported, depending on how water vapor is treated on the distillate side following production. These include air gap membrane distillation (AGMD), sweep gas membrane distillation (SGMD), vacuum membrane distillation (VMD) and direct contact membrane distillation (DCMD) (Eykens *et al.*, 2016). DCMD remains the most widely used configuration (Choi *et al.*, 2019),

involving a direct contact of the hydrophobic membrane with the heated feed solution and the cold distillate (Jiang *et al.*, 2017). With DCMD, the water fluxes generated are more stable, especially compared to VMD (Drioli, Ali and Macedonio, 2015). However, DCMD suffers from massive conductive heat loss, hampering its industrial application. To reduce energy loss, an air gap was introduced into the system, establishing high energy savings with, however, significantly lower fluxes (Eykens *et al.*, 2016). In terms of the mechanism of operation, vapor generated from the vapor pressure difference existing across the membrane gets transported to the distillate side where it condenses to form pure water. As illustrated in **Figure 2.1**, both mass (vapor) and heat are transferred though the hydrophobic membrane. The mechanism of mass transport occurs through Poisseuille flow, molecular diffusion, and Knudsen diffusion, conditional to the existence of trapped air in the pores and the membrane pore size (Khayet, 2011). Mass transport depends on the concentration of the feed solution, the mass transfer coefficient, the type of membrane used and its properties.

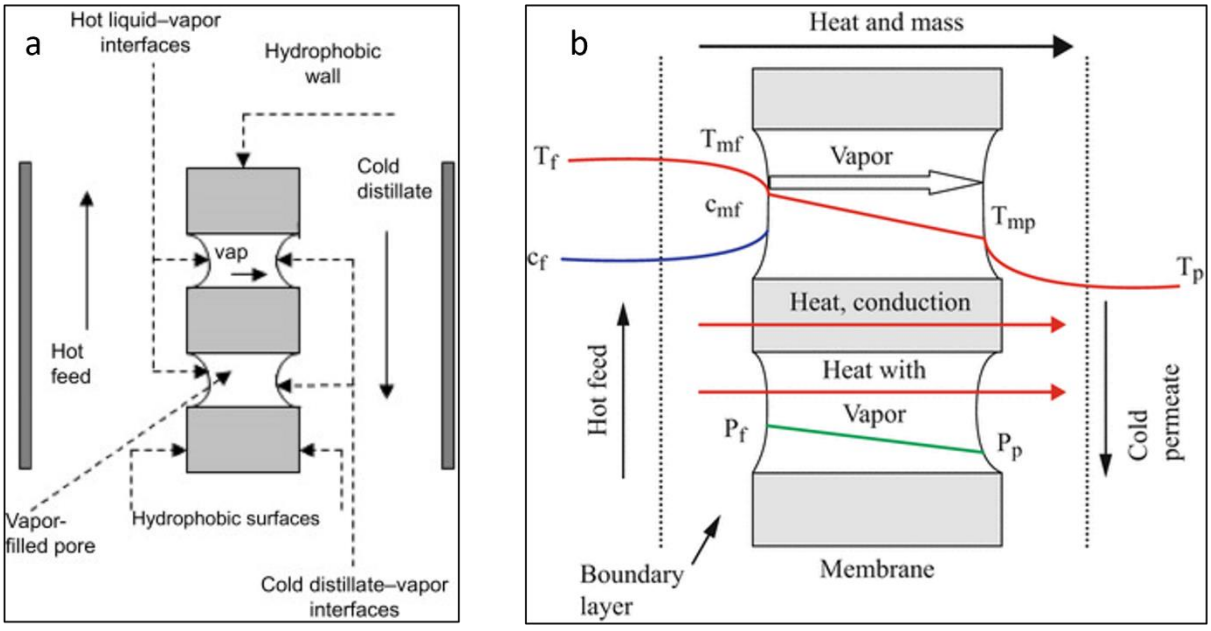

Figure 2.1: Mechanism of operation of MD: (a) process mechanism and (b) heat and mass transfer, where Tf, Tmf, Tmp and Tp represent temperatures of the feed solution in

the tank, near the membrane surface, the distillate solution in the tank and near the membrane surface, respectively. Pf, Pp represent the partial pressures on the feed side and the distillate side and cf, cmf represent feed solution concentrations in the tank and near the membrane surface, respectively (Tomaszewska, 2020).

Membranes used in MD include PVDF, polytetrafluoroethylene (PTFE) and polypropylene (PP) (Hou *et al.*, 2014). The widespread application of PVDF in MD stems from its advantages including mechanical, thermal and chemical stability, as well as its beneficial dissolution in a wide variety of solvents (Lai *et al.*, 2014). PVDF consists of 59.4 wt% fluorine and 3 wt% hydrogen (Dohany, 2000), with 35% - 70% crystallinity. Fluorinated polymers generally have high thermal stability over their hydrocarbon counterparts, largely due to the highly electronegative fluorine atom (Liu *et al.*, 2011).

Although MD displays attractive features, it is its ability to use residual heat that continues to heighten its advancement in research (Choi *et al.*, 2019). A study by Schwantes *et al.*, (2013) coupled MD operation (pilot-scale) with a diesel power station, where residual heat from cooling circuits of the diesel power station was utilized to heat the MD feed stream. During MD operation, temperatures of up to 70ºC-80ºC could be obtained throughout a 24-hour day, with MD producing about 4 m^3 of water per day. The utilization of residual heat was found to be energy-saving and cost-effective. One significant limitation of MD application is the tendency for membrane fouling (Drioli, Ali and Macedonio, 2015). Membrane fouling is reported to increase membrane wetting, causing a reduction in the quality of the distillate stream (Chew, Krantz and Fane, 2014). Moreover, membrane fouling introduces regular membrane cleaning and frequent membrane replacements, further increasing costs of water production (Shirazi, Lin and Chen, 2010).

Current studies reported in literature mostly focus on inorganic and organic fouling, with limited information available pertaining to the dynamics and succession of biofouling (Liu, Zhu and Chen, 2020a). By definition, biofouling refers to the deposition and accumulation of microorganisms on the surface of the membrane and within its pores, leading to the formation of a biofilm (Zahid *et al.*, 2021). The biofilm consists of microbial cells and

extracellular polymeric substances (EPS), covering the surface of the membrane. A study by Zodrow *et al*.,(2014) investigated the initial stages of biofilm formation in MD and RO. Waters collected during the autumn season had greater amounts of EPS, dead bacteria, and nutrients than waters collected during winter. Consequently, a 50% decline in water flux was observed in the first 12 h of MD operation. This was attributed to the high nutrients present in the feed solution which were not removed though pre-treatment via microfiltration (10 µm pores). Elucidating the mechanism and effects of biofouling and biofilm development in MD is highly imperative as it will ensure a sustained operation of MD over long periods of time. The latter part of this Chapter will cover biofilm development, its implications on performance and its mitigation.

2.2 Biofilm development pathway

Biofilm formation follows a pathway of successive steps including (1) conditioning film formation with the migration and adhesion of bacterial cells to the membrane surface, (2) EPS secretion with the growth/maturation of bacterial cells, and (3) proliferation and cell detachment for the colonization of new areas (Aslam, Ahmad and Kim, 2018). Enumeration of bacterial cells on the membrane surface will be further highlighted as well as predominant microbial cells responsible for initiating biofouling in MD.

2.2.1 Conditioning film formation and surface attachment

A conditioning film composed of macromolecules, organic matter, proteins, amino acids, and nucleic acids initially cover the surface of the membrane. Concomitantly, dead bacteria and soluble microbial products (SMP's) capable of surface adsorption adhere on the surface. The presence of the conditioning film alters the membrane surface, promoting better adhesion of cells (Petrova and Sauer, 2012). Planktonic (free-floating) cells migrate from the bulk solution to the membrane surface though the Brownian motion, where movement is induced by the collision of particles (**Figure 2.2**) (Guo *et al.*, 2022). Attachment is not permanent, as planktonic cells preferentially select sites for adhesion

though cell locomotion using flagella and pili (Uneputty *et al.*, 2022). Cells exhibiting better motility and better microbial activity attach first on membrane surfaces (Zheng *et al.*, 2022).

Following attachment, cells undergo proliferation, where constant multiplication and division takes place. The interaction between cells and the membrane (cell-to-surface) occur largely though electrostatic and hydrophobic-hydrophobic interactions (Zhang *et al.*, 2018). Although positively charged bacterial cells adhere readily on membrane surfaces, negatively charged bacterial cells tend to adhere less, especially in cases where the membrane surface is predominantly negatively charged and the ionic strength of the feed solution is low (Hori and Matsumoto, 2010). Solutions of low ionic strength contain less ions to counter-act the electronegativity of bacterial cells, resulting in increased repulsion between the membrane and the cell. However, at high ionic strength, cells adhere readily and irreversibly on membrane surfaces. Abu-Lail & Camesano, (2003) evaluated the bio-adhesion of *Pseudomonas putida KT2442* and noted low adhesion rates at low ionic strength. This was attributed to the high energy barrier that was required to be overcome for adhesion to take place, a theory best described by the Derjaguin–Landau–Verwey–Overbeek (DLVO) theory (Adair, Suvaci and Sindel, 2001).

From a hydrophobic-hydrophobic interaction perspective, hydrophobic surfaces tend to adsorb hydrophobic microorganisms. In particular, bacteria contain hydrophobins (also known as adhesins), which promote adhesion and the formation of the conditioning layer, responsible for initiating biofilm development (Bogler, Lin and Bar-Zeev, 2017). In the same space, bacteria that are predominantly hydrophilic tend to adsorb on hydrophilic surfaces. However, bacteria generally adsorb more on hydrophobic than hydrophilic surfaces (Bogler *et al*., 2017). Maikranz *et al.*, (2020) studied the binding mechanism of *Staphylococcus aureus* on hydrophilic and hydrophobic surfaces. It was noted that many macromolecules tethered on hydrophobic surfaces while a few macromolecules tethered on hydrophilic surfaces. This was attributed to the cell-surface contact time and adhesion force. It was further stated by Fabre *et al.*, (2018) that the adhesion of protein (precursor of bacterial adhesion) occurs in low amounts and less tightly on hydrophilic surfaces than

hydrophobic surfaces. It is important to note that full assurance of absolute adherence/non-adherence of cells is complicated as bacteria exhibit endless mechanisms that enable their adaptation under different conditions (Luan *et al.*, 2018).

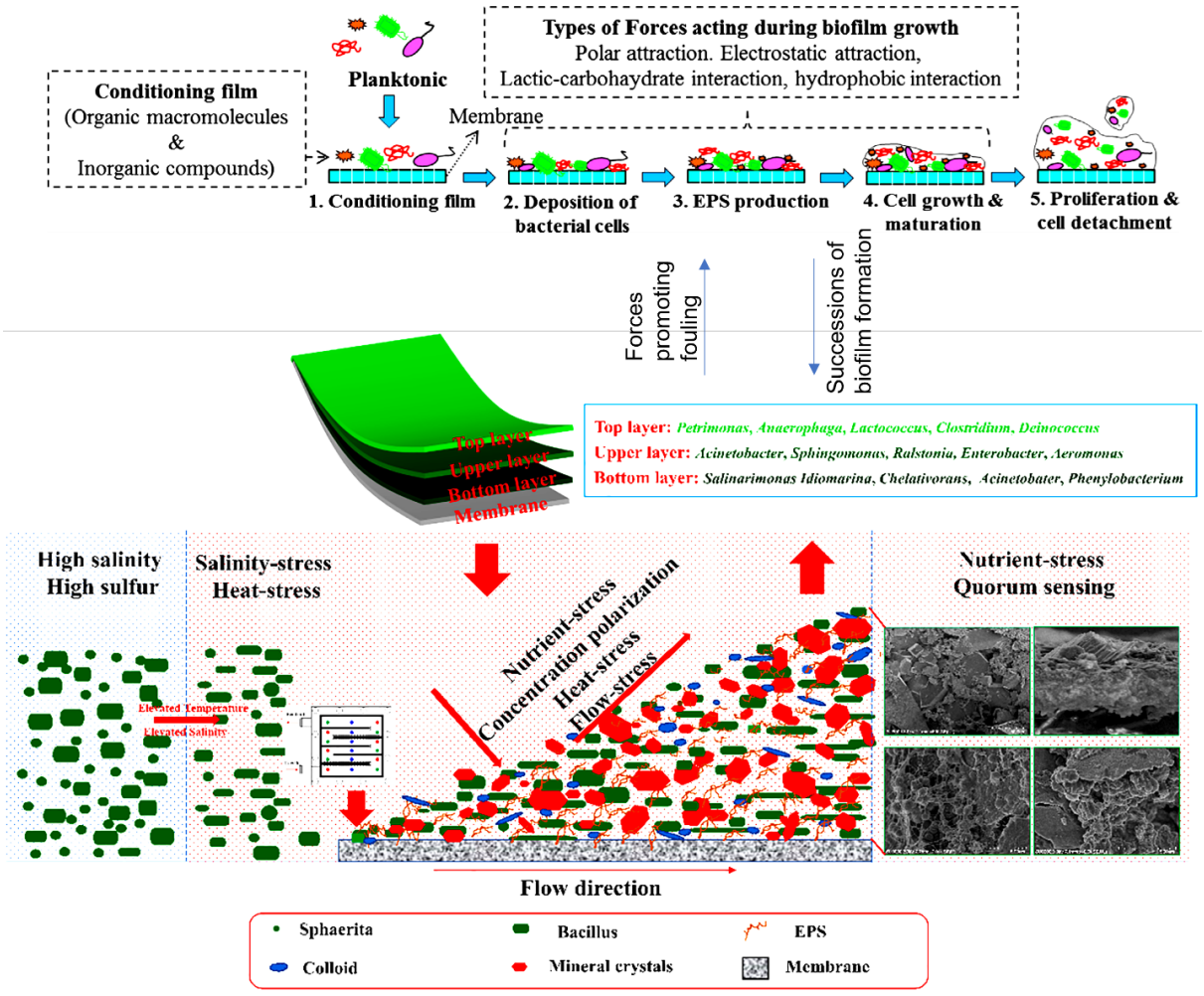

Figure 2.2: Mechanistic relationship of the heat, nutrient, and flow stress on the distribution of bacteria on membrane surfaces during MD operation (Aslam, Ahmad and Kim, 2018; Zheng *et al.*, 2022)

2.2.2 Biofilm stability and EPS secretion

Following attachment and proliferation, bacterial cells secrete EPS and together, essentially constitute the biofilm (**Figure 2.3**). The biofilm forms between the solid and the liquid phase, where ultimate separation takes place. EPS tend to immobilize and encapsulate bacterial cells, enhancing the firmness of the biofilm. The biofilm structure contains interstitial water channels, facilitating the movement of oxygen, nutrients, and genetic material (Bogler, Lin and Bar-Zeev, 2017). Bacteria are usually larger than other biofilm microorganisms and typically range from 0.5 – 2 µm (Hori and Matsumoto, 2010). Movement of bacteria though the biofilm results in the colonization of new areas.

EPS vary in terms of composition, but mainly contain polysaccharides, lipoproteins, proteins, glycoproteins, and carbohydrates (Manzoor *et al.*, 2022). Contributing towards bacteria resistance against inhibitors, EPS further bind the cells to the surface. EPS are capable of enhancing communication within cells and act as a source of nutrients for the bacteria (Costa *et al.*, 2021). Bacteria are known to release significant EPS under thermal stress, making EPS production during MD operation highly favorable (Zheng *et al.*, 2022). Notably, different biofilm layers contain different pore-size distributions. Goh *et al.,* (2013) used evapoporometry to study the particle-size distribution of the biofilm layer caused by two sludge solutions of different hydrophobicity's. Reportedly, the hydrophilic sludge containing smaller pores was responsible for vapor pressure reduction. The depression of vapor pressure was attributed to the Kelvin effect rather than the effect of an increase in hydraulic resistance.

During biofilm development, bacteria can sense each other within the vicinity, a process known as quorum sensing (QS). Bacteria secrete autoinducers during QS development, enhancing bacteria communication (Tabraiz *et al.*, 2021). QS further promotes microbial social activities and enhance community behavior though the expression of certain genes (Pagliero *et al.*, 2021). The dispersion of the biofilm is augmented by QS (Ruhal and Kataria, 2021). Thus, QS further encourages biofilm development. In a study by *Zheng et al.,* (2022), the development and succession of the microbial community was exerted by

QS, amongst other factors. The obstinacy of biofilm development and EPS secretion has deemed membrane biofouling a key research concern.

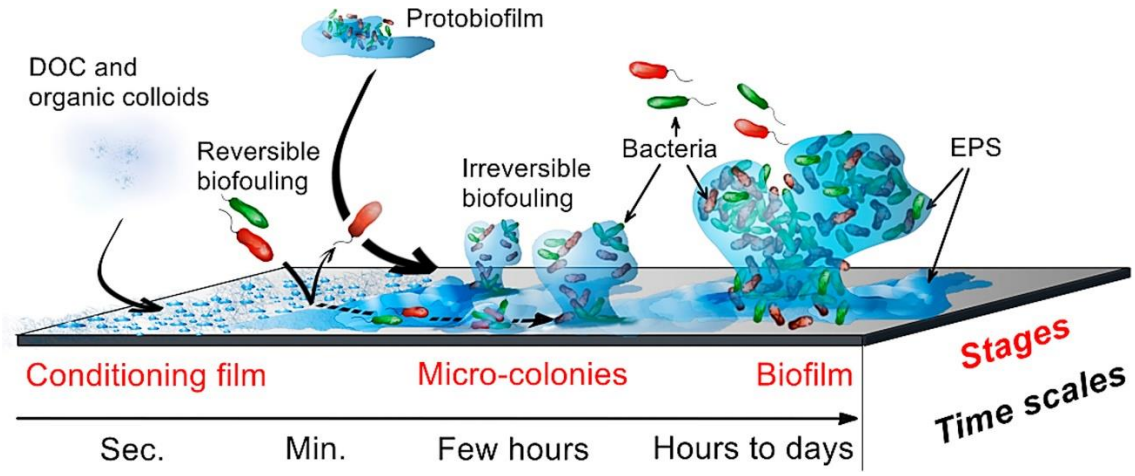

Figure 2.3: Biofilm progression in MD (Bogler, Lin and Bar-Zeev, 2017)

2.3 Enumeration and identification of microbial cells on the membrane surface

Biofilm identification and characterization on the membrane surface is conducted using a variety of techniques including scanning electron microscopy coupled with energy dispersive spectroscopy (SEM-EDS), optical coherence tomography (OCT) and confocal laser scanning microscopy (CLSM) (Yoon *et al.*, 2013; Valladares Linares *et al.*, 2014). Zodrow *et al*., (2014) evaluated membrane biofilm formation using CLSM, assessing the architecture, heterogeneity and biovolume of the microbial community. The biofilms were heterogeneous and contained several colonies, with a plethora of *Burkholderiales*, *Rhodobacterales*, and *Flavobacteriales*. Bogler & Bar-Zeev, (2018) identified the presence of polysaccharides and detected dead and live bacterial cells using CLSM, with a further evaluation of the average biofilm thickness and total biovolume. Krivorot *et al.,* (2011) evaluated the progression of biofilm development (over-time) on the membrane surface using SEM. The experiment was conducted over a period of 19 days and the

deposition of microbial cells increased qualitatively as a function of time. Initial bacterial attachment was detected after 28 h, with the conditioning film seen only after 20 h of operation. In 48 h, the biofilm had formed and over the next 19 days, biofilm coverage on the membrane surface increased. This later caused a reduction in process performance.

The use of highly specialized sequencing techniques for the identification of bacterial species within the biofilm structure has gained significant attraction. Goh *et al.,* (2013) for example, identified bacterial species on the fouled membrane through DNA amplification using polymerase chain reaction (PCR). The bacterial organisms were predominantly thermophilic and halotolerant, including *Rubrobacter taiwanensis*, *Caldalkalibacillus uzonensis*, *Caldalkalibacillus uzonensis*, *Tepidimonas sp*, and *Meiothermus hypogaeus*. In addition to identifying bacterial species; growth patterns and behavioural changes of specific microorganisms can be identified, particularly using 16S rDNA and 16S rRNA gene sequencing techniques C. Liu *et al.,* (2020a) studied the bacterial composition of the biofilm on the membrane surface using 16S rRNA and 16S rDNA gene sequencing. Analysis was done following DNA extraction. The abundance of live bacteria was higher during the initial biofilm development stage which sharply reduced as a function of time. This decrease was associated with an increase in salt crystal deposition on the membrane.

2.4 Microorganisms responsible for membrane biofouling in MD

Since feed solutions sourced from different environmental locations contain microorganisms of different identity, studying feed solution composition is imperative. Feed solutions sourced from marine environments are discovered to cause biofouling through enhancing the deposition of phyla *Firmicutes*, *Bacteroidetes* and *Proteobacteria*, especially at high temperatures and high water salinity (Belila *et al.*, 2016). From a general perspective, bacteria enhancing biofilm development in MD include *genera Mycobacterium*, *Bacillus*, *Lactobacillus, Cytophaga*, and *Flavobacterium* (Matin *et al.*, 2011). It is important to note that not all microorganisms present in the feed solution cause biofouling in MD, as microorganisms evolve and adapt to changing conditions.

Gryta, (2002) evaluated biofouling occurrence in MD. Prior to MD operation, the feed solution was characterized by genera *Pseudomonas*, *Penicillium bacteria*, Aspergillus fungi and species *S. faecalis*. Evaluation of the biofilm on the membrane surface following MD operation displayed the presence of *S. faecalis* and Aspergillus fungi only. Genera *Pseudomonas* growth was hindered by oxygen deficiency and high-water salinity. In another study, Zheng *et al.*, (2022) reported a change of plump sphere or short rod to lankier rhabditiform with a microbial community transformation from *Algoriphagus, Marinobater*, and *Sulfurihydrogenibium* to *Chelativorans, Acinetobater,* and *Idiomarina*. The change in microbial community was attributed to the elevated temperatures and high saline conditions under which MD processes operate. Moreover, the latter strains notably survived due to having high motility, good quorum sensing and high secretory ability.

C. Liu *et al.,* (2020a) used lake water (Xuanwu Lake) characterized by *Proteobacteria, Actinobacteria, Bacteroidetes,* and *Cyanobacteria* to assess biofilm development under closed and open loop operations of MD. Early biofilm development consisted of genera *Acidovorax* and *Acetobacteraceae*, which were replaced by thermophilic *Methyloversatilis* at stage 2 of flux decay. Only *Gammaproteobacteria* and *Deinococcus-Thermus* were detected from the biofilm under closed loop operation. The viability of these strains was explained by their halotolerant mechanism induced by a change in morphology and identity to withstand heat (Zheng *et al.*, 2022). Under open loop operation, the membrane biofilm was dominated by *Anoxybacillus, Meiothermus, Schlegelella, Tepidimonas*, and *Vulcaniibacterium*. These examples show that the viability of microorganisms and the succession of microbial communities strongly depend on process parameters.

Microbial succession is detrimental to MD as it leads to the production of more EPS, which decreases membrane life span and further lowers process performance. Sometimes, however, microbial communities present in the feed solution do not evolve, but deposit on the membrane surface as they are, just in varying degrees. Zodrow *et al.,* (2014) evaluated the biofouling impact of seawater, predominantly characterized by *Octadecabacter*, *Sediminicola*, *Loktanella*, and *Pelagibacteraceae*. All aforementioned

bacteria were detected on the membrane surface as well, although in varying degrees. The most abundant strain was *Octadecabacter*, due to its capability to survive high temperatures. Other strains detected included thermophilic *Bacillales* and spore self-protective *Ralstonia.* Additional microbes identified from the biofilm are listed in **Table 2.1**.

Table **2.1**: Biofouling-causing microbial organisms in MD

Feed source	Operating conditions	Microorganisms	Reference
Saline wastewater (From animal intestines)	Temp: F – 80℃ P – 25℃ CV: 0.367 m/s	*S. faecalis* (S)	(Gryta, 2002)
Seawater (Long Island Sound)	Temp: F – 50.4℃ P – 18.1℃ CV: 4.3 cm/s	*Ralstonia* (G) *Octadecabacter* (G) *Pelagibacteraceae* (F) *Loktanella* (G) *Sediminicola* (G) *Vibrionaceae* (F) *Rhodobacteraceae* (F) *Cryomorphaceae* (F) *Flavobacteriaceae* (F) *Bacillales* (O)	(Zodrow *et al.*, 2014)
Xuanwu Lake (China)	Temp: F – 60℃ P – 10℃ CV:	*Anoxybacillus* (G) *Meiothermus* (G) *Schlegelella* (G) *Tepidimona* (G) *Vulcaniibacterium* (G) *Proteobacteria* (P) *Deinococcus-Thermus* (P)	(C. Liu *et al.,* 2020a)
Xuanwu Lake, Nan Lake and Qinhuai	Temp: F – 60℃ P – 15℃ CV: 10.5mm/s	*Tepidimonas* (G) *Meiothermus* (G) *OLB14_norank* (G)	(Chen *et al.*, 2021)

River (Nanjing, China)		*Schlegelella* (G) *Hydrogenophilaceae* (F) *Env.OPS 17_norank* (G) *Armatimonadetes_norank* (G)	
Wastewater from power plant	Temp: F – 55℃ P – 25℃ CV:	*Idiomarina* (G) *Chelativorans* (G) *Phenylobacterium* (G) *Methyloversatilis* (G) *Schlegelella* (G) *Aeribacillus* (G) *Bacillus* (G) *Actinobacteria* (P) *Chloroflexi* (P) *Microgenomates* (P)	(Zheng *et al.*, 2022)
Xuanwu Lake (China)	Temp: F – 60℃ P – 10℃ CV: 10.5 mm/s	*Tepidimonas* (G) *Meiothermus* (G) *Sphingobium* (G) *env.OPS 17_norank* (G) *Curvibacter* (G) *OLB14_norank* (G) *Pelomonas* (G) *Novosphingobium* (G) *Sphingomonas* (G) *Bradyrhizobium* (G) *Chelatococcus* (G) *Geobacillus* (G)	(Liu, Zhu and Chen, 2020b)
Artificial sterile wastewater	Temp: F – 55℃ P – CV:	*Anoxybacillus sp* (G)	(Bogler and Bar-Zeev, 2018)

F and P are the feed and distillate temperatures, CV is the crossflow velocity, and the letters G, F, O, P and S represent the taxonomic classification of the microorganisms namely: G=genus, F=family, O=order, P=phylum, and S=species.

2.5 Effects of biofouling on process performance

Microbial accumulation on the membrane surface produces undesirable consequences, including water flux decline, salt rejection decline and frequent membrane replacements. These effects are largely caused by vapor pressure depression/pore blockage, membrane wetting, and the accumulation of EPS and protein. Microbial accumulates on feed spacers (inserted inside the membrane module during operation to increase flow turbidity) can further exacerbate fouling though providing more surface area where these foulants can adhere. **Table 2.2** summarizes the impact of biofouling on MD efficiency. The conclusion that can be drawn from this table is that the feed solution composition is the most important factor to consider (for any operation) if biofouling is to be minimized. For example, while the treatment of coastal seawater presented minimal effects on the salt rejection efficiency of the system, the treatment of sludge resulted in a 71.9% decrease in the salt rejection efficiency, and therefore lowering process performance. Overall, it is important to note that the decline of MD efficiency is complex and may not be attributed to biofouling alone.

Table 2.2: A summarized impact of biofouling on MD efficiency

Configurat-ion of MD	Type of membrane	Feed type	Temperature (ºC)	Flux decay (L/m^2/h)	Salt rejection decay	Reference
DCMD	PP	Coastal seawater	Fe – 40 P – 20	I – 3.85 F – 2.55	No effect on salt rejection efficiency	(Krivorot *et al.*, 2011)
MDBR	PVDF	Sludge suspension	Fe – 55 P – 19.5	I – 8.42 F – 3.36	I – 217 µS/cm F – <600 µS/cm	(Goh *et al.*, 2013)
DCMD	-	Artificial sterile wastewater	Fe – 65 P –	I – 23.0 F – 15.6	I – 1000 µS/cm F – 90000 µS/cm	(Bogler and Bar-Zeev, 2018)
MDBR	PVDF/PTFE	Sludge	Fe – 56 P – 25	I – 12.7 F – 1.90	I – 1.6 g/L F – 5.7 g/L	(Phattaranawik *et al.*, 2009)
DCMD	PTFE	Estuarine water	Fe – 50.4 P – 18.1	I – 20.0 F – 10.0	No effect on salt rejection efficiency	(Zodrow *et al.*, 2014)
DCMD	PTFE	Lake water	Fe – 60 P – 10	I – 9.67 F – 4.28	I – 2.33 µS/cm F – <12.7 µS/cm	(Liu, Zhu and Chen, 2020a)
DCMD	PTFE	Qinhuai river	Fe – 60 P – 15	I – 8.10 F – 4.30	I – 324.7 µS/cm F – <23.0 µS/cm	(Chen *et al.*, 2021)
DCMD	PVDF	Effluent water	Fe – 60 P – 20	I – 40 F – 21	I – 100% F – 97%	(Nthunya, Gutierrez, Khumalo, *et al.*, 2019a)

Where Fe, P, I and F, represent the feed temperature, distillate temperature, initial and final water flux/salt rejection efficiency, respectively.

2.5.1 Distillate flux decay

Membrane biofilm development notably causes a reduction in water flux. The water flux decreases due to: (1) membrane pore-blockage, (2) vapor pressure reduction, (3) temperature polarization (**Figure 2.4**) and (4) concentration polarization effects. Commonly, the major cause of MD distillate flux decay is the blockage of membrane pores, where the passage of vapor is obstructed by the biofouling layer (Chew, Krantz and Fane, 2014). The degree of pore blockage determines the extent of flux decay. Goh *et al.,* (2013) noted a 60% decrease in water flux caused by the accumulation of microbial contaminants on the surface of the membrane. These contaminants essentially caused a decrease in the vapor pressure of the system by 20% to 32%. Another plausible explanation given for the reduction in flux was the resistance to heat and mass transfer across the boundary layer. Resistance to heat transfer occurs when heat from the feed solution is prevented from reaching the membrane surface where vaporization takes place. This decreases performance efficiency and invariably increases costs of operation (Costa *et al.*, 2021). Future modelling studies of MD looking into vapor pressure depression around biofouling should be considered to gain insights into its mitigation.

Notably, the degree of water flux decline depends on the temperature of the feed solution as well. Bogler & Bar-Zeev, (2018) evaluated the impact of biofouling in MD. The feed stream temperatures were controlled at 47℃, 55℃ and 65℃. Correspondingly, the percentages of the water flux declines reported were 30%, 78% and 32%, respectively. The flux declines were attributed to a variety of reasons. At 47℃, the 30% flux drop was attributed to the enhanced TP and CP phenomena caused by the presence of biofoulants. At 55℃, the 78% flux decline was attributed to the increased growth of the bacteria under study (*Anoxybacillus sp*) on the membrane surface as those were its optimal growth conditions. Here, it was suggested that biofouling in MD can be greatly minimized if the feed temperatures are kept below or above the optimal growth conditions of the bacteria

expected to cause biofouling. However, as was seen from previous sections, the adaptability of bacteria induces substantial challenges as new strains may thrive under new conditions. At 65ºC, substantial pore wetting caused the 32% flux decline. Overall, membrane wetting significantly affected the entire system of the MD operation.

In a recent study by Elcik *et al*., (2022), similar tests were conducted, where feed stream temperatures of 45ºC, 55ºC and 65ºC were evaluated for biofilm progression in MD. Notably, flux drops of 71.8%, 71.5% and 79% were experienced at 45ºC, 55ºC and 65ºC, respectively. Biofilm thickness was reported to induce the flux decline, as a biofilm thickness of 250 ± 10 μm was obtained for 65ºC, 95 ± 10 μm for 45ºC and 130 ± 20 μm for 55ºC.

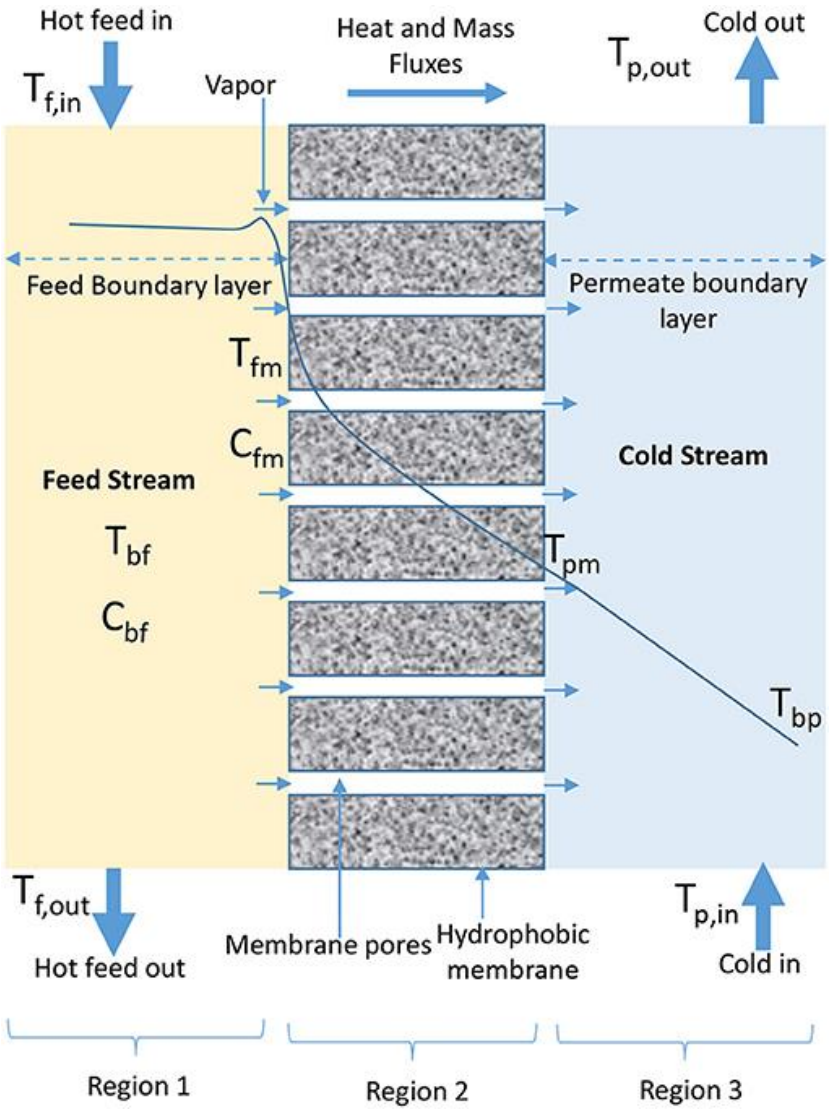

Figure 2.4: Temperature polarization phenomenon in MD. Tf,in, Tfm, Tpm and Tpb represent temperatures in the bulk feed solution, near the membrane surface (feed side), near the membrane surface (distillate side) and in the bulk distillate, respectively (Olatunji and Camacho, 2018).

2.5.2 Salt rejection decline

Membrane wetting is a fundamental aspect requiring significant attention in MD systems. Wetting promotes the passage of the feed stream though the pores of the membrane, reducing the solute (e.g., salt) rejection efficiency (Nthunya *et al.*, 2022). Membrane wetting occurs as a result of an increase in hydrophilicity of the membrane pores following biofilm development. Bogler & Bar-Zeev, (2018) reported a reduced salt rejection efficiency caused by EPS-induced membrane wetting. A significant difference in salt rejection efficiency was obtained for different feed operating temperatures. At 55℃ and 65℃, a respective 30-fold and 90-fold increase in distillate salinity was obtained. The 90-fold increase was attributed to the improved bacterial growth conditions causing rapid biofilm formation. It is evident from the study that both salt rejection and water flux declines occurred only after inoculation of the feed water with bacteria (*Anoxybacillus sp.*)

Zodrow *et al.,* (2014) evaluated biofilm development in RO and MD systems. For MD systems, it was found that although the hydrophobicity of the membrane decreased from 134 ± 4º to 32 ± 6º due to the presence of a foulant layer, no membrane wetting occurred. This was attributed to the hydrophilic layer on the membrane surface preventing and blocking pores from encountering the feed solution and getting wet. It was thereby concluded that it is not enough for the surface of the membrane to be hydrophilic, the pores also need to be wet for salt rejection decay to be realized.

2.5.3 Frequency of membrane replacements

A decrease in membrane lifespan of hydrophobic membranes caused by the accumulation and persistence of biofilm development leads to frequent membrane replacements. This causes significant increases in operational costs (Nthunya *et al.*, 2022). The frequency of membrane replacements largely depend on the type of feed stream treated and the hydrodynamic conditions (Avlonitis, Kouroumbas and Vlachakis, 2003). In desalination plants, membrane replacement occurs within 4 – 5 years whereas industries treating dairy products replace membranes within 3 years (Avlonitis, Kouroumbas and Vlachakis, 2003). In general, membrane replacements are not

recommended due to interruptions in the process and significant amount of labor requirements (Agrawal *et al.*, 2021). Hence, mitigation of biofouling in MD is highly encouraged.

2.6 Mitigation of biofouling in MD

Major strategies used to mitigate biofouling in MD have been proposed and include pre-treatment of the feed solution, membrane modification and membrane cleaning (**Figure 2.5**). The detailed impact of these strategies towards water flux and salt rejection stabilities is presented in **Table 5.3**.

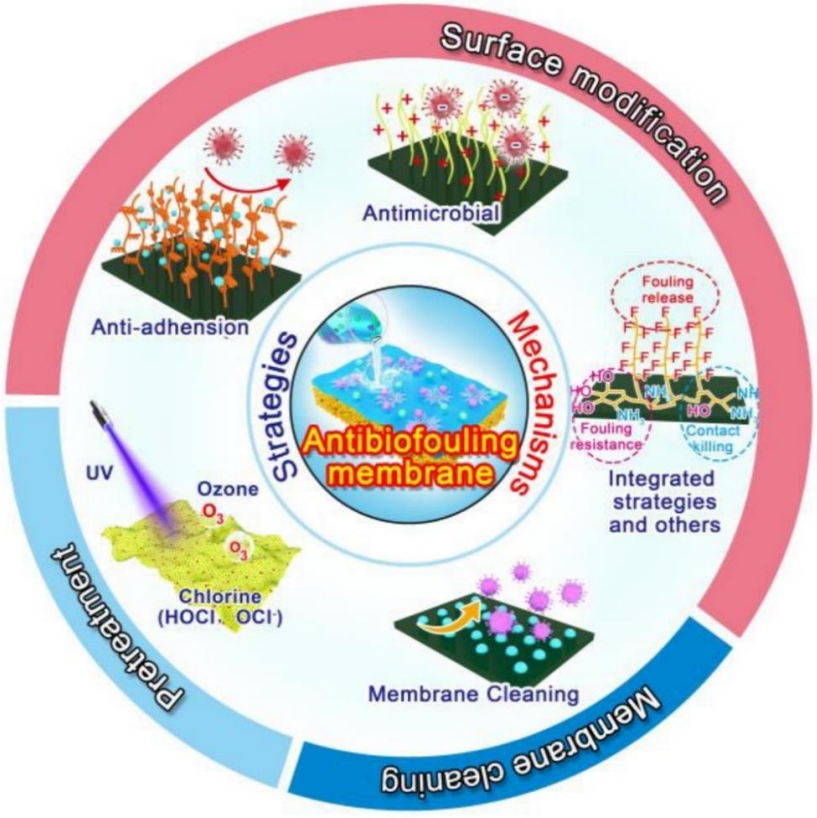

Figure 2.5: Latest developments of biofouling control strategies in MD (H. Zhang *et al.*, 2022)

2.6.1 Pre-treatment of the feed solution

Membranes subjected to contaminated saline wastewaters are prone to biofouling. Therefore, pre-treatment of the feed solution is a useful tool for the minimization of biofouling. Pre-treatment involves the removal of potential foulants from the feed solution before MD processing, reducing the concentration of biofoulants entering the module. This may cause a delay in water flux reduction and reduce the rate of membrane cleaning (B. Zhang *et al.*, 2022). Pre-treatment methods are largely dependent on the composition of the feed solution (Choudhury *et al.*, 2019). There are two types of pre-treatment methods widely applied in membrane-based technologies: (1) physical pre-treatment, and (2) chemical pre-treatment processes.

a) Physical pre-treatment processes

A variety of physical pre-treatment processes exist including filtration (ultra/micro), sonication and UV radiation, amongst others. Ultra- and Micro-filtration utilize the mechanism of size-exclusion to selectively prevent certain contaminants from becoming a part of the feed stream (Zodrow *et al.,* 2014). This minimizes nutrient availability in the feed stream and minimizes microbial growth during biofilm development. It is important to note here that bacteria are self-replicating and any planktonic cell that survives filtration may enter the module and reproduce, enhancing biofilm development (Mansouri, Harrisson and Chen, 2010). Hence, pre-treatment of the feed solution for biofouling management is not encouraged (Mansouri, Harrisson and Chen, 2010). If sterilization is not 100% effective, some bacteria may survive and reproduce, and exacerbate fouling. Sonication is another alternative strategy to the management of bacterial growth, where ultrasound frequencies of ≥ 18 KHz are used to effectively mitigate fouling (Gizer *et al.*, 2023). Here, fouling is mitigated though cavitation, where the production of strong convective currents is triggered (Aghapour Aktij *et al.*, 2020). Studies related to ultrasound treatment in minimizing bacterial growth are few. Mathieu *et al.*, (2019) studied the ability of ultrasound to inhibit bacterial growth in bulk drinking water “N” spiked with 100 mg/L of

$Ca(OH)_2$. Evidently, there was a 7-fold reduction in bacterial growth (from 1.4×10^5 mL^{-1} to 2.0×10^4 mL^{-1}) caused by the injection of ultrasonic waves. This was achieved though using an ultrasound frequency of 46 KHz.

b) Chemical pre-treatment processes

Coagulation, chlorine injection and ozone injection are some of the chemical processes used during chemical pre-treatment. Coagulation is the cheapest and most convenient process, involving the stabilization of particulates though addition of a coagulant promoting agglomeration within the feed stream (Alkhatib, Ayari and Hawari, 2021). Inorganic coagulants include ferric chloride ($FeCl_3$), aluminium chloride ($AlCl_3$) and polymeric aluminium chloride (PAC) whereas organic coagulants include polyacrylamide (PAM), poly dimethyl diallyl ammonium chloride (PDMDAAC) and microbial flocculants (Ren *et al.*, 2019; Zhao *et al.*, 2021). Since higher doses of inorganic flocculants are known to cause secondary pollutants due to the presence of residual metal ions, a hybrid system of organic and inorganic coagulants is usually used to enhance the performance of coagulation. B. Zhang *et al.,* (2022) used a hybrid system to evaluate the performance of microbial flocculants modified with PAC (MMF/PAC) to minimize fouling. Cake layer formation on the membrane surface was effectively mitigated, especially in comparison to the individually applied inorganic flocculant, PAC. The optimum concentration of MMF in MMF/PAC (for optimum performance) was 10 mg/L. Management of biofilm development has further been seen though chlorine dosages, largely at concentrations of 1 – 50 ppm (Costa *et al.*, 2021). Although chlorination of the feed stream effectively prevents biofilm development, it produces mutagenic and carcinogenic by-products that are harmful (Zemite *et al.*, 2022).

2.6.2 Membrane cleaning

Membrane cleaning involves the removal of microbial accumulates from the membrane surface following deposition. The concept of membrane cleaning was introduced to

restore the original performance of the membrane following fouling interruptions (Costa *et al.*, 2021). Membrane cleaning further reduces the rate of membrane replacements (Alzahrani *et al.*, 2013). There are two types of cleaning methods widely applied in membrane-based technologies: (1) physical cleaning and (2) chemical cleaning.

a) Physical cleaning

Physical cleaning involves the use of deionized water during MD operation to facilitate foulant detachment (Guo *et al.*, 2022). Using water guarantees minimal damage to the membrane structure. During cleaning, pumping of the feed stream into the module stops, followed by deionised water running through the system, usually at higher flowrates. These flowrates ensure increased shear forces that induce optimal detachment of foulants from the membrane surface and spacers (Bogler, Lin and Bar-Zeev, 2017). In other instances, high pressure water is utilized (Gizer *et al.*, 2023). Lyly *et al*., (2021) evaluated deionised water's ability (as a cleaning agent) to restore the performance of PTFE membranes. The feed solution used was a 35 000 ppm NaCl solution spiked with BSA (1000 ppm) and microalgae (*Cylindrotheca fusiformis*). After running the operation for 35 h, the following steps were implemented for physical cleaning: (1) running of pure cold-water (at 25ºC) for 10 mins, (2) running of pure hotwater (at 60ºC) for 10 mins and (3) running of cold-water again for 5 mins. Reportedly, the water flux was restored by 62.69%, displaying promising results for future applications. In the same study, modification of PTFE with PVDF as top later and poly(N-Isopropylacrylamide) as modifying agent presented a water flux restoration of 88.26%.

b) Chemical cleaning

Chemical cleaning involves the exclusive use of chemicals to continuously remove foulants from the membrane surface. To avoid unalterable damage to the membrane, the concentration of the cleaning agent and frequency of membrane cleaning is optimized (Choudhury *et al.*, 2019). Current literature is dominated by the chemical cleaning of inorganic fouled (using acidic solutions) and organic fouled (using basic solutions)

membranes (Guillen-Burrieza *et al.*, 2014). Reported chemical cleaning of biofouled membranes is limited. Zheng *et al.,* (2022) sought to remove microbial accumulates on the membrane surface by applying different concentrations of HCl and water. The process ensured complete removal of *Euryarchaeota*. However, full restoration of the flux was not achieved, largely due to *Idiomarina* cells' affinity for the membrane surface.

Although process performance efficiency is notably restored by membrane cleaning, modification of the membrane is highly encouraged to render biofouling-resistance to the hydrophobic membranes (Bogler, Lin and Bar-Zeev, 2017). This approach ensures minimal waste disposal, subsequently posing less risk to the environment (Ben-Sasson *et al.*, 2014).

2.6.3 Membrane modification

Membrane modification involves the alteration of membrane properties to render the membrane resistant to biofouling. Membranes are modified though various approaches; including the incorporation of metal nanoparticles (MNPs) (**Figure 2.6**) and the alteration of membrane surface properties such as surface roughness, membrane hydrophobicity and surface charge (Choudhury *et al.*, 2018). Herein, we will only deal with the incorporation of MNPs.

a) Incorporation of MNPs

Attachment and proliferation of microbial cells on membrane surfaces is largely minimized through the incorporation of biocidal MNPs. Upon oxidation, ionic counterparts of the biocidal MNPs get released and react with microbial cells, inactivating them. Biocidal MNPs capable of inactivating bacterial cells include Ag, Ti, Zn and Fe (Slavin *et al.*, 2017; Guo *et al.*, 2022). Inactivation occurs due to the electrostatic interaction between the positively charged metal ions and the negatively charged thiol groups on the DNA of the bacteria (Politano *et al.*, 2017). Amongst others, AgNPs are the most commonly used to inhibit biofouling (Somayajula *et al.*, 2019; Xuan *et al.*, 2020). In addition to membrane

systems, many different industries apply AgNPs for their anti-microbial properties, including textile, medicinal, wood dressing, and food packaging industries (Fu *et al.*, 2016). Nthunya et al., (2020) modified the PVDF membrane using AgNPs and functionalized carbon nanotubes (*f*-MWCNTs), achieving successful biofouling, colloidal and organic fouling control. Although biofouling mitigation is evident when applying membrane modification, biocidal MNPs tend to leach from the membrane surface, an event that reduces their antibacterial activity over-time (Bogler, Lin and Bar-Zeev, 2017). In addition, the quality of water produced from the operation may be reduced following leaching. Hence, ensuring the stability of these MNPs on membrane surfaces is crucial. Stability is assured through a variety of ways, including the use of biopolymers such as cellulose, containing abundant negatively charged groups on the surface capable of stabilizing these MNPs.

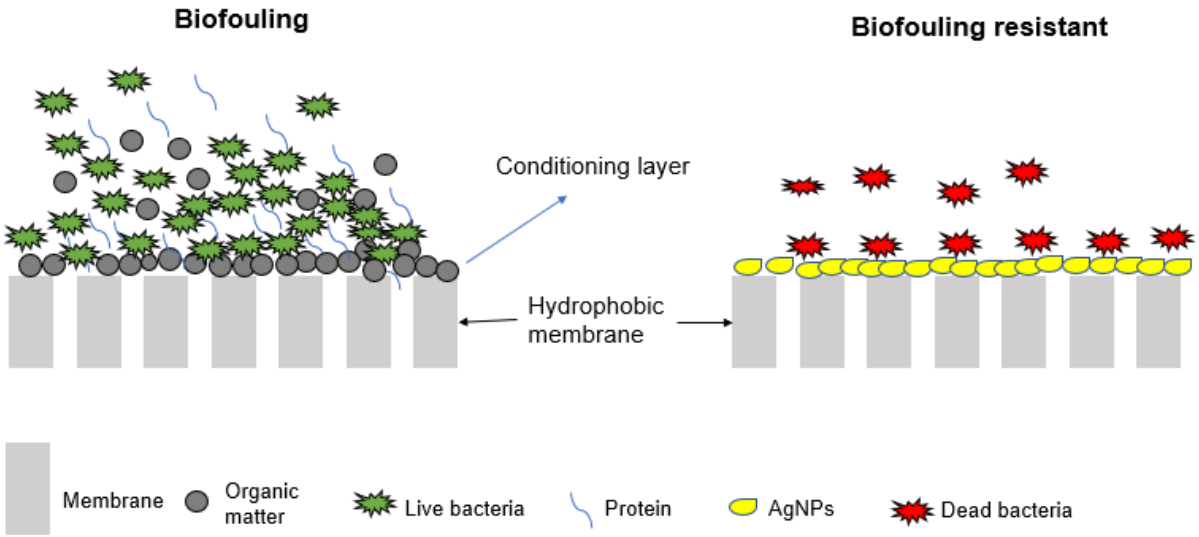

Figure 2.6: Membrane modification using MNPs

CNCs are nano-structural forms of cellulose, the most important structural constituent of the cell walls of plants and algae. Paper-producing industries isolate cellulose from wood for use during the production of cardboard and paper (Trache *et al.*, 2017). Other

applications of cellulose include its addition in textile and technical products. In addition to exhibiting various advantages such as biocompatibility, bioavailability, chemical functionality and high surface to volume ratio, CNCs have shown to exhibit tremendous tensile strength (Chen *et al.*, 2011). Moreover, the presence of hydroxyl groups on the surface has made the grafting of various chemical functional groups and MNPs on the backbone possible.

Isolation methods of CNC's from wood includes acid hydrolysis (Karim *et al.*, 2016), mechanical refining (Qiao *et al.*, 2015), water hydrolysis (Novo *et al.*, 2016), oxidation methods (Sun *et al.*, 2015) and enzymatic hydrolysis (Anderson *et al.*, 2014). However, the main experimental method for CNC preparation is through acid hydrolysis (Habibi, Lucia and Rojas, 2010). The reason behind acid hydrolysis is for enabling the disintegration of amorphous regions for the removal of hemicellulose and lignin. In addition, the subjection of cellulose to acid is generally known to decrease the degree of Polymerization (DP) between structural linkages of the polymer (Håkansson and Ahlgren, 2005). Following acid hydrolysis, a white crystal-like solid remains that is primarily composed of crystalline regions, which requires dialysis with distilled water (several times) before further application. The two prominent acid solutions used during hydrolysis are hydrochloric acid (HCl) and sulphuric acid (H_2SO_4). CNC's produced through HCl subjection tend to flocculate in solution and have been reported to display limited dispersion (Araki *et al.*, 1998). The use of H_2SO_4, however, promotes the non-dispersion of crystal structures in solution. However, H_2SO_4 produced CNC's display little thermostability due to the presence of charged sulphate groups (Roman and Winter, 2004). Consequently, HCl and H_2SO_4 are used simultaneously during reactions for the production thermally stable and disperse CNC's.

Table 2.3: Mitigation strategies of biofouling in MD

Membrane configuration	Mitigation strategy	Mitigation process	Feed solution	Duration of operation	Impact on water flux and salt rejection efficiency	Ref.
DCMD	Pre-treatment	Chlorination (Addition of HCl in feed stream)	Tap-water	58 days	Stable water flux and salt rejection.	(Gryta, 2002)
DCMD	Pre-treatment and membrane cleaning	Magnetic coagulation and HCl cleaning	Wastewater	65 days	Original flux of membrane restored (at high HCl concentration)	(Zheng *et al.*, 2022)
DCMD	Membrane modification	Membrane modification (f-MWCNTs and AgNPs)	Effluent water	2 days	Stable flux and salt rejection efficiencies obtained as far as biofouling was concerned.	(Nthunya *et al.*, 2020)
DCMD	Pre-treatment	Microfiltration	Estuarin water	4 days	50% decline in flux	(Zodrow *et al.*, 2014)
DCMD	Membrane cleaning	NaOH, distilled water, 70% ethanol cleaning	Coastal seawater	14 days	Original flux of membrane restored.	(Krivorot *et al.*, 2011)
AGMD	Backwash	Reversion of direction of flow	Pond water	91 days	Original flux of membrane restored	(Meindersma, Guijt and de Haan, 2006)
DCMD	Membrane modification	Coating membrane with hydrophilic active layer	Effluent water	2.5 days	47% flux decline and 99.8% salt rejection	(Nthunya, Gutierrez, Khumalo, *et al.*, 2019b)

DCMD	Membrane modification	Membrane modification (f-MWCNTs and AgNPs)	Scheldt estuary water	2 days	20.8% flux decline and 99.8% salt rejection	(Nthunya, Gutierrez, Lapeire, *et al.*, 2019)

In this chapter, a summary of the mechanism of operation of MD as well the configurations used during separation have been discussed. Moreover, the effects of biofouling in MD, as well as the mitigation strategies have been highlighted. It is worthwhile to note that while biofilm formation has a high propensity for occurrence in MD systems, assessing the feed solution composition, and optimizing membrane properties can significantly reduce it. Although membrane cleaning presents another alternative strategy to minimize biofilm development, solvent choice is of crucial importance, including its toxicity and disposal. Overall, biofouling remains a challenge in MD and requires operation-specific approaches to deal with it.

2.7 References

1. Abu-Lail, N. I. and Camesano, T. A. (2003) 'Role of ionic strength on the relationship of biopolymer conformation, DLVO contributions, and steric interactions to bioadhesion of pseudomonas putida KT2442', *Biomacromolecules*, 4(4), pp. 1000–1012. doi: 10.1021/bm034055f.
2. Adair, J. H., Suvaci, E. and Sindel, J. (2001) 'Derjaguin, Landau, Verwey and Overbeek (DLVO) theory', *Surface and Colloid Chemistry - from the Encyclopedia of Materials: Science and Technology*, (figure 3), pp. 1–10.
3. Aghapour Aktij, S. *et al.* (2020) 'A critical review on ultrasonic-assisted fouling control and cleaning of fouled membranes', *Ultrasonics*, 108(March 2019), p. 106228. doi: 10.1016/j.ultras.2020.106228.
4. Agrawal, A. *et al.* (2021) 'Metal oxides nanocomposite membrane for biofouling mitigation in wastewater treatment', *Materials Today Chemistry*, 21, p. 100532. doi: 10.1016/j.mtchem.2021.100532.

5. Alkhatib, A., Ayari, M. A. and Hawari, A. H. (2021) ‘Fouling mitigation strategies for different foulants in membrane distillation’, *Chemical Engineering and Processing - Process Intensification*, 167, p. 108517. doi: 10.1016/j.cep.2021.108517.
6. Alzahrani, S. *et al.* (2013) ‘Identification of foulants, fouling mechanisms and cleaning efficiency for NF and RO treatment of produced water’, *Separation and Purification Technology*, 118, pp. 324–341. doi: 10.1016/j.seppur.2013.07.016.
7. Anderson, S. R. *et al.* (2014) ‘Enzymatic preparation of nanocrystalline and microcrystalline cellulose’, *Tappi Journal*, 13(5), pp. 35–42. doi: 10.32964/tj13.5.35.
8. Araki, J. *et al.* (1998) ‘Flow properties of microcrystalline cellulose suspension prepared by acid treatment of native cellulose’, *Colloids and Surfaces A: Physicochemical and Engineering Aspects*, 142(1), pp. 75–82. doi: 10.1016/S0927-7757(98)00404-X.
9. Aslam, M., Ahmad, R. and Kim, J. (2018) ‘Recent developments in biofouling control in membrane bioreactors for domestic wastewater treatment’, *Separation and Purification Technology*, 206, pp. 297–315. doi: 10.1016/j.seppur.2018.06.004.
10. Avlonitis, S. A., Kouroumbas, K. and Vlachakis, N. (2003) ‘Energy consumption and membrane replacement cost for seawater RO desalination plants’, *Desalination*, 157(1–3), pp. 151–158. doi: 10.1016/S0011-9164(03)00395-3.
11. Belila, A. *et al.* (2016) ‘Bacterial community structure and variation in a full-scale seawater desalination plant for drinking water production’, *Water Research*, 94, pp. 62–72. doi: 10.1016/j.watres.2016.02.039.
12. Ben-Sasson, M. *et al.* (2014) ‘In situ formation of silver nanoparticles on thin-film composite reverse osmosis membranes for biofouling mitigation’, *Water Research*, 62, pp. 260–270. doi: 10.1016/j.watres.2014.05.049.
13. Bodell, B. R. (1968) ‘Distillation of Saline Water Using Silicone Rubber Membrane’, *United States Patent*, (3,361,645), pp. 1–4.
14. Bogler, A. and Bar-Zeev, E. (2018) ‘Membrane Distillation Biofouling: Impact of Feedwater Temperature on Biofilm Characteristics and Membrane Performance’, *Environmental Science and Technology*, 52(17), pp. 10019–10029. doi:

10.1021/acs.est.8b02744.

15. Bogler, A., Lin, S. and Bar-Zeev, E. (2017) ‘Biofouling of membrane distillation, forward osmosis and pressure retarded osmosis: Principles, impacts and future directions’, *Journal of Membrane Science*, 542, pp. 378–398. doi: 10.1016/j.memsci.2017.08.001.
16. Chen, L. *et al.* (2021) ‘The fouling layer development on MD membrane for water treatments: An especial focus on the biofouling progress’, *Chemosphere*, 264, p. 128458. doi: 10.1016/j.chemosphere.2020.128458.
17. Chen, W. *et al.* (2011) ‘Individualization of cellulose nanofibers from wood using high-intensity ultrasonication combined with chemical pretreatments’, *Carbohydrate Polymers*, 83(4), pp. 1804–1811. doi: 10.1016/j.carbpol.2010.10.040.
18. Chew, J. W., Krantz, W. B. and Fane, A. G. (2014) ‘Effect of a macromolecular- or bio-fouling layer on membrane distillation’, *Journal of Membrane Science*, 456, pp. 66–76. doi: 10.1016/j.memsci.2014.01.025.
19. Choi, Y. *et al.* (2019) ‘Membrane distillation crystallization for brine mining and zero liquid discharge: Opportunities, challenges, and recent progress’, *Environmental Science: Water Research and Technology*, pp. 1202–1221. doi: 10.1039/c9ew00157c.
20. Choudhury, M. R. *et al.* (2019) ‘Fouling and wetting in the membrane distillation driven wastewater reclamation process – A review’, *Advances in Colloid and Interface Science*, 269, pp. 370–399. doi: 10.1016/j.cis.2019.04.008.
21. Choudhury, R. R. *et al.* (2018) ‘Antifouling, fouling release and antimicrobial materials for surface modification of reverse osmosis and nanofiltration membranes’, *Journal of Materials Chemistry A*, 6(2), pp. 313–333. doi: 10.1039/c7ta08627j.
22. Costa, F. C. R. *et al.* (2021) ‘Biofouling in membrane distillation applications - a review’, *Desalination*, 516(July). doi: 10.1016/j.desal.2021.115241.
23. Dohany, Julius, E. (2000) ‘FLUORINE-CONTAINING POLYMERS , POLY (VINYLIDENE FLUORIDE)’, (20).
24. Drioli, E., Ali, A. and Macedonio, F. (2015) ‘Membrane distillation: Recent

developments and perspectives', *Desalination*, 356, pp. 56–84. doi: 10.1016/j.desal.2014.10.028.

25. El-Bourawi, M. S. *et al.* (2006) 'A framework for better understanding membrane distillation separation process', *Journal of Membrane Science*, 285(1–2), pp. 4–29. doi: 10.1016/j.memsci.2006.08.002.
26. Elcik, H. *et al.* (2022) 'Elucidating biofouling over thermal and spatial gradients in seawater membrane distillation in hot climatic conditions', *Water Research*, 223(May), p. 118983. doi: 10.1016/j.watres.2022.118983.
27. Eykens, L. *et al.* (2016) 'How To Optimize the Membrane Properties for Membrane Distillation: A Review', *Industrial & Engineering Chemistry Research*, 55(35), pp. 9333–9343. doi: 10.1021/acs.iecr.6b02226.
28. Fabre, H. *et al.* (2018) 'Impact of hydrophilic and hydrophobic functionalization of flat TiO 2 /Ti surfaces on proteins adsorption', *Applied Surface Science*, 432, pp. 15–21. doi: 10.1016/j.apsusc.2017.08.138.
29. Fu, L. H. *et al.* (2016) 'Comparative study of cellulose/Ag nanocomposites using four cellulose types', *Materials Letters*, 171, pp. 277–280. doi: 10.1016/j.matlet.2016.02.118.
30. Gizer, G. *et al.* (2023) 'Biofouling and Mitigation Methods: A Review', *Biointerface Research in Applied Chemistry*, 13(2), pp. 1–25. doi: 10.33263/BRIAC132.185.
31. Goh, S. *et al.* (2013) 'Impact of a biofouling layer on the vapor pressure driving force and performance of a membrane distillation process', *Journal of Membrane Science*, 438, pp. 140–152. doi: 10.1016/j.memsci.2013.03.023.
32. Gryta, M. (2002) 'The assessment of microorganism growth in the membrane distillation system', *Desalination*, 142(1), pp. 79–88. doi: 10.1016/S0011-9164(01)00427-1.
33. Guastalli, A. R. *et al.* (2013) 'Comparison of DMF and UF pre-treatments for particulate material and dissolved organic matter removal in SWRO desalination', *Desalination*, 322, pp. 144–150. doi: 10.1016/j.desal.2013.05.005.
34. Guillen-Burrieza, E. *et al.* (2014) 'Membrane fouling and cleaning in long term plant-scale membrane distillation operations', *Journal of Membrane Science*, 468, pp. 360–372. doi: 10.1016/j.memsci.2014.05.064.

35. Guo, Y. *et al.* (2022) 'Contemporary antibiofouling modifications of reverse osmosis membranes: State-of-the-art insights on mechanisms and strategies', *Chemical Engineering Journal*, 429, p. 132400. doi: 10.1016/j.cej.2021.132400.
36. Habibi, Y., Lucia, L. A. and Rojas, O. J. (2010) 'Cellulose nanocrystals: Chemistry, self-assembly, and applications', *Chemical Reviews*, 110(6), pp. 3479–3500. doi: 10.1021/cr900339w.
37. Håkansson, H. and Ahlgren, P. (2005) 'Acid hydrolysis of some industrial pulps: Effect of hydrolysis conditions and raw material', *Cellulose*, 12(2), pp. 177–183. doi: 10.1007/s10570-004-1038-6.
38. Hori, K. and Matsumoto, S. (2010) 'Bacterial adhesion: From mechanism to control', *Biochemical Engineering Journal*, 48(3), pp. 424–434. doi: 10.1016/j.bej.2009.11.014.
39. Hou, D. *et al.* (2014) 'Preparation and characterization of PVDF flat-sheet membranes for direct contact membrane distillation', *Separation and Purification Technology*, 135(1), pp. 211–222. doi: 10.1016/j.seppur.2014.08.023.
40. Jiang, X. *et al.* (2017) 'Progress in membrane distillation crystallization: Process models, crystallization control and innovative applications', *Frontiers of Chemical Science and Engineering*, pp. 647–662. doi: 10.1007/s11705-017-1649-8.
41. Karim, Z. *et al.* (2016) 'Nanocellulose based functional membranes for water cleaning: Tailoring of mechanical properties, porosity and metal ion capture', *Journal of Membrane Science*, 514, pp. 418–428. doi: 10.1016/j.memsci.2016.05.018.
42. Kevin W. Lawson, D. R. L. (1997) 'Membrane distillation', *Elsevier*.
43. Khayet, M. (2011) 'Membranes and theoretical modeling of membrane distillation: A review', *Advances in Colloid and Interface Science*, 164(1–2), pp. 56–88. doi: 10.1016/j.cis.2010.09.005.
44. Krivorot, M. *et al.* (2011) 'Factors affecting biofilm formation and biofouling in membrane distillation of seawater', *Journal of Membrane Science*, 376(1–2), pp. 15–24. doi: 10.1016/j.memsci.2011.01.061.
45. Lai, C. Y. *et al.* (2014) 'Preparation and characterization of poly(vinylidene fluoride)/nanoclay nanocomposite flat sheet membranes for abrasion resistance',

Water Research, 57, pp. 56–66. doi: 10.1016/j.watres.2014.03.005.

46. Liu, C., Zhu, L. and Chen, L. (2020a) 'Biofouling phenomenon of direct contact membrane distillation (DCMD) under two typical operating modes: Open-loop mode and closed-loop mode', *Journal of Membrane Science*, 601. doi: 10.1016/j.memsci.2020.117952.
47. Liu, C., Zhu, L. and Chen, L. (2020b) 'Effect of salt and metal accumulation on performance of membrane distillation system and microbial community succession in membrane biofilms', *Water Research*, 177, p. 115805. doi: 10.1016/j.watres.2020.115805.
48. Liu, F. *et al.* (2011) 'Progress in the production and modification of PVDF membranes', *Journal of Membrane Science*, 375(1–2), pp. 1–27. doi: 10.1016/j.memsci.2011.03.014.
49. Luan, Y. *et al.* (2018) 'Bacterial interactions with nanostructured surfaces', *Current Opinion in Colloid and Interface Science*, 38, pp. 170–189. doi: 10.1016/j.cocis.2018.10.007.
50. Lyly, L. H. T. *et al.* (2021) 'Desalinating microalgal-rich water via thermoresponsive membrane distillation', *Journal of Environmental Chemical Engineering*, 9(5), p. 105897. doi: 10.1016/j.jece.2021.105897.
51. Maikranz, E. *et al.* (2020) 'Different binding mechanisms of: Staphylococcus aureus to hydrophobic and hydrophilic surfaces', *Nanoscale*, 12(37), pp. 19267–19275. doi: 10.1039/d0nr03134h.
52. Mansouri, J., Harrisson, S. and Chen, V. (2010) 'Strategies for controlling biofouling in membrane filtration systems: Challenges and opportunities', *Journal of Materials Chemistry*, 20(22), pp. 4567–4586. doi: 10.1039/b926440j.
53. Manzoor, K. *et al.* (2022) 'Assessment of anaerobic membrane distillation bioreactor hybrid system at mesophilic and thermophilic temperatures treating textile wastewater', *Journal of Water Process Engineering*, 46, p. 102603. doi: 10.1016/j.jwpe.2022.102603.
54. Mathieu, L. *et al.* (2019) 'Assessment of a low-frequency ultrasound device on prevention of biofilm formation and carbonate deposition in drinking water systems', *Ultrasonics Sonochemistry*, 52, pp. 41–49. doi:

10.1016/j.ultsonch.2018.10.029.

55. Matin, A. *et al.* (2011) 'Biofouling in reverse osmosis membranes for seawater desalination: Phenomena and prevention', *Desalination*, 281(1), pp. 1–16. doi: 10.1016/j.desal.2011.06.063.
56. Meindersma, G. W., Guijt, C. M. and de Haan, A. B. (2006) 'Desalination and water recycling by air gap membrane distillation', *Desalination*, 187, pp. 291–301. doi: 10.1016/j.desal.2005.04.088.
57. Nakoa, K., Date, A. and Akbarzadeh, A. (2015) 'A research on water desalination using membrane distillation', *Desalination and Water Treatment*, 56(10), pp. 2618–2630. doi: 10.1080/19443994.2014.972731.
58. Novo, L. P. *et al.* (2016) 'A study of the production of cellulose nanocrystals through subcritical water hydrolysis', *Industrial Crops and Products*, 93, pp. 88–95. doi: 10.1016/j.indcrop.2016.01.012.
59. Nthunya, L. N., Gutierrez, L., Lapeire, L., *et al.* (2019) 'Fouling-resistant PVDF nanofibre membranes for the desalination of brackish water in membrane distillation', *Separation and Purification Technology*, 228, p. 115793. doi: 10.1016/j.seppur.2019.115793.
60. Nthunya, L. N., Gutierrez, L., Khumalo, N., *et al.* (2019a) 'Superhydrophobic PVDF nanofibre membranes coated with an organic fouling resistant hydrophilic active layer for direct-contact membrane distillation', *Colloids and Surfaces A: Physicochemical and Engineering Aspects*, 575, pp. 363–372. doi: 10.1016/j.colsurfa.2019.05.031.
61. Nthunya, L. N., Gutierrez, L., Khumalo, N., *et al.* (2019b) 'Superhydrophobic PVDF nanofibre membranes coated with an organic fouling resistant hydrophilic active layer for direct-contact membrane distillation', *Colloids and Surfaces A: Physicochemical and Engineering Aspects*, 575, pp. 363–372. doi: 10.1016/j.colsurfa.2019.05.031.
62. Nthunya, L. N. *et al.* (2020) 'F-MWCNTs/AgNPs-coated superhydrophobic PVDF nanofibre membrane for organic, colloidal, and biofouling mitigation in direct contact membrane distillation', *Journal of Environmental Chemical Engineering*, 8(2), p. 103654. doi: 10.1016/j.jece.2020.103654.

63. Nthunya, L. N. *et al.* (2022) ‘Fouling, performance and cost analysis of membrane-based water desalination technologies: A critical review’, *Journal of Environmental Management*, 301, p. 113922. doi: 10.1016/j.jenvman.2021.113922.
64. Olatunji, S. O. and Camacho, L. M. (2018) ‘Heat and mass transport in modeling membrane distillation configurations: A review’, *Frontiers in Energy Research*, 6, pp. 1–18. doi: 10.3389/fenrg.2018.00130.
65. Pagliero, M. *et al.* (2021) ‘Effect of support on PVDF membranes for distillation process’, *Journal of Membrane Science*, 635, p. 119528. doi: 10.1016/j.memsci.2021.119528.
66. Pal, P. and Manna, A. K. (2010) ‘Removal of arsenic from contaminated groundwater by solar-driven membrane distillation using three different commercial membranes’, *Water Research*, 44(19), pp. 5750–5760. doi: 10.1016/j.watres.2010.05.031.
67. Petrova, O. E. and Sauer, K. (2012) ‘Sticky situations: Key components that control bacterial surface attachment’, *Journal of Bacteriology*, 194(10), pp. 2413–2425. doi: 10.1128/JB.00003-12.
68. Phattaranawik, J. *et al.* (2009) ‘Experimental study and design of a submerged membrane distillation bioreactor’, *Chemical Engineering and Technology*, 32(1), pp. 38–44. doi: 10.1002/ceat.200800498.
69. Politano, A. *et al.* (2017) ‘Photothermal Membrane Distillation for Seawater Desalination’, *Advanced Materials*, 29(2), pp. 1–6. doi: 10.1002/adma.201603504.
70. Qiao, H. *et al.* (2015) ‘Effective removal of cationic dyes using carboxylate-functionalized cellulose nanocrystals’, *Chemosphere*, 141, pp. 297–303. doi: 10.1016/j.chemosphere.2015.07.078.
71. Ren, B. *et al.* (2019) ‘Fe(II)-dosed ceramic membrane bioreactor for wastewater treatment: Nutrient removal, microbial community and membrane fouling analysis’, *Science of the Total Environment*, 664, pp. 116–126. doi: 10.1016/j.scitotenv.2019.02.019.
72. Roman, M. and Winter, W. T. (2004) ‘Effect of sulfate groups from sulfuric acid hydrolysis on the thermal degradation behavior of bacterial cellulose’, *Biomacromolecules*, 5(5), pp. 1671–1677. doi: 10.1021/bm034519+.

73. Ruhal, R. and Kataria, R. (2021) 'Biofilm patterns in gram-positive and gram-negative bacteria', *Microbiological Research*, 251, p. 126829. doi: 10.1016/j.micres.2021.126829.
74. Schwantes, R. *et al.* (2013) 'Membrane distillation: Solar and waste heat driven demonstration plants for desalination', *Desalination*, 323, pp. 93–106. doi: 10.1016/j.desal.2013.04.011.
75. Shirazi, S., Lin, C. J. and Chen, D. (2010) 'Inorganic fouling of pressure-driven membrane processes - A critical review', *Desalination*, 250(1), pp. 236–248. doi: 10.1016/j.desal.2009.02.056.
76. Slavin, Y. N. *et al.* (2017) 'Metal nanoparticles: Understanding the mechanisms behind antibacterial activity', *Journal of Nanobiotechnology*, 15(1), pp. 1–20. doi: 10.1186/s12951-017-0308-z.
77. Somayajula, D. *et al.* (2019) 'In Situ Synthesis of Silver Nanoparticles within Hydrogel-Conjugated Membrane for Enhanced Antibacterial Properties', *ACS Applied Bio Materials*, 2(2), pp. 665–674. doi: 10.1021/acsabm.8b00471.
78. Sun, B. *et al.* (2015) 'Sodium periodate oxidation of cellulose nanocrystal and its application as a paper wet strength additive', *Cellulose*, 22(2), pp. 1135–1146. doi: 10.1007/s10570-015-0575-5.
79. Tabraiz, S. *et al.* (2021) 'Mitigation of membrane biofouling in membrane bioreactor treating sewage by novel quorum quenching strain of Acinetobacter originating from a full-scale membrane bioreactor', *Bioresource Technology*, 334(May), p. 125242. doi: 10.1016/j.biortech.2021.125242.
80. Trache, D. *et al.* (2017) 'Recent progress in cellulose nanocrystals: Sources and production', *Nanoscale*, 9(5), pp. 1763–1786. doi: 10.1039/c6nr09494e.
81. Tripathi, B. P. (2020) 'Encyclopedia of Membranes', *Encyclopedia of Membranes*, pp. 1–3. doi: 10.1007/978-3-642-40872-4.
82. Uneputty, A. *et al.* (2022) 'Strategies applied to modify structured and smooth surfaces: A step closer to reduce bacterial adhesion and biofilm formation', *Colloids and Interface Science Communications*, 46. doi: 10.1016/j.colcom.2021.100560.
83. Valladares Linares, R. *et al.* (2014) 'Impact of spacer thickness on biofouling in

forward osmosis', *Water Research*, 57(4), pp. 223–233. doi: 10.1016/j.watres.2014.03.046.

84. Weyl, P. K. (1967) 'WEYL 3,340,186 RECOVERY OF DEMINERALIZED WATER FROM SALINE WATERS Filed May l4', *P. K*, (5), pp. 1–4.
85. Xuan, L. *et al.* (2020) 'In situ synthesizing silver nanoparticels by bio-derived gallic acid to enhance antimicrobial performance of PVDF membrane', *Separation and Purification Technology*, 251, p. 117381. doi: 10.1016/j.seppur.2020.117381.
86. Yoon, H. *et al.* (2013) 'Biofouling occurrence process and its control in the forward osmosis', *Desalination*, 325, pp. 30–36. doi: 10.1016/j.desal.2013.06.018.
87. Zahid, M. *et al.* (2021) 'Fabrication and characterization of sulfonated graphene oxide-doped polymeric membranes with improved anti-biofouling behavior', *Membranes*, 11(8). doi: 10.3390/membranes11080563.
88. Zemite, M. *et al.* (2022) 'Affordable Pretreatment Strategy for Mitigation of Biofouling in Drinking-Water Systems', *Journal of Environmental Engineering*, 148(2). doi: 10.1061/(asce)ee.1943-7870.0001968.
89. Zhang, B. *et al.* (2022) 'Pre-coagulation for membrane fouling mitigation in an aerobic granular sludge membrane bioreactor: A comparative study of modified microbial and organic flocculants', *Journal of Membrane Science*, 644, p. 120129. doi: 10.1016/j.memsci.2021.120129.
90. Zhang, H. *et al.* (2022) 'Advancing Strategies of Biofouling Control in Water-Treated Polymeric Membranes', *Polymers*, 14(6), pp. 1–23. doi: 10.3390/polym14061167.
91. Zhang, Y. *et al.* (2018) 'Surface modification of polyamide reverse osmosis membrane with organic-inorganic hybrid material for antifouling', *Applied Surface Science*, 433, pp. 139–148. doi: 10.1016/j.apsusc.2017.10.043.
92. Zhao, C. *et al.* (2021) 'Application of coagulation/flocculation in oily wastewater treatment: A review', *Science of the Total Environment*, 765, p. 142795. doi: 10.1016/j.scitotenv.2020.142795.
93. Zheng, L. *et al.* (2022) 'Insight into the microbial distribution and succession and biofouling mechanism in membrane distillation for desulfurization wastewater treatment', *Chemical Engineering Journal*, 428, p. 131097. doi:

10.1016/j.cej.2021.131097.

94. Zodrow, K. R. *et al.* (2014) ‘Biofouling and Microbial Communities in Membrane Distillation and Reverse Osmosis’, *Environmental Science and Technology*, 48(22), pp. 13155–13164. doi: 10.1021/es503051t.

Chapter 3: Equipment and techniques' overview

This chapter describes the techniques used during synthesis, as well as the equipment used for characterization. The actual synthetic procedures are described in **Chapters 4 and 5.**

3.1 Techniques used in study

The synthesis of AgNPs by CNCs was enhanced by the incorporation of microwave irradiation, while modified and unmodified PVDF membranes were synthesized using the phase inversion technique. For the preliminary assessment of anti-microbial activity, two techniques were used, including minimum inhibitory concentration (MIC) and cell viability assays, which are elaborated on.

3.1.1 Microwave irradiation

Microwave irradiation has emerged as a rapid and green process towards the synthesis of MNPs. Due to the controlled reaction conditions and uniform heating, microwave irradiation increases the rate of reaction and the product yield. Cellulosic materials have been extensively evaluated in thermally assisted methods towards the synthesis of MNPs (Kotel'nikova *et al.*, 2003). However, these reduction reactions are lengthy due to a decreased activity of the hydroxyl groups caused by intra and inter-molecular hydrogen bonding (Xu *et al.*, 2019). Hence, in this study, microwave irradiation was evaluated towards the reduction and capping of AgNPs by CNCs.

3.1.2 Phase inversion

In literature, PVDF membranes are largely prepared using two techniques, electrospinning, and phase inversion (Nejati *et al.*, 2015). Although phase inversion is the

most applied technique (**Figure 3.1**), its main disadvantage lies in the lack of systematic predictability when it comes to selecting solvents for polymer dissolution (Klein and Smith, 1972). A poor solvent choice promotes polymer aggregation in solution, with subsequent degradation of the polymer configuration and weakening of polymer mobility (Liu *et al.*, 2011). Indeed, solvents play a huge role in determining the properties and performance of the synthesized membranes and should be selected with great attention and care. Herein, phase inversion was used during the synthesis of PVDF membranes.

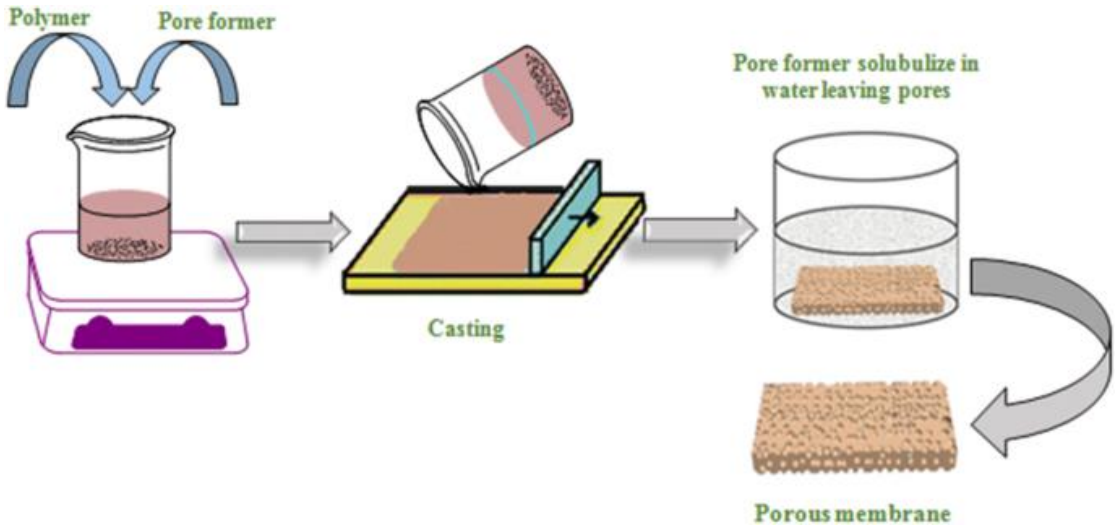

Figure 3.1: Synthesis of polymer membranes through the phase inversion technique (Malik *et al.*, 2019)

3.1.3 Minimum inhibitory concentration (MIC)

MIC is a technique that is used to quantify the extent of the susceptibility of bacterial strains to the applied anti-bacterial agent (Parvekar *et al.*, 2020). A consideration of important factors is required for the success of MIC experiments including correct method of choice and correct application of labeling rules. MIC is largely used in clinical practices for the estimation of the resistance of bacteria against various antibiotics in-vitro (Kowalska-Krochmal and Dudek-Wicher, 2021). Herein, MIC was used to estimate the

minimum concentration of CNC-capped AgNPs required to resist bacterial growth using the dilution method.

3.1.4 Cell viability

Viability of cells refers to the number of healthy cells in a specific sample (Kamiloglu *et al.*, 2020). In toxicity assays, viability of cells is crucial as it gives an indication of cell behavior in response to a chemical agent or drug applied. Garg *et al.*, (2018) studied the safety of drugs using short term viability assays. Cell viability assays are further predominantly applied in the study of cancer cells, where developed therapeutic agents are tested for effectiveness overtime (Adan, Kiraz and Baran, 2016). Various factors need to be considered for correct application of cell viability assays including sensitivity, cost, safety, efficiency, and speed (Shokrzadeh and Modanloo, 2017). This will guarantee the reliability of results. Cell-viability was used to evaluate the resistance of bacterial growth when CNC/AgNP-modified PVDF membrane is applied.

3.2 Equipment used for characterization

The characterization of the nanoparticles (NPs) and membranes was conducted using UV-vis spectroscopy, TEM, X-ray diffraction (XRD), Fourier transform infrared spectroscopy (FTIR), Thermogravimetric analysis (TGA), SEM, AFM, Dead-end filtration, inductively coupled plasma-optical fluorescence spectroscopy (ICP-OES), and a Goniometer.

3.2.1 UV/vis spectroscopy

Spectroscopy is the study of how matter interacts with light (Agilent, 2020). This light constitutes EM radiation of different wavelengths and frequencies. Gamma rays exhibit the highest frequency while radio waves exhibit the lowest frequency (Sliney, 2016). Other forms of radiation include X-rays, ultraviolet (UV) light, visible light, radio waves and

microwave radiation. UV/vis spectroscopy is a type of spectroscopic technique where light is either reflected or absorbed within the UV/visible light region (200 nm – 800 nm) (L.C. Passos and M.F.S. Saraiva, 2019). During analysis, light from a lamp is directed towards a monochromator, where screening of different radiation takes place, directing only one source of light through the sample (**Figure 3.2**). Upon light absorption by the sample, an electronic transition transpires where ground state electrons are excited towards a higher energy level, simultaneously releasing light of a particular wavelength (Rocha *et al.*, 2018). This light signal is converted to an electrical signal by a detector and can be monitored digitally. In this work, this technique was used to verify AgNPs formation through assessing the surface plasmon resonance (SPR) peak of silver.

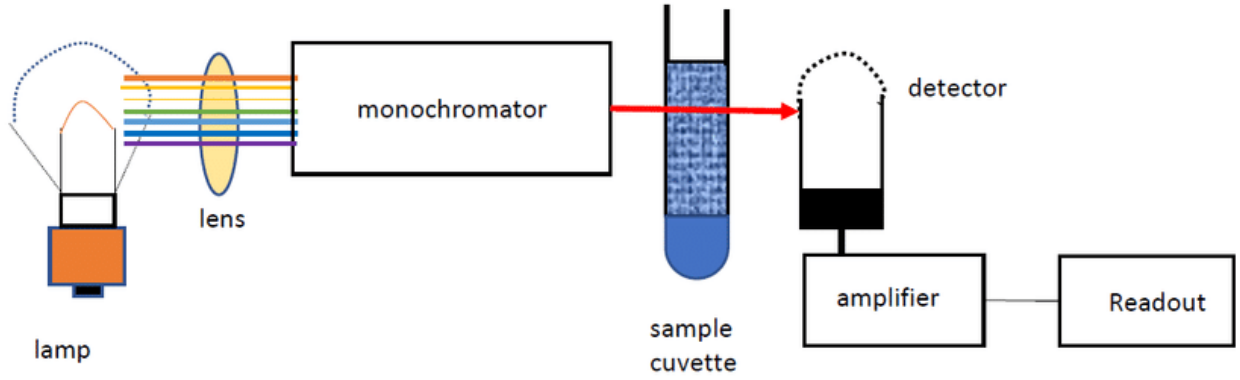

Figure 3.2: UV/vis spectroscopy principle of operation (Rahman, Arini and Utomo, 2020)

3.2.2 FTIR

FTIR gives an indication of the chemical bonds and confirms successful functionalization. The absorption of infrared radiation (IR) of the EM spectrum by a substance affords the study of its molecular structure, including the presence of different types of functional groups and chemical bonds (McMurry, 2018). This is because the absorption of infrared frequency triggers the vibration/stretching/rotation of specific bonds within a molecule (Fahelelbom *et al.*, 2022). Notably, different regions of IR exist within the EM spectrum. These include far infrared (FIR), mid infrared (MIR) and near infrared (NIR) (Veerasingam

et al., 2021). FIR is within wavenumbers ranging from 400 – 10 cm^{-1}, MIR ranges from 4000 – 400 cm^{-1} and NIR 14 000 – 4000 cm^{-1}. MIR is the region where most solids, liquids and gases absorb and is therefore the most widely used range. Exhibiting high speed and high sensitivity, FTIR further affords the verification of the quality of different material. Herein, FTIR was used to study the molecular structure of all NPs and membranes, giving an indication of the chemical bonds and confirming successful functionalization.

3.2.3 XRD

X-ray diffraction is a non-invasive technique mainly employed to study a sample's molecular structure, particularly through assessing the arrangement of atoms in space, largely crystalline material (Ali, Chiang and Santos, 2022). This is done through bombarding a material with X-ray waves from an X-ray source, followed by scattering (at specific angles) of the radiation by the electrons of that material (**Figure 3.3**). The scattered X-rays either interfere constructively or destructively. Constructive interference produces an X-ray diffraction pattern, which becomes the ultimate fingerprint of the periodic arrangement of atoms (Bunaciu, Udriştioiu and Aboul-Enein, 2015). Varying peak intensities within the diffraction pattern determines the atomic distribution within the lattice.

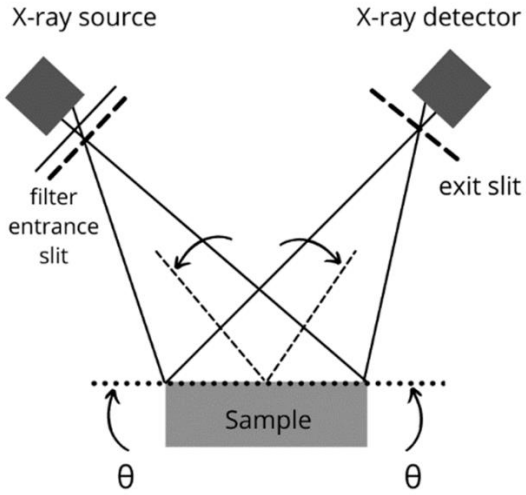

Figure 3.3: Interaction of material with X-rays (Chajec, 2021)

In addition to providing insight into the crystalline structure of a substance, XRD is also used for phase identification and mineral composition determination. Comprehensive characterization offered by XRD is crucial as the functionality of a material is directly linked to its molecular/atomic structure. Herein, XRD analysis was conducted to understand the crystalline phases of the NPs.

3.2.4 TGA

TGA is used for thermal analysis, where a sample is subjected to heat at varying/constant temperature to elucidate its physical and chemical properties (Saadatkhah *et al.*, 2020). With TGA, this involves monitoring the changes in sample mass when subjected to temperature increases (to roughly 1600 °C) (Ng *et al.*, 2018). The thermal properties of a substance depend on a number of factors including defects, presence of oxygen groups and particle size (Farivar *et al.*, 2021). In addition to thermal stability, reaction kinetics, and material structure; oxidation stabilities can also be determined with TGA (Yao *et al.*, 2022). In this study, the thermal stability of the NPs under study was evaluated using TGA.

3.2.5 TEM and SEM (coupled with EDS)

TEM analysis is conducted to understand the morphological properties of substances at better resolution (<50 pm) than SEM (~0.5 nm). In theory, TEM and SEM are a part of the electron microscopy cluster. This type of technology (in material science) applies a beam of electrons to study the specimen image (Subramanian *et al.*, 2018). Its wide applicability stems from its potential to analyze extremely small samples (<200 nm), a resolution surpassing existing light microscope's. TEM and SEM assess the atomic composition and structural imaging of different samples, as well as understand elemental composition using EDS. TEM and SEM analysis were conducted to understand the morphological properties of the NPs and membranes synthesized.

3.2.6 AFM

AFM analysis is conducted to assess the degree of membrane surface roughness. This is crucial as a high degree of surface roughness translates to increased air-pockets that minimize membrane surface energy and overall interaction with water. AFM techniques' study surface morphology of a substance through producing a 3-D image, from which surface roughness, size of nodule, hydrophobicity, and surface interactions between the sample and foulants are studied (Stawikowska and Livingston, 2013). During analysis, a fine tip (connected to a cantilever) scans back and forth on the surface of the sample, where local interactions are measured to give a recorded value (Olejnik and Nowak, 2015). This value depends on the change of the laser beam. Hence, obtaining a topical image of a substance is possible. AFM exhibits several advantages including high accuracy, reproducibility and resolution (Sazanova *et al.*, 2016). AFM analysis was conducted to assess the degree of membrane surface roughness.

3.2.7 Dead-end cell

A dead-end filtration cell (**Figure 3.4**) was used to determine membrane LEP. The importance of LEP determination lies in its ability to give an estimation of the hydraulic pressure required to run the DCMD process for a particular membrane. Operating DCMD at a pressure higher than the LEP maximizes membrane wetting, leading to a decrease in the salt rejecting efficiency of the process. However, running at hydraulic pressures lower than the LEP significantly minimizes membrane wetting. During analysis, a membrane is placed at the bottom of the cell connect to a nitrogen cylinder, with the cell filled with water. System pressure is then increased gradually until the first water drop is recorded. This minimum pressure required to drive the water through the membrane is referred to as the LEP.

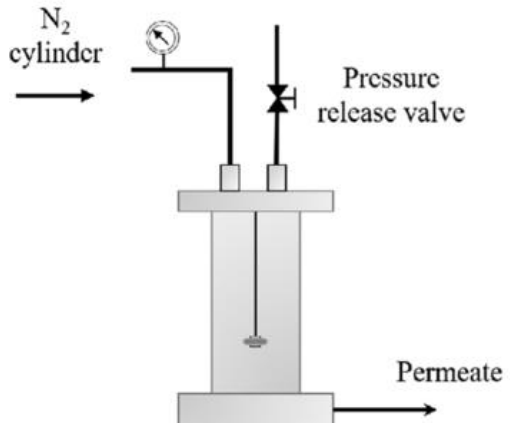

Figure 3.4: Dead-end filtration cell set up (He *et al.*, 2019)

3.2.8 Goniometer

Membrane hydrophobicity is assessed by means of measuring the WCA using a goniometer (**Figure 3.5**). Water repellency studies are crucial as they give an indication of the ability of membranes to reject water penetration. Hydrophobicity largely depends on surface roughness and surface porosity. For excellent performance of the MD system, only the permeation of gas is required through the membrane. Herein, membrane hydrophobicity was assessed by means of measuring the WCA using a goniometer, mainly through the sessile drop method. Approximately 5 – 8 µl of water is dropped on the membrane and the contact angle is measured using a goniometer, with a digital camera used to capture the contact angle. Analysis is usually run in triplicates.

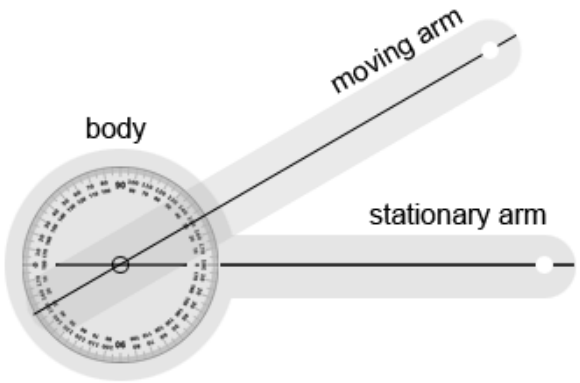

Figure 3.5: Typical goniometer used to assess WCA (Math.net, 2023)

3.2.9 ICP-OES

ICP-OES is a technique used to quantify the concentration of analytes in a sample, both in biological and environmental samples (Pröfrock and Prange, 2012). Displaying high accuracy and precision, ICP-OES further enables the analysis of the purity of pharmaceutical samples (Majumdar, Dubey and Vishwavidhyalaya, 2017). Its high sensitivity induces lower detection limits, making ICP-OES stand out amongst other ICP techniques. Notably, the analysis of negatively charged ions in ICP-OES is difficult, as only positively charged ions are discharged by the plasma (Batsala *et al.*, 2012). With regards to the principle of operation (**Figure 3.6**), a liquid sample injected via a pump into the instrument first enters the nebulizer, where phase conversion of the sample to an aerosol takes place (in the presence of Argon gas). The aerosol produced then feeds into the spray chamber (maintained at 2ºC), where droplets larger than 10 µm in diameter get screened and disposed of into the waste stream (Wilschefski and Baxter, 2019). Fine droplets then pass into the high-temperature plasma torch and get ionized, finally feeding into the ion optics and analyzer, where the ions get detected. In this work, ICP-OES was utilized to determine the concentration of silver leached from the CNC/AgNP-modified PVDF membrane over a 72-h period.

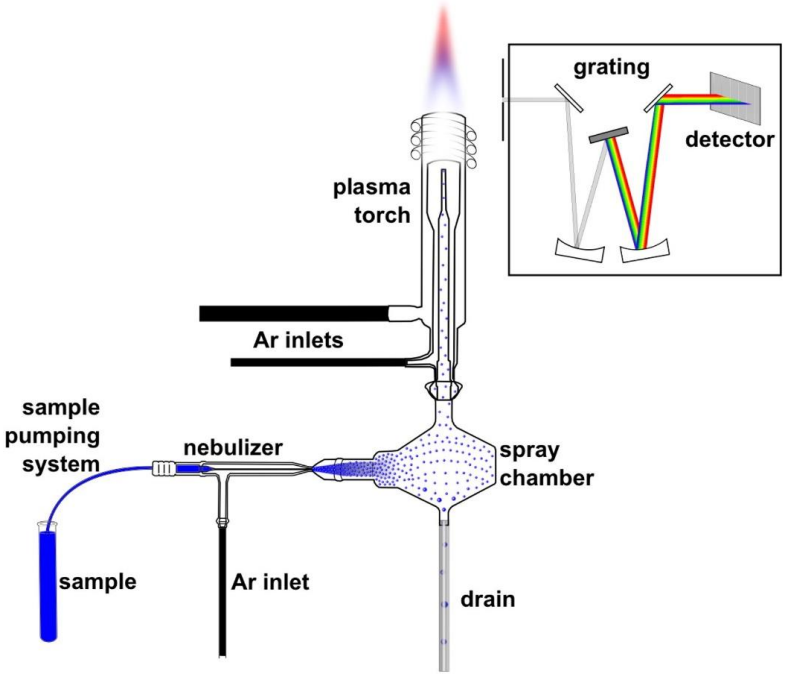

Figure 3.6: ICP-OES principle of operation (Caruso *et al.*, 2017)

3.4 References

1. Adan, A., Kiraz, Y. and Baran, Y. (2016) 'Cell proliferation and cytotoxicity assays', *Current pharmaceutical biotechnology*, 17(14), pp. 1213–1221.
2. Agilent (2020) 'The Basics of UV-Vis Spectrophotometry', p. 36. Available at: www.agilent.com/chem.
3. Ali, A., Chiang, Y. W. and Santos, R. M. (2022) 'X-Ray Diffraction Techniques for Mineral Characterization: A Review for Engineers of the Fundamentals, Applications, and Research Directions', *Minerals*, 12(2). doi: 10.3390/min12020205.
4. Batsala, M. *et al.* (2012) 'Ijrpc 2012, 2(3) International Journal of Research in Pharmacy and Chemistry Inductively Coupled Plasma Mass Spectrometry (Icp-Ms)', *Inductively Coupled Plasma Mass Spectrometry (Icp-Ms)*, 2(3), pp. 672–80.
5. Bunaciu, A. A., Udriştioiu, E. gabriela and Aboul-Enein, H. Y. (2015) 'X-Ray Diffraction: Instrumentation and Applications', *Critical Reviews in Analytical*

Chemistry, 45(4), pp. 289–299. doi: 10.1080/10408347.2014.949616.

6. Caruso, F. *et al.* (2017) 'ICP-OES method for the characterization of cement pore solutions and their modification by polycarboxylate-based superplasticizers', *Cement and Concrete Research*, 91, pp. 52–60. doi: 10.1016/j.cemconres.2016.10.007.
7. Chajec, A. (2021) 'Granite powder vs. Fly ash for the sustainable production of air-cured cementitious mortars', *Materials*, 14(5), pp. 1–26. doi: 10.3390/ma14051208.
8. Fahelelbom, K. M. *et al.* (2022) 'Recent applications of quantitative analytical FTIR spectroscopy in pharmaceutical, biomedical, and clinical fields: A brief review', *Reviews in Analytical Chemistry*, 41(1), pp. 21–33. doi: 10.1515/revac-2022-0030.
9. Farivar, F. *et al.* (2021) 'Thermogravimetric Analysis (TGA) of Graphene Materials: Effect of Particle Size of Graphene, Graphene Oxide and Graphite on Thermal Parameters', *C*, 7(2), p. 41. doi: 10.3390/c7020041.
10. Garg, S. *et al.* (2018) 'Integration of conventional cell viability assays for reliable and reproducible read-outs: Experimental evidence', *BMC Research Notes*, 11(1), pp. 1–7. doi: 10.1186/s13104-018-3512-5.
11. He, M. *et al.* (2019) 'High-performance acid-stable polysulfonamide thin-film composite membrane prepared via spinning-assist multilayer interfacial polymerization', *Journal of Materials Science*, 54. doi: 10.1007/s10853-018-2847-6.
12. Kamiloglu, S. *et al.* (2020) 'Guidelines for cell viability assays', *Food Frontiers*, 1(3), pp. 332–349. doi: 10.1002/fft2.44.
13. Klein, E. and Smith, J. K. (1972) 'Asymmetrie Membrane Formation. Solubility Parameters for Solvent Selection', *Industrial and Engineering Chemistry Product Research and Development*, 11(2), pp. 207–210. doi: 10.1021/i360042a017.
14. Kotel'nikova, N. E. *et al.* (2003) 'Mechanisms of Diffusion-Reduction Interaction of Microcrystalline Cellulose and Silver Ions', *Russian Journal of General Chemistry*, 73(3), pp. 427–433. doi: 10.1023/A:1024966121771.
15. Kowalska-Krochmal, B. and Dudek-Wicher, R. (2021) 'The minimum inhibitory concentration of antibiotics: Methods, interpretation, clinical relevance',

Pathogens, 10(2), pp. 1–21. doi: 10.3390/pathogens10020165.

16. L.C. Passos, M. and M.F.S. Saraiva, M. L. (2019) 'Detection in UV-visible spectrophotometry: Detectors, detection systems, and detection strategies', *Measurement: Journal of the International Measurement Confederation*, 135, pp. 896–904. doi: 10.1016/j.measurement.2018.12.045.
17. Liu, F. *et al.* (2011) 'Progress in the production and modification of PVDF membranes', *Journal of Membrane Science*, 375(1–2), pp. 1–27. doi: 10.1016/j.memsci.2011.03.014.
18. Majumdar, A. J., Dubey, N. and Vishwavidhyalaya, D. A. (2017) 'I j p l s', 8(1), pp. 5420–5425.
19. Malik, T. *et al.* (2019) 'Design and synthesis of polymeric membranes using water-soluble pore formers: an overview', *Polymer Bulletin*, 76(9), pp. 4879–4901. doi: 10.1007/s00289-018-2616-3.
20. McMurry, J. (2018) 'Periodic Table of the Elements', *Properties and Selection: Nonferrous Alloys and Special-Purpose Materials*, pp. 1098–1098. doi: 10.31399/asm.hb.v02.a0001116.
21. Nejati, S. *et al.* (2015) 'Engineering flat sheet microporous PVDF films for membrane distillation', *Journal of Membrane Science*, 492, pp. 355–363. doi: 10.1016/j.memsci.2015.05.033.
22. Ng, H. M. *et al.* (2018) 'Thermogravimetric Analysis of Polymers', *Encyclopedia of Polymer Science and Technology*, pp. 1–29. doi: 10.1002/0471440264.pst667.
23. Olejnik, A. and Nowak, I. (2015) 'Atomic force microscopy analysis of synthetic membranes applied in release studies', *Applied Surface Science*, 355, pp. 686–697. doi: 10.1016/j.apsusc.2015.07.145.
24. Parvekar, P. *et al.* (2020) ' The minimum inhibitory concentration (MIC) and minimum bactericidal concentration (MBC) of silver nanoparticles against Staphylococcus aureus ', *Biomaterial Investigations in Dentistry*, 7(1), pp. 105–109. doi: 10.1080/26415275.2020.1796674.
25. Pröfrock, D. and Prange, A. (2012) 'Inductively coupled plasma-mass spectrometry (ICP-MS) for quantitative analysis in environmental and life sciences: A review of challenges, solutions, and trends', *Applied Spectroscopy*, 66(8), pp.

843–868. doi: 10.1366/12-06681.

26. Rahman, H., Arini, S. F. and Utomo, V. (2020) ‘Tannins Extraction of Tea Leaves by Ultrasonic Method: Comparison with The Conventional Method’, *Jurnal Teknologi*, 8(1), pp. 84–95. doi: 10.31479/jtek.v1i8.62.
27. Rocha, F. S. *et al.* (2018) ‘Experimental methods in chemical engineering: Ultraviolet visible spectroscopy—UV-Vis’, *Canadian Journal of Chemical Engineering*, 96(12), pp. 2512–2517. doi: 10.1002/cjce.23344.
28. Saadatkhah, N. *et al.* (2020) ‘Experimental methods in chemical engineering: Thermogravimetric analysis—TGA’, *Canadian Journal of Chemical Engineering*, 98(1), pp. 34–43. doi: 10.1002/cjce.23673.
29. Sazanova, T. S. *et al.* (2016) ‘An atomic force microscopy study of hybrid polymeric membranes: Surface topographical analysis and estimation of pore size distribution’, *Petroleum Chemistry*, 56(5), pp. 427–435. doi: 10.1134/S096554411605011X.
30. Shokrzadeh, M. and Modanloo, M. (2017) ‘An overview of the most common methods for assessing cell viability’, *J. Res. Med. Dent. Sci*, 5(2), pp. 33–41.
31. Sliney, D. H. (2016) ‘What is light? the visible spectrum and beyond’, *Eye (Basingstoke)*, 30(2), pp. 222–229. doi: 10.1038/eye.2015.252.
32. Stawikowska, J. and Livingston, A. G. (2013) ‘Assessment of atomic force microscopy for characterisation of nanofiltration membranes’, *Journal of Membrane Science*, 425–426, pp. 58–70. doi: 10.1016/j.memsci.2012.08.006.
33. Subramanian, K. S. *et al.* (2018) ‘A Textbook on Fundamentals and Applications of Nanotechnology’, *Kemampuan Koneksi Matematis (Tinjauan Terhadap Pendekatan Pembelajaran Savi)*, 53(9), pp. 81–92.
34. Veerasingam, S. *et al.* (2021) ‘Contributions of Fourier transform infrared spectroscopy in microplastic pollution research: A review’, *Critical Reviews in Environmental Science and Technology*, 51(22), pp. 2681–2743. doi: 10.1080/10643389.2020.1807450.
35. Wilschefski, S. C. and Baxter, M. R. (2019) ‘Inductively Coupled Plasma Mass Spectrometry: Introduction to Analytical Aspects’, *Clinical Biochemist Reviews*, 40(3), pp. 115–133. doi: 10.33176/AACB-19-00024.

36. Xu, Q. *et al.* (2019) ‘Synthesis of silver nanoparticles using dialdehyde cellulose nanocrystal as a multi-functional agent and application to antibacterial paper’, *Cellulose*, 26(2), pp. 1309–1321. doi: 10.1007/s10570-018-2118-3.
37. Yao, F. *et al.* (2022) ‘Thermogravimetric Analysis on a Resonant Microcantilever’, *Analytical Chemistry*, 94(26), pp. 9380–9388. doi: 10.1021/acs.analchem.2c01374.

Chapter 4: Cellulose nanocrystal-mediated synthesis of silver nanoparticles via microwave assisted methods for preliminary anti-microbial evaluation against Gram-negative and Gram-positive bacteria

4.1 Introduction

The application of metal nanoparticles (MNPs) in the fields of biomedical science, catalysis and water technology has sparked great interest in research (Jatoi *et al.*, 2019). AgNPs are MNPs exhibiting sizes ranging from 1 – 100 nm (Ma *et al.,* 2021). Their antimicrobial use has gained momentum in medicinal application, dental materials and stainless steel materials (Xu *et al.,* 2019). The goal of AgNPs' synthesis is to produce monodisperse colloids with little variation in size and a relatively good yield (Stinson-Bagby *et al*., 2019). To minimize the conventional use of toxic reducing agents (e.g., sodium borohydride) in synthesizing AgNPs, ecofriendly methods have emerged, including the use of plant-based products such as cellulose.

Cellulose is the most abundant biopolymer consisting of repeating D-glucose units linked together through β(1→4) glycosidic bonds (Panchal, Ogunsona and Mekonnen, 2019). Cellulose is engineered to a nanostructured form called nanocelluloses (NCs) with the purpose of improving its biophysical properties (Trache *et al.*, 2020). Having high surface to volume ratio, NCs are composed of microfibrillated cellulose (MFC), nanofibrillated cellulose (NFC) and CNCs (Ma *et al.*, 2021). The high surface area of CNCs is able to prevent AgNPs' aggregation through providing sufficient space (as support) for AgNPs' dispersion (Xu *et al.,* 2019). It is the thermodynamic instability of AgNPs that require stabilizing agents to prevent aggregation (Cieśla *et al.,* 2020). The current study assessed the bio-mediated synthesis of AgNPs for their preliminary antibacterial evaluation against Gram-negative and Gram-positive bacterial strains. This involved the exploration of microwave-assisted methods. The preliminary evaluation of the CNC/AgNP-modified PVDF membrane to inhibit microbial growth was also assessed.

4.2 Materials and methods

4.2.1 Materials

Silver nitrate ($AgNO_3$, Mw = 169.87 g/mol), dimethylformamide (DMF, ACS reagent, 99%), Dimethylacetamide (DMac, ACS reagent, 99%), Dimethyl sulfoxide (DMSO, ACS reagent, 99%), polyvinylidene fluoride (PVDF, Mw = 534,000 g/mol), polyvinylpyrrolidone (PVP, Mw = 360,000 g/mol), NaOH (sodium hydroxide, pellets, Mw = 39.99 g/mol), Resazurin sodium sulphate salt (Mw = 251.17 g/mol) and Streptomycin were purchased from Sigma Aldrich (Germany). Cellulose nanocrystals (CNCs) were procured from Nanografi Nano Technology and CNTs from SabiNano (Pty) Ltd. Mueller Hinton broth (MHB) and Mueller Hinton agar (MHA) were procured from Sisco Research Laboratories (Pvt) Ltd. All reagents were used as received. Ultrapure water was obtained from a Direct-Q® system (resistivity: 18 MΩ cm, Merck, Millipore) produced in our laboratory. Bacterial strains used in these studies were obtained from Prof Hope Dlamini (University of Johannesburg) and included *S. aureus* NCTC 6571, *S. saprophyticus* ATCC 15305, *E. coli* ATCC 25922, *P. aeruginosa* ATCC 27853 and *S. epidermis* ATCC 14990.

4.2.2 Methods

a) Preparation of CNC-capped AgNPs

AgNPs were prepared following a modified greener approach (Chen *et al.*, 2008). Specifically, 50 mL of $AgNO_3$ (0.1 M) was added into a flask containing 100 mL of CNCs (1 mg/mL). The pH of the resulting mixture was adjusted to 10 using NaOH (0.1 M). The reduction of Ag^+ ions was performed in a microwave reactor at the following conditions: power setting, stirring speed, and temperature of 500 W, 600 rpm, and 60 ºC, respectively. Aliquot samples were taken at 5, 10, 15, 30, 60, 120, 180 min time intervals for UV-Vis

analysis. The resulting CNC-capped AgNPs were centrifuged at 48,000 rpm to separate them from the supernatant and dried in the oven at 60 ºC.

b) Preparation of PVDF membranes

Polymeric (PVDF) membranes were prepared using the phase inversion technique. Briefly, a solution of 15% PVDF was prepared using a mixed solvent system of DMac and DMF (3:2 v/v ratio) and various non-solvent additives according to the requirements of each membrane (**Table 4.1**). The polymer solution containing the reagents was stirred until full dissolution followed by degassing. The solution was cast on a glass plate using a casting knife film applicator, maintaining the gap size at 60 µm. The wet films were immersed in a water bath and coagulated for 24 h, followed by air-drying for 48 h. The specific synthesis of *f*-CNTs is presented in **Chapter 5**. For the purposes of this chapter, only M1 and M4 were used to evaluate the preliminary anti-microbial performances of the membranes.

Table 4.1: Casting solution composition for each membrane

Membrane	DMAc (g)	DMF (g)	PVDF (g)	PVP (g)	*f*-CNTs (g)	CNC-capped AgNP (g)
M1	51.0	34.0	15.0	-	-	-
M2	51.0	33.9	15.0	0.1	-	-
M3	50.6	33.8	15.0	0.1	0.5	-
M4	47.0	31.4	15.0	0.1	0.5	7

c) Characterization of CNC-capped AgNPs

Characterization of the synthesized nanoparticles ((NPs) referring to CNC-capped AgNPs) was conducted via UV-vis spectroscopy, TEM coupled with EDS, XRD, FTIR, and TGA. The characterization of the membranes is presented in **Chapter 5**.

UV–vis spectroscopic analysis of the NPs was carried out using PerkinElmer UV-Vis spectrometer Lambda 6505 instrument at room temperature. Prior to analysis, the wavelength range was set at 200–800 nm. TEM analysis was conducted using FEI Tecnai T12 TEM to understand NPs' morphological properties. Prior to analysis, samples were dissolved in a solvent (methanol) and sonicated for 5 mins to afford maximum dispersion. Then, a Pasteur pipette was used to place a drop of the sonicated sample on a copper grid, removing excess water using a paper towel. The samples were analyzed, and the resultant TEM images used to determine the particle size distribution using the Image J Pro software. EDS analysis was used to determine the elemental composition of the samples.

The crystalline structure of the NPs was analyzed using Bruker D2 X-ray diffraction (XRD), with a scanning range of 5–80º. The thermal stability of the NPs was evaluated through using Perkin Elmer STA 6000 thermal analyzer. Analysis was conducted at a pressure, heating rate, nitrogen gas rate, and temperature range of 4 bar, 10 ºC/min, 20 mL/min, and 35–900 ºC, respectively. FTIR analysis was conducted using Tensor 27 FTIR (Bruker South Africa PTY LTD) at a scanning wavenumber of 500–4000 cm^{-1} for analysis of the chemical functional groups of the NPs.

4.2.3 Preliminary antimicrobial tests

The overall goal of this research was to develop a biofouling resistant PVDF membrane for use in MD. Therefore, it was imperative to test the antimicrobial properties of the additives (pristine CNC-capped AgNPs). The antibacterial tests of CNC-capped AgNPs were performed using MIC against Gram-negative and Gram-positive bacterial strains, including *S. aureus* NCTC 6571, *S. saprophyticus* ATCC 15305, *E. coli* ATCC 25922, *P. aeruginosa* ATCC 27853 and *S. epidermis* ATCC 14990. Cell viability tests were carried out using the same strains of bacteria to assess the preliminary evaluation of the CNC/AgNP-modified PVDF membrane to control bacterial growth *in-situ*.

a) Minimum inhibitory concentration (MIC)

To determine the MIC of the CNC-capped AgNPs required to achieve antibacterial activity, strains were cultured in MHB at 30 ℃ and incubated for 24 h. The 0.5 McFarland standard was used to obtain the optimal density of the cultured bacteria. The Streptomycin antibiotic (10 mg/mL) was used as the positive control. The stock solution of the synthesized CNC-capped AgNPs was prepared through dissolution of 5 mg CNC-capped AgNPs in 1 mL 0.1% w/v DMSO, obtaining a final concentration of 5 mg/mL. Further standards were prepared through serial dilutions to obtain 2.5 mg/mL, 1.25 mg/mL, 0.625 mg/mL, 0.312 mg/mL, and 0.156 mg/mL solutions of CNC-capped AgNPs. Using aseptic techniques, 100 µL of the bacterial suspension and 100 µL of the CNC-capped AgNPs suspension were added into a 96 well-plate (with two repeats), followed by incubation at 30 ℃ for 24 h. After incubation, 10 µL of the resazurin sodium salt solution (0.2% w/v) was added into the wells of the plate to establish the bacterial growth colorimetric assay. Change in colour to pink signified the presence of live bacterial cells.

b) Cell viability

Cell-viability assay was used to evaluate the preliminary bacterial growth resistance of the CNC/AgNP-modified PVDF membrane. All glassware and solutions used were sterilized through autoclaving. Bacterial broth prepared within 48 h was used during these experiments. Following incubation, the collection of bacterial cells was done through centrifugation and subsequent washing with sterile deionized water. Thereafter, the resuspension of bacterial cells was carried out in a 0.9% NaCl solution for the removal of cell debris. Membranes were placed in a 30 mL bacterial suspension and incubated at 30 ℃ for 24 h with agitation at 160 rpm. Finally, bacterial concentration in the solution was determined by measuring the optical density (OD).

4.3 Results and discussion

4.3.1 Characterization of CNC-capped AgNPs

a) UV-Vis analysis of CNC-capped AgNPs

The bio-mediated synthesis of AgNPs was successfully conducted via an in-situ reaction. The reduction of Ag^{+} ions to their counterpart AgNPs was observed through a colour change from clear to brown and finally black (**Figure 4.1b**). To ascertain the formation of AgNPs, UV-Vis spectroscopic analysis was carried out (**Figure 4.1a**). Notably, maximum absorbance occurred at a wavelength range of 425–443 nm, corresponding to the surface plasmon resonance of AgNPs. Similar observations were reported in other studies (Sunitha *et al.*, 2013; Lokanathan *et al.*, 2014). The increase in intensity of the colour change leading to the increase in absorbance was recorded as a function of time during microwave irradiation. This change correlated with an increase in the production of AgNPs (**Figure 4.1b**). Nonetheless, the production of AgNPs became less rapid at higher irradiation time (between 30 and 180 min), as the reaction was reaching equilibrium.

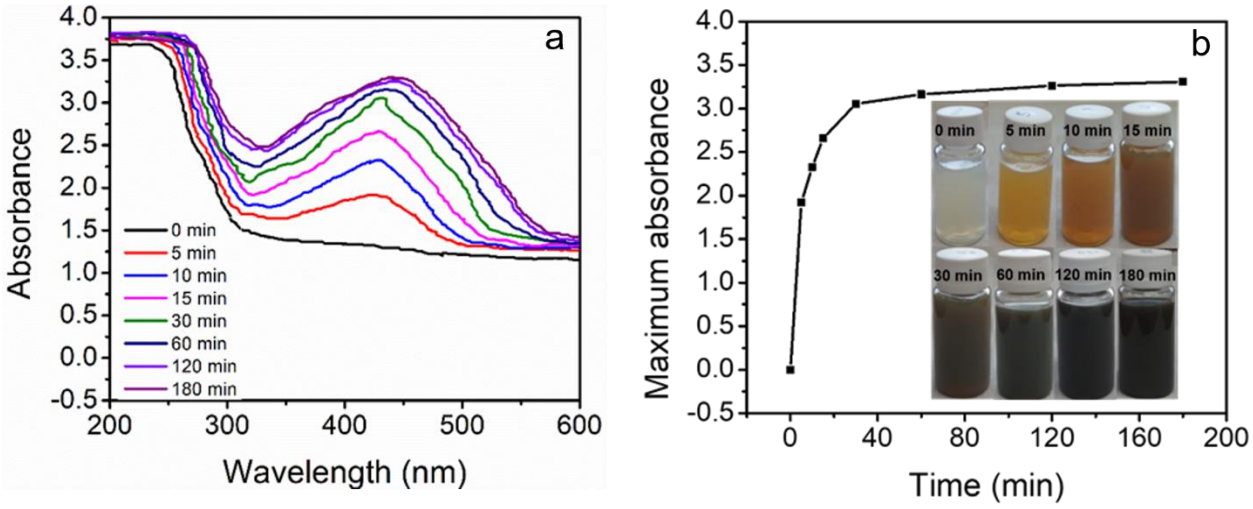

Figure 4.1: UV−vis absorbance spectra of CNC-capped AgNPs

b) AgNPs' chemical reduction and capping by CNCs

In terms of the proposed reaction mechanism, positive Ag^{+} ions in solution first attached to the electron-rich hydroxyl group on the CNCs' surface, forming a complex through electrostatic interactions. This was then followed by the nucleation and growth of AgNPs on CNCs (**Figure 4.2**). The attachment of AgNPs on CNCs was confirmed by TEM analysis.

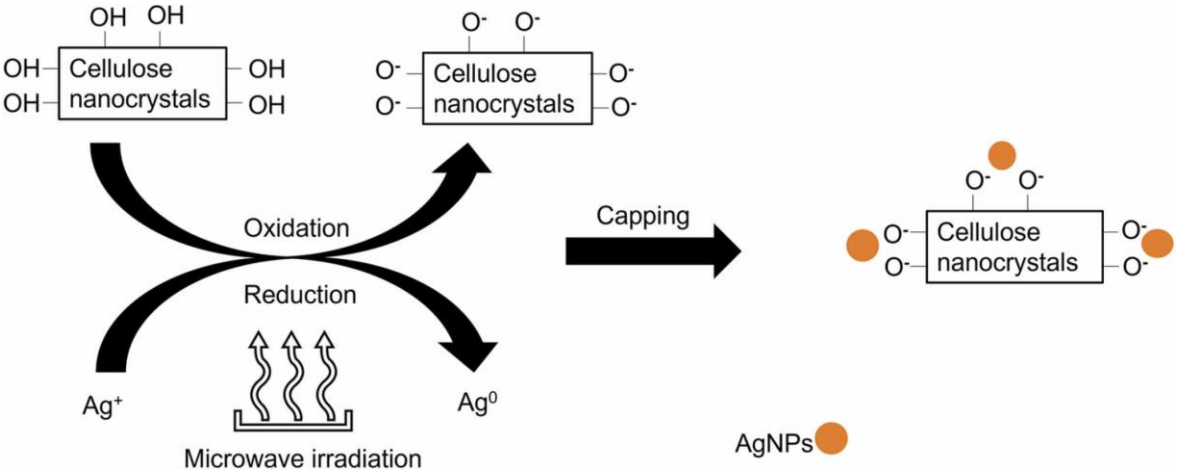

Figure 4.2: Schematic illustration of the chemical reduction of AgNPs by CNCs and their subsequent adherence on the surface

c) TEM analysis of CNC-capped AgNPs

The TEM micrograph of CNC-capped AgNPs and the corresponding particle size distribution plot are illustrated in **Figure 4.3**. AgNPs were unevenly dispersed on the surface of CNCs, with several clusters forming minimal particle agglomeration. The dispersion of AgNPs was due to the electrostatic repulsions arising from the negatively charged hydroxyl groups anchoring the AgNPs. The anchoring ability of CNCs was further proven by the absence of free AgNPs between the substrate (Hanif *et al.*, 2021). AgNPs

were predominantly spherical in shape, exhibiting an average particle size of 13.3 ± 3.94 nm (**Figure 4.3a**). Smaller-sized AgNPs are desirable as they have better contact with the bacteria, enhancing their overall anti-microbial activity.

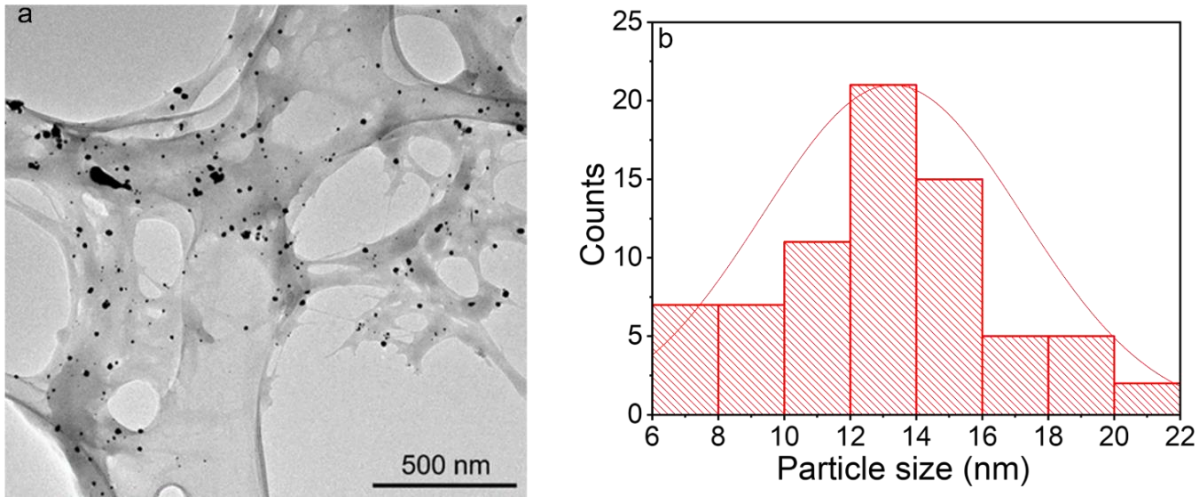

Figure 4.3: Transmission electron micrograph of CNC-capped AgNPs (a), coupled with the corresponding histogram plot (b)

d) XRD analysis of CNCs and CNC-capped AgNPs

To understand the crystal structure of CNCs and CNC-capped AgNPs, XRD analysis was conducted (**Figure 4.4**). The diffraction peaks of CNCs at 2θ = 14.9°, 22.1°, and 34.1° were attributed to (110), (200) and (004) crystal planes of cellulose, respectively (Xu *et al.*, 2019). Upon AgNPs interaction with CNCs, new diffraction peaks emerged, markedly at 2θ = 38.1°, 43.4°, 64.5°, 77.2° and 82.1°. These were attributed to (111), (200), (220), (311) and (222) crystal planes of cubic silver, respectively (Wang *et al.*, 2009; Yu *et al.*, 2014). The peak intensities of crystal planes (200), (111) and (110) were considerably larger than others, signifying their effective ability to diffract X-rays.

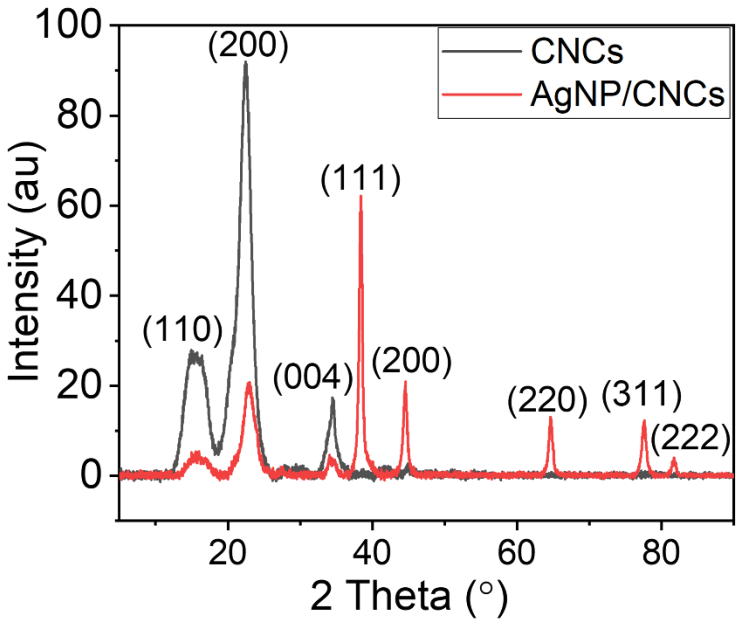

Figure 4.4: XRD spectra of CNCs and CNC-capped AgNPs

e) FTIR analysis of CNCs and CNC-capped AgNPs

The FTIR spectra of CNCs and CNC-capped AgNPs is illustrated in **Figure 4.5**. For CNCs, the broad peak at 3328 cm^{-1} was attributed to the symmetric and asymmetric stretching of the OH functional groups on the surface of CNCs (Yu *et al.*, 2014). The band position of the C-O-C peak at 1014 cm^{-1} demonstrated a significantly strong intensity of adsorption, forming part of the bulk material of cellulose (Jatoi *et al.*, 2019). The peaks at 2906 cm^{-1} and 1315 cm^{-1} were attributed to the stretching C-H alkyl peak and the bending C-H peak, respectively. There was a significant decline in intensity of the OH peak (as well as a shift toward a lower wavenumber) for the CNC-capped AgNPs, potentially due to the interaction of AgNPs with the OH groups. Similar results were obtained elsewhere (Xu *et al.*, 2019), although their shift in position of the OH peak was towards a higher wavenumber. These alterations in spectra imply the significant role that OH groups play in forming and stabilizing AgNPs (Toro *et al.*, 2021). There was also a slight shift in the C-O-C band position from 1014 cm^{-1} to 990 cm^{-1}, denoting the physical deposition of AgNPs

(Badawy *et al.*, 2021). The appearance of the absorption band at 1240 cm^{-1} demonstrated the formation of an ester group, a product of cellulose decarboxylation.

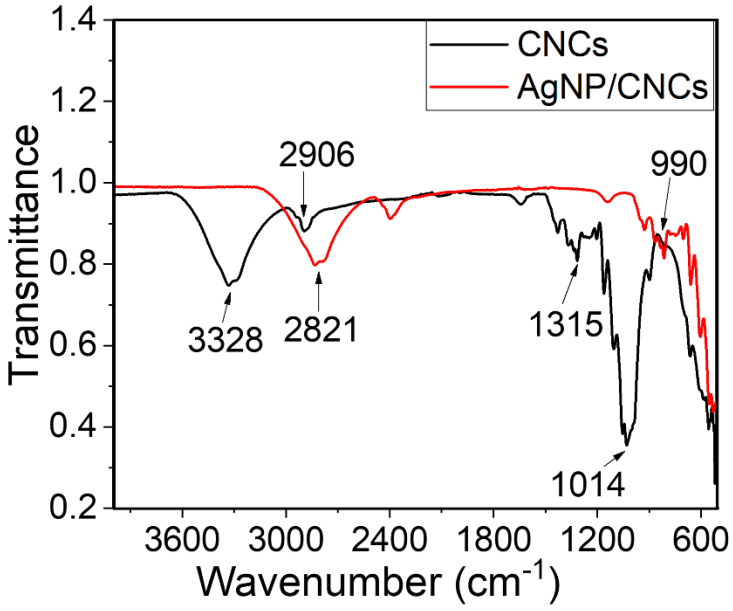

Figure 4.5: FTIR spectra of CNCs and CNC-capped AgNPs

f) TGA analysis of CNCs and CNC-capped AgNPs

The thermal properties of CNCs and CNC-capped AgNPs was assessed, and the spectra presented in **Figure 4.6**. Reduced sample weight near 100℃ (**Figure 4.6a)** was attributed to the loss of absorbed water (Zhu *et al.*, 2021). At 272℃ and 331℃, mass loss of CNCs to 93.9% and 40.9% was attributed to the depolymerization and dehydration of cellulose glycosyl units (Lizundia *et al.*, 2018). Upon capping of AgNPs, the mass loss of CNCs occurred at 335℃, signifying increased thermal stability. Evidently, CNC-capped AgNPs exhibited more weight (18%) at 900℃ than pristine CNCs (15%), mainly due to the enhanced thermal stability induced by the incorporation of AgNPs. The AgNPs acted as flame retardants, increasing the mass of the charred fraction of the residue (Yu *et al.*, 2014). Moreover, due to the favored synthesis of more AgNPs at higher pH, alkalinization of the reaction medium enhanced the thermal stability (Hoeng *et al.*, 2015).

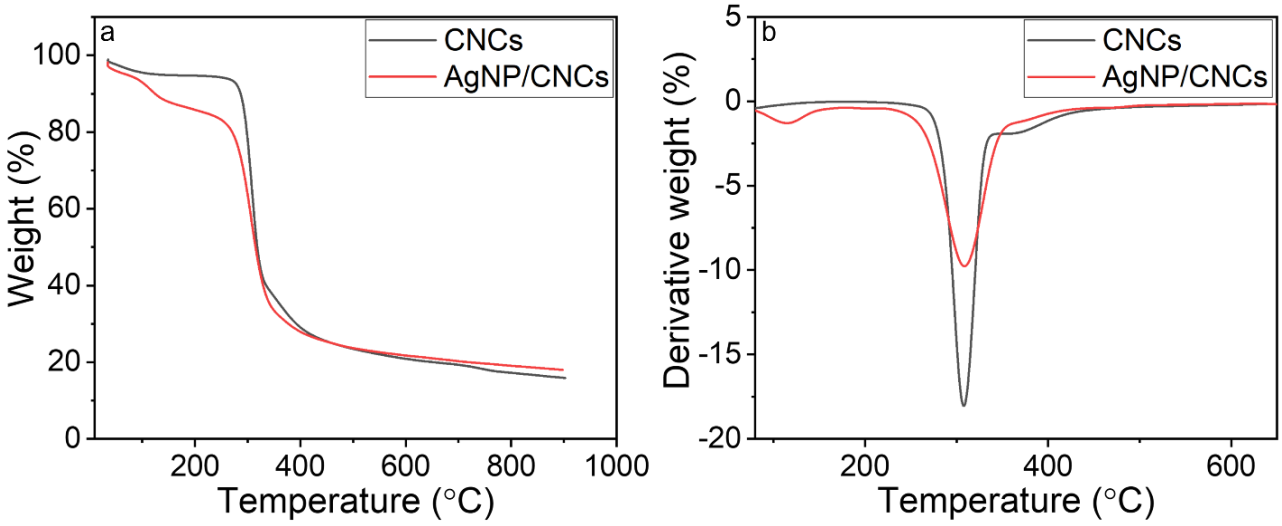

Figure 4.6: TGA (a) and DTG (b) curves for CNCs and CNC-capped AgNPs

g) EDS analysis of CNCs and CNC-capped AgNPs

Figure 4.7 depicts the EDS spectra of CNCs and CNC-capped AgNPs. The presence of elemental sulphur stems from acidic preparations of CNCs, where sulphuric acid was used to purify CNCs (as noted from the suppliers). Carbon and oxygen on the spectra constitute the chemical backbone of cellulose, with carbon being the most predominant element. The successful deposition of AgNPs on the surface of CNCs was further confirmed, with elemental silver showing at 3 kiloelectron volts (keV) (Ma *et al.*, 2021).

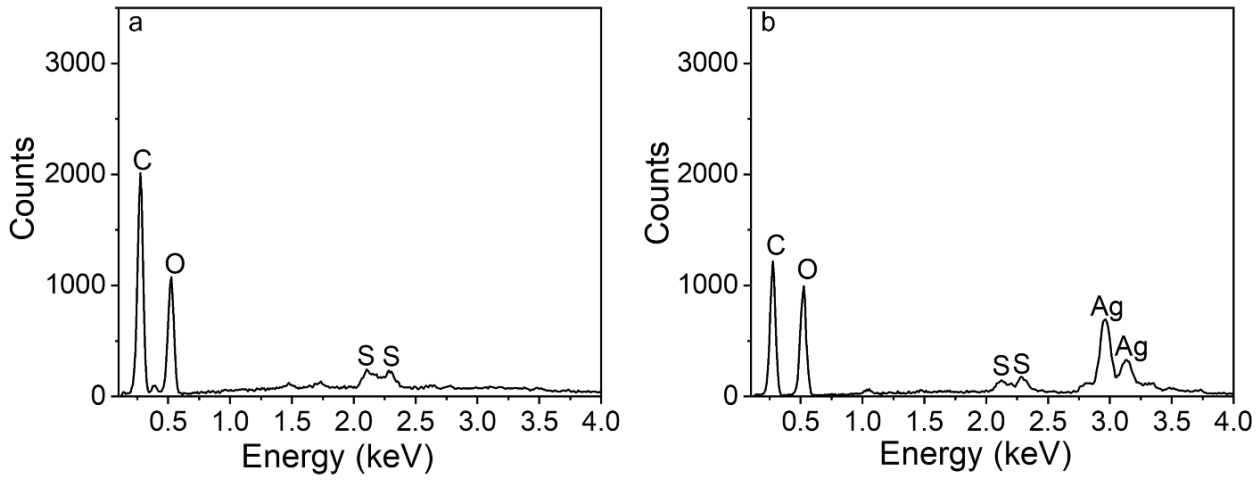

Figure 4.7: EDS spectra of CNCs (a) and CNC-capped AgNPs (b)

4.3.2 Preliminary antimicrobial tests

MIC and cell viability assays were used for the preliminary evaluation of anti-microbial performance of CNC-capped AgNPs and CNC/AgNP-modified PVDF membrane.

a) MIC

To determine MIC, a 96 well plate assay was used. MIC gives an indication of bacterial resistance against antimicrobial compounds (Nthunya *et al.*, 2017). In this work, different concentrations of CNC-capped AgNPs were tested against Gram-negative and Gram-positive bacterial strains, using resazurin sodium sulphate salt as the indicator of the presence/absence of bacterial growth. Since the addition of the resazurin salt renders all inner wells purple, any further colour changes from purple to pink (following the 2 h incubation period) would signify oxygen decrease in the medium, subsequently signifying the activity of live microbial cells (Hanif *et al.*, 2021; Lulamba, Green and Serepa-Dlamini, 2021). It is evident from **Figure 4.9** that CNC-capped AgNPs displayed excellent bacterial growth inhibition with many cells remaining purple while pristine CNCs did not (**Figure 4.8**), specifically due to the absence of AgNPs (Xiong *et al.*, 2013). The MIC values of

CNC-capped AgNPs ranged from 1.25 mg/mL to 2.50 mg/mL, with 1.25 mg/mL being observed for *E. coli* and *P. aeruginosa*, and 2.50 mg/mL being observed for *S. aureus, S. epidermis and S. saprophyticus* (**Table 4.2**). Notably, the antibacterial activity of CNC-capped AgNPs was higher for *E. coli*, and *P. aeruginosa* compared to *S. aureus, S. epidermis and S. saprophyticus*. Similar results were reported elsewhere (Liu *et al.*, 2012). *E. coli* and *P. aeruginosa* are Gram–negative bacteria characterized by a thin peptidoglycan cell wall, capable of facilitating the easy penetration of AgNPs within the cell and causing cell death (Hori and Matsumoto, 2010). Moreover, since the oxidation of AgNPs produced Ag^+ ions, a strong electrostatic interaction may have resulted between the negatively charged bacterial cell wall and the positively charged Ag^+ ions, resulting in better antibacterial activity.

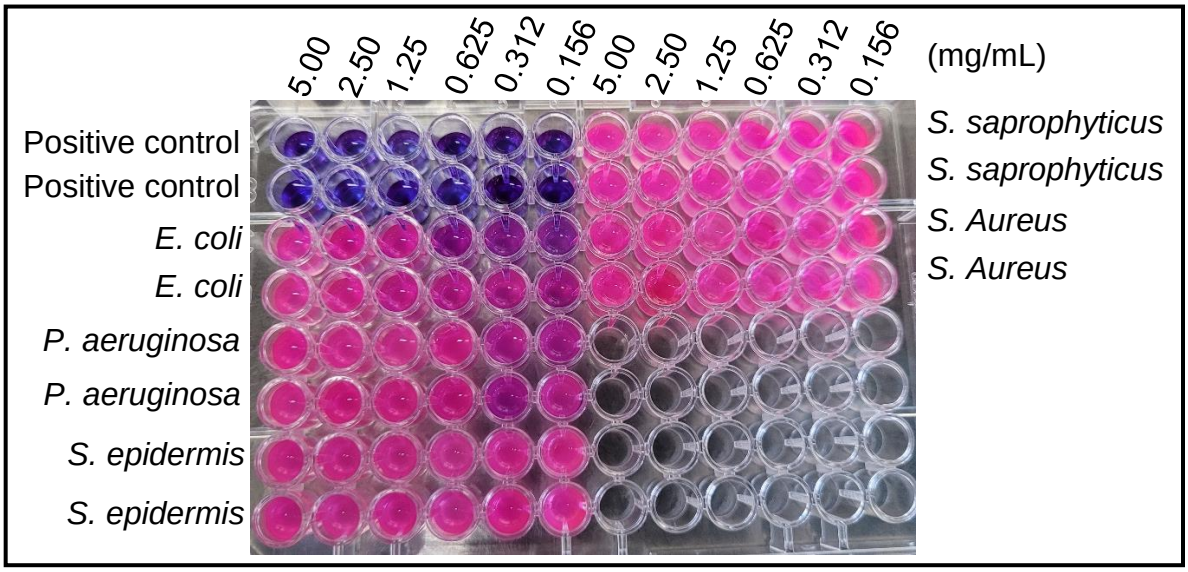

Figure 4.8: MIC of CNCs

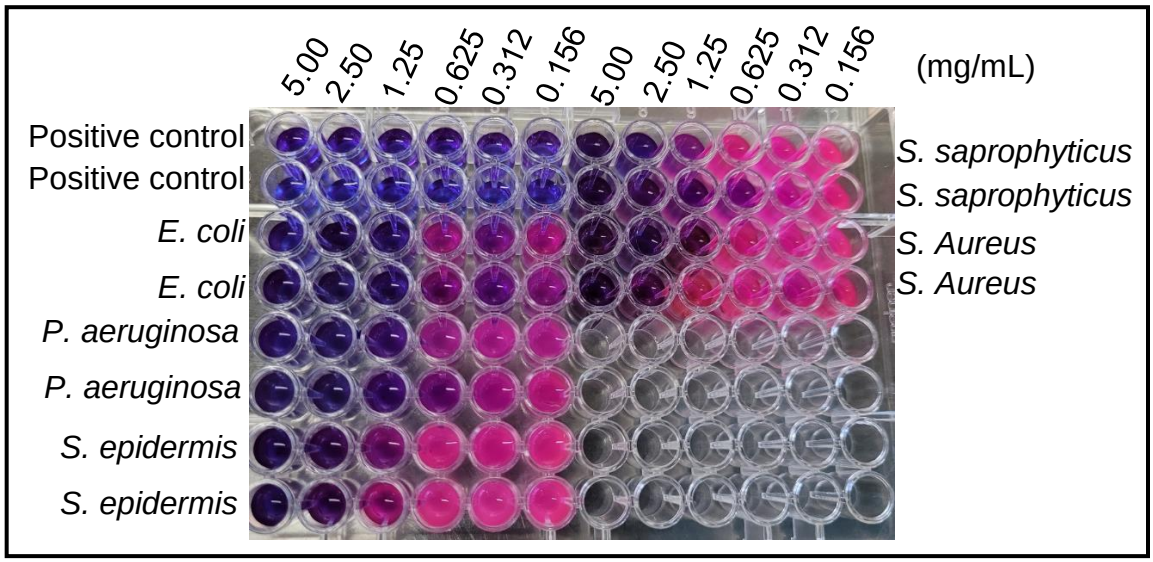

Figure 4.9: MIC of CNC-capped AgNPs

Table 4.2: MIC values of CNC-capped AgNPs against the different bacterial strains

Test strain	CNC-capped AgNPs MIC (mg/mL)
E.coli	1.25
S. Aureus	2.50
S. Epidermis	2.50
S. Saprophyticus	2.50
P. Aeruginosa	1.25

b) Cell viability

Cell viability refers to a measure of a cell's physiological health upon extracellular interaction with antibacterial agents (Kamiloglu *et al.*, 2020). In this work, cell viability was used to assess the preliminary antibacterial activity of CNC/AgNP-modified PVDF membrane prior to application in MD. Viability of cells was measured through measuring the optical density (at 600 nm) of the bacterial culture following contact with the membrane. Notably, pristine PVDF did not display a significant reduction in cell population

(**Table 4.3**). This was associated with weak interactions between the bacteria and the un-modified membrane (Wang *et al.*, 2019). Specifically*, E. coli, P. aeruginosa*, *S. aureus*, *S. epidermis*, *S. saprophyticus* strains were reduced by 1.21%, 0.733%, 2.29%, 0.786% and 0.663%, respectively. However, a significant reduction in cell population was attained upon contact of the CNC/AgNP-modified PVDF membrane with the bacterial suspension. This was induced by minimal bacterial growth caused by the presence of AgNPs embedded on the membrane. Evidently*, E. coli, P. aeruginosa, S. aureus, S. epidermis, and S. saprophyticus* strains were reduced by 98.7%, 52.3%, 78.0%, 53.9% and 93.3%, respectively. The high sensitivity of *E. coli* cells toward AgNPs was further reported elsewhere (Wang *et al.*, 2019). Though the mechanism of the antibacterial activity of AgNPs is somewhat unclear, it has been proposed to follow one of three paths: (1) penetration of the AgNPs into the cell enhanced by its small radii, promoting its interaction with the thiol functional groups and subsequently lead to cell death, (2) reaction of the AgNPs with sulfhydryl groups of the bacterial membrane, subsequently decreasing cell membrane energy and ultimately lead to cell death and (3) deactivation of antioxidative enzymes caused by a rise in reactive oxygen species (ROS) levels (Stabryla *et al.*, 2018; Barrios *et al.*, 2020).

Table 4.3: Antibacterial performance of PVDF (M1) and CNC/AgNP-modified PVDF (M4) against bacterial strains.

Strains	Bacterial concentration before and after membrane modification (CFU mL^{-1})				
	E. coli	*P. aeruginosa*	*S. aureus*	*S. epidermis*	*S. saprophyticus*
Control	4.10×10^7	9.55×10^7	4.80×10^7	8.90×10^7	9.05×10^7
M1	4.05×10^7	9.48×10^7	4.69×10^7	8.83×10^7	8.99×10^7
M4	5.00×10^5	4.55×10^7	1.05×10^7	4.10×10^7	6.00×10^6

4.4 Conclusion

CNC-capped AgNPs were successfully synthesized via a microwave-assisted approach. The bio-derived approach was preferred to ensure a sustainable green synthesis of the AgNPs. Minimal particle agglomeration and a heterogenous dispersion of AgNPs was confirmed from TEM analysis, markedly exhibiting an average diameter of 13.3 ± 4 nm. Preliminary evaluation of the anti-bacterial activity of the CNC-capped AgNPs and CNC/AgNP-modified PVDF membrane was conducted using five different bacterial strains, both showing excellent antibacterial activity against all strains. Overall, the application of CNC-capped AgNPs demonstrated effectiveness towards bacterial cells' growth control.

4.5 References

1. Badawy, A. A. *et al.* (2021) 'Utilization and characterization of cellulose nanocrystals decorated with silver and zinc oxide nanoparticles for removal of lead ion from wastewater', *Environmental Nanotechnology, Monitoring and Management*, 16, p. 100501. doi: 10.1016/j.enmm.2021.100501.
2. Barrios, A. C. *et al.* (2020) 'Prolonging the antibacterial activity of nanosilver-coated membranes through partial sulfidation', *Environmental Science: Nano*, 7(9), pp. 2607–2617. doi: 10.1039/d0en00300j.
3. Bogler, A., Lin, S. and Bar-Zeev, E. (2017) 'Biofouling of membrane distillation, forward osmosis and pressure retarded osmosis: Principles, impacts and future directions', *Journal of Membrane Science*, 542, pp. 378–398. doi: 10.1016/j.memsci.2017.08.001.
4. Chen, J. *et al.* (2008) 'Microwave-assisted green synthesis of silver nanoparticles by carboxymethyl cellulose sodium and silver nitrate', *Materials Chemistry and Phyisics*, 108, pp. 421–424. doi: 10.1016/j.matchemphys.2007.10.019.
5. Cieśla, J. *et al.* (2020). 'Effect of different conditions of synthesis on properties of silver nanoparticles stabilized by nanocellulose from carrot pomace', *Carbohydrate Polymers*, *245*. https://doi.org/10.1016/j.carbpol.2020.116513

6. Hanif, Z. *et al.* (2021) ‘One-pot synthesis of silver nanoparticle deposited cellulose nanocrystals with high colloidal stability for bacterial contaminated water purification’, *Journal of Environmental Chemical Engineering*, 9(4), pp. 105535. doi: 10.1016/j.jece.2021.105535.
7. Hoeng, F. *et al.* (2015) ‘Charge density modification of carboxylated cellulose nanocrystals for stable silver nanoparticles suspension preparation’, *Journal of Nanoparticle Research*, 17(6), pp. 1–14. doi: 10.1007/s11051-015-3044-z.
8. Hori, K. and Matsumoto, S. (2010) ‘Bacterial adhesion: From mechanism to control’, *Biochemical Engineering Journal*, 48(3), pp. 424–434. doi: 10.1016/j.bej.2009.11.014.
9. Jatoi, A. W. *et al.* (2019) ‘Dopa-based facile procedure to synthesize AgNP/cellulose nanofiber composite for antibacterial applications’, *Applied Nanoscience (Switzerland)*, 9(8), pp. 1661–1670. doi: 10.1007/s13204-019-00952-3.
10. Kamiloglu, S. *et al.* (2020) ‘Guidelines for cell viability assays’, *Food Frontiers*, 1(3), pp. 332–349. doi: 10.1002/fft2.44.
11. Liu, H. *et al.* (2012) ‘Cellulose nanocrystal/silver nanoparticle composites as bifunctional nanofillers within waterborne polyurethane’, *ACS Applied Materials and Interfaces*, 4(5), pp. 2413–2419. doi: 10.1021/am3000209.
12. Lizundia, E. *et al.* (2018) ‘Metal Nanoparticles Embedded in Cellulose Nanocrystal Based Films: Material Properties and Post-use Analysis’, *Biomacromolecules*, 19(7), pp. 2618–2628. doi: 10.1021/acs.biomac.8b00243.
13. Lokanathan, A. R. *et al.* (2014) ‘Cellulose nanocrystal-mediated synthesis of silver nanoparticles: Role of sulfate groups in nucleation phenomena’, *Biomacromolecules*, 15(1), pp. 373–379. doi: 10.1021/bm401613h.
14. Lulamba, T. E., Green, E. and Serepa-Dlamini, M. H. (2021) ‘Photorhabdus sp. ETL antimicrobial properties and characterization of its secondary metabolites by gas chromatography–mass spectrometry’, *Life*, 11(8). doi: 10.3390/life11080787.
15. Ma, Z. *et al.* (2021) ‘In-situ synthesis and immobilization of silver nanoparticles on microfibrillated cellulose for long-term antibacterial applications’, *Cellulose*, 28(10), pp. 6287–6303. doi: 10.1007/s10570-021-03941-4.

16. Nthunya, L. N. *et al.* (2017) ‘Greener Approach to Prepare Electrospun Antibacterial β-Cyclodextrin/Cellulose Acetate Nanofibers for Removal of Bacteria from Water’, *ACS Sustainable Chemistry and Engineering*, 5(1), pp. 153–160. doi: 10.1021/acssuschemeng.6b01089.
17. Nthunya, L. N. *et al.* (2020) ‘F-MWCNTs/AgNPs-coated superhydrophobic PVDF nanofibre membrane for organic, colloidal, and biofouling mitigation in direct contact membrane distillation’, *Journal of Environmental Chemical Engineering*, 8(2), pp. 103654. doi: 10.1016/j.jece.2020.103654.
18. Panchal, P., Ogunsona, E. and Mekonnen, T. (2019) ‘Trends in advanced functional material applications of nanocellulose’, *Processes*, 7(1). doi: 10.3390/pr7010010.
19. Stabryla, L. M. *et al.* (2018) ‘Emerging investigator series: It’s not all about the ion: Support for particle-specific contributions to silver nanoparticle antimicrobial activity’, *Environmental Science: Nano*, 5(9), pp. 2047–2068. doi: 10.1039/c8en00429c.
20. Stinson-Bagby, K. L. *et al*. (2019). 'Silver Nanoparticle Pulsed Synthesis and Attachment to Cellulose Nanocrystals', *ACS Applied Nano Materials*, *2*(4), pp, 2317–2324. https://doi.org/10.1021/acsanm.9b00225
21. Sunitha, A. *et al.* (2013) ‘Evaluation of Antimicrobial Activity of Biosynthesized Iron and Silver Nanoparticles Using the Fungi Fusarium and Actinomycets sp. on Human Pathogen’, *Nano Biomed Eng*, 5(1), pp. 39–45. doi: 10.5101/nbe.v5i1.p39-45.Magnetic.
22. Toro, R. G. *et al.* (2021) ‘Evaluation of long–lasting antibacterial properties and cytotoxic behavior of functionalized silver-nanocellulose composite’, *Materials*, 14(15). doi: 10.3390/ma14154198.
23. Trache, D. *et al.* (2020) *Nanocellulose: From Fundamentals to Advanced Applications*, *Frontiers in Chemistry*. doi: 10.3389/fchem.2020.00392.
24. Wang, Wenyi *et al.* (2019) ‘Palygorskite/silver nanoparticles incorporated polyamide thin film nanocomposite membranes with enhanced water permeating, antifouling and antimicrobial performance’, *Chemosphere*, 236, p. 124396. doi:

10.1016/j.chemosphere.2019.124396.

25. Wang, Z. *et al.* (2009) ‘Facile fabrication method and characterization of hollow Ag/SiO2 double-shelled spheres’, *Langmuir*, 25(13), pp. 7646–7651. doi: 10.1021/la9002934.
26. Xiong, R. *et al.* (2013) ‘Facile synthesis of tunable silver nanostructures for antibacterial application using cellulose nanocrystals’, *Carbohydrate Polymers*, 95(1), pp. 214–219. doi: 10.1016/j.carbpol.2013.02.077.
27. Xu, Q. *et al.* (2019) ‘Synthesis of silver nanoparticles using dialdehyde cellulose nanocrystal as a multi-functional agent and application to antibacterial paper’, *Cellulose*, 26(2), pp. 1309–1321. doi: 10.1007/s10570-018-2118-3.
28. Yu, H. Y. *et al.* (2014) ‘One-pot green fabrication and antibacterial activity of thermally stable corn-like CNC/Ag nanocomposites’, *Journal of Nanoparticle Research*, 16(1), pp. 1–12. doi: 10.1007/s11051-013-2202-4.
29. Zhu, J. *et al.* (2021) ‘Cellulose nanocrystal assisted trace silver nitrate to synthesize green silver nanocomposites with antibacterial activity’, *RSC Advances*, 11(7), pp. 3808–3815. doi: 10.1039/d0ra07198f.

Chapter 5: Preparation of nanoparticle enhanced PVDF for improved performance in membrane distillation

5.1 Introduction

Although MD continues to be evaluated on laboratory scale for water desalination and treatment of wastewater (Lalia *et al.*, 2014; Huang *et al.*, 2021; Makanjuola, Anis and Hashaikeh, 2021; Rabie, Elkady and El-Shazly, 2021), extensive studies are still required to optimize membrane properties and operating conditions. It is worthwhile to note that pilot scale testing is actively underway in various research institutions (Tijing *et al.*, 2015). A company called Aquaver commissioned MD pilot plants in the Maldives (Drioli, Ali and Macedonio, 2015). As mentioned prior, MD utilizes a hydrophobic membrane during separation. PVDF is a hydrophobic membrane predominantly used in MD and possesses excellent hydrophobicity (which can be improved), thermal stability, mechanical strength and resistance to aggressive chemicals (Ji *et al.*, 2021). It comprises multiple -CF_2-CH_2- units (Abdalla, Obaid and Al-Marzouki, 2016) and dissolves in a wide variety of solvents, dissimilar to PP and PTFE whose preparation introduces solvent choice intricacies and complex processing methods (Bottino, Capannelli and Comite, 2005). The hydrophobicity of PVDF is desired as it facilitates minimal membrane wetting (Tan *et al.*, 2020). Unique to MD, irreversible wetting has been reported to cause a rise in costs through increasing membrane replacements (Ruiz-Aguirre, Andrés-Mañas and Zaragoza, 2019).

Although highly attractive, PVDF still lacks superior properties required for MD application. Membranes possessing inadequate properties lead to increases in operational costs and induce significant efficiency losses. To improve membrane properties, membranes are usually modified using various NPs (Nejati *et al.*, 2015). This ensures: (1) membrane properties' enhancement and/or (2) fouling control measures. CNTs are NPs commonly used during membrane synthesis, largely due to their specific hollow structure and high durability (Zhou *et al.*, 2019). The durability of CNTs stems from their high tensile strength (Gao *et al.*, 2020). During membrane synthesis, CNTs often agglomerate, presenting significant challenges of low even percolation within the membrane matrix (Kar *et al.*, 2018). This produces membranes of inadequate properties

(Biswas, Kar and Bose, 2015). Hence, functionalization of CNTs with fluorinated silanes is a common approach to enhance their dispersion within the PVDF matrix." In this chapter, the impact of the incorporation of *f*-CNTs, PVP and CNC-capped AgNPs during PVDF membrane synthesis to enhance its overall membrane performance was assessed. The performance of the modified membranes was further assessed in DCMD using artificial seawater as the feed stream. Lastly, leaching tests of AgNPs on the membrane surface were conducted to evaluate the extent of the leachability of the AgNPs.

5.2 Materials and methods

5.2.1 Materials

PVDF (powder, Mw = 534 000 g/mol), polyvinylpyrrolidone (PVP, powder, Mw = 360 000 g/mol), dimethylformamide (DMF, ACS reagent, 99%), dimethylacetamide (DMac, ACS reagent, 99%), 1-propanol (ACS reagent, 99%), sodium chloride (NaCl, Mw = 58.44 g/mol), magnesium chloride ($MgCl_2$, Mw = 95.21 g/mol), sodium sulphate ($NaSO_4$, Mw = 142.04 g/mol), calcium chloride ($CaCl_2$, Mw = 110.99 g/mol), potassium chloride (KCl, Mw = 74.56 g/mol), 1H, 1H, 2H, 2H-perfluoro-octyltriethoxysilane (POTS, ACS reagent, 98%), toluene (ACS reagent, 99%), and nitric acid (HNO_3, ACS reagent, 99%) were procured from Sigma Aldrich (Germany). Liquid nitrogen was procured from Schorn Cryogenics (South Africa). The CNCs were procured from Nanografi Nano Technology and CNTs from SabiNano (Pty) Ltd.

5.2.2 Methods

a) Preparation of *f*-CNTs

f-CNTs were synthesized following a modified approach (Gao *et al.*, 2020). Briefly, 80 mL HNO_3 was mixed with 0.5 g CNTs under sonication for 4 h at room temperature, followed by a temperature increase to 60 ºC for 24 h. This was done to allow carboxyl groups to

form on the surface of CNTs for further modification. Following acidification, CNTs were centrifuged at 4000 revolutions per minute (rpm) for 20 min and rinsed with DI water to ensure complete removal of residual acid. The CNTs were later dried at 60 ºC overnight. Fluorosilanization of modified CNTs (**Figure 5.1**) involved the dissolution of 0.5 g acidified CNTs in toluene under sonication for 2 h. Then, 20 mL of 0.5 wt% of the POTS toluene solution (prepared by dissolving 0.5 g of POTS in 100 mL toluene) was added into the CNTs mixture and the resultant solution stirred for 24 h. The product produced (*f*-CNTs herein) was washed with toluene and dried at 60 ºC overnight.

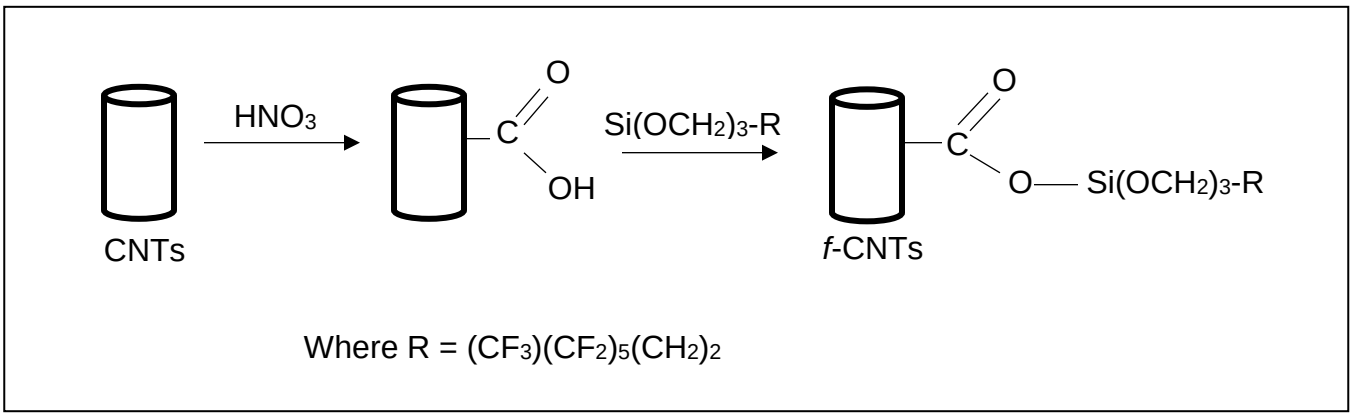

Figure 5.1: Interaction between CNTs and POTS to produce *f*-CNTs

b) Preparation of PVDF membranes

The method of pristine and modified PVDF membranes' preparation is similar to the one described in **Chapter 4**.

c) Characterization of CNTs and *f*-CNTS

CNTs and f-CNTS were characterized using TEM for morphological analysis, XRD for the study of crystalline phases, FTIR for the analysis of functional groups and EDS for elemental analysis.

d) Characterization of PVDF membranes

The membranes were characterized to understand their physicochemical properties using various techniques. Dead-end filtration was used to determine the LEP for each membrane. Scanning electron microscopy (SEM) analysis was conducted using TESCAN Vega SEM to understand the morphological properties of the membranes.

To study membrane cross-section using SEM, each membrane sample was dipped into liquid nitrogen for about 5 mins and freeze fractured. Prior to SEM analysis, all samples were sputter coated using gold/palladium (Au/Pd) to minimize sample charging. AFM (Witec Alpha 300 A, TS-150) analysis was conducted to understand the extent of membrane roughness using a scanning area of 2.0 μm × 2.0 μm. FTIR (Tensor 27 FTIR, Bruker South Africa (PTY) LTD) was used to evaluate the functional groups for each membrane (modified and unmodified) at a scanning range of 500 cm^{-1} to 4000 cm^{-1}. Membrane-water contact angle measurements were assessed using a goniometer via the sessile drop method.

Membrane porosity was determined gravimetrically. Experimentally, a membrane sample (2 × 2 cm^2) was submerged in 1-propanol for 24 h, with the masses of the saturated and the dry membrane measured, and the porosity calculated using the equation below:

$$\varepsilon = \frac{(m1-m2)/De}{(m1-m2)/De + m2/Dp} \times 100, \quad (1)$$

where ε is the membrane porosity (%), m1 and m2 are the masses of the saturated membrane (g) and dry membrane (g) respectively, De and Dp the specific gravities of 1-propanol (g/cm^3) and PVDF (g/cm^3), respectively.

e) Leaching studies of AgNPs

A modified method was used to quantify the amount of AgNPs released from CNC/AgNP-modified PVDF membrane (M4) (Xuan *et al.*, 2020). Briefly, samples of the membrane were cut into rectangles (1 × 3 cm), placed in 15 mL DI water, and shaken at 140 rpm for 72 h. Aliquot samples of 3 mL were taken at different time intervals (1, 3, 6, 9, 12, 24, 48 and 72 h), with equal supplementation of fresh DI water. The collected aliquots were analyzed for silver using ICP-OES.

f) Membrane performance evaluation using DCMD

Lab-scale DCMD tests were conducted to evaluate membrane performance (**Figure 5.2**), where each membrane was placed in direct contact with the feed stream and the distillate stream (inside the module). The active surface area for each membrane tested was 1.147 m^2. Artificial seawater (the feed stream) was composed of 24.5 g/L NaCl, 5.2 g/L $MgCl_2$, 4.1 g/L $NaSO_4$, 1.1 g/L $CaCl_2$, and 0.69 g/L KCl. Distilled water (approx. conductivity of 0.691 µS/cm) was used as the distillate stream. The plate and frame module was applied during operation. The solutions were circulated in a counter-current direction at a crossflow velocity of 7 mL/sec using a peristaltic pump (Cole Parmer Ltd, Masterflex). The temperatures of the feed and distillate solutions were set at 60 ºC and 15 ºC, respectively. A water bath and chiller were used to maintain the feed and distillate solution temperatures, respectively. Salt rejection efficiency was measured using a conductivity meter and the water flux measured using a weighing balance, and the calculations done using the following equations:

$$R\% = \frac{k_f - k_p}{k_f} * 100\% \quad (2)$$

$$J = {}^{m}/_{A \times t}, \quad (3)$$

where *R%, k_f, k_p J, m, A,* and *t* represent the salt rejection efficiency (%), feed conductivity (µS/cm), distillate conductivity (µS/cm), water flux (kg/m^2/h), distillate mass obtained from the weighing balance (kg), effective membrane area (m^2) and time (h), respectively.

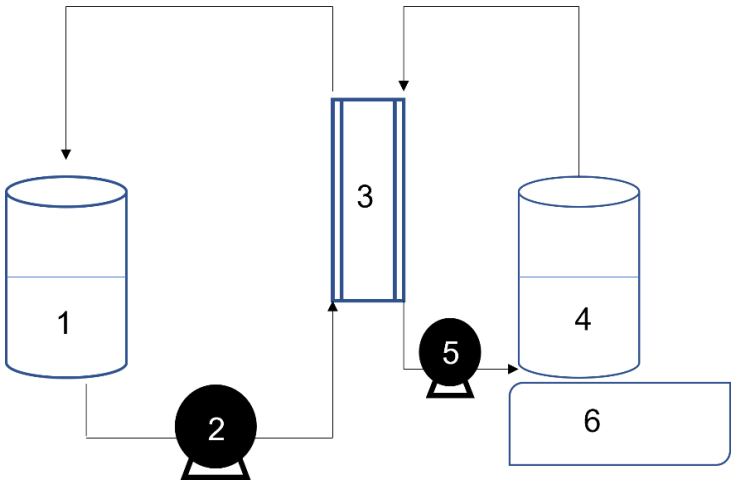

Figure 5.2: MD lab-set up: (1) Feed tank, (2) and (5) Circulation pumps, (3) Membrane module, (4) Distillate tank, and (6) Weighing balance

5.3 Results and discussion

5.3.1 Characterization of CNTs and *f*-CNTs

a) TEM, FTIR and XRD analysis of CNTs and *f*-CNTs

The transmission electron micrograph of CNTs and *f*-CNTs is presented in **Figure 5.3**. Entangled-like structures were observed for both CNTs and *f*-CNTs, with interconnected tubing. It is envisaged that the nanotubes were held in bundles by strong intermolecular forces (i.e., Van Der Waals forces) (Aqel *et al.*, 2012). From **Figure 5.3b**, it is evident that functionalization with POTS was achieved successfully, depicted by the ends of the *f*-CNTs increasing in thickness (Demirel and Dadashov, 2022). FTIR analysis was further conducted to study various functional groups present within the samples. Absorption peaks occurring at 1486 cm^{-1}, 1585 cm^{-1}, 2099 cm^{-1} and 2334 cm^{-1} were attributed to C-H, C=C, COOH, and C-O stretching bands, respectively. A shift in FTIR spectra (red shift) was observed upon CNTs reaction with POTS, a phenomenon depicting chemical structural changes occurring during functionalization. XRD analysis was conducted to

study the crystal phases and chemical composition of CNTs and *f*-CNTs (**Figure 5.4**). For CNTs, the crystal planes of (002) and (100) at 25.0º and 42.0º were attributed to the graphite pattern of carbon (Cui *et al.*, 2014). Upon functionalization with POTS, an additional silica peak emerged at 18.5°.

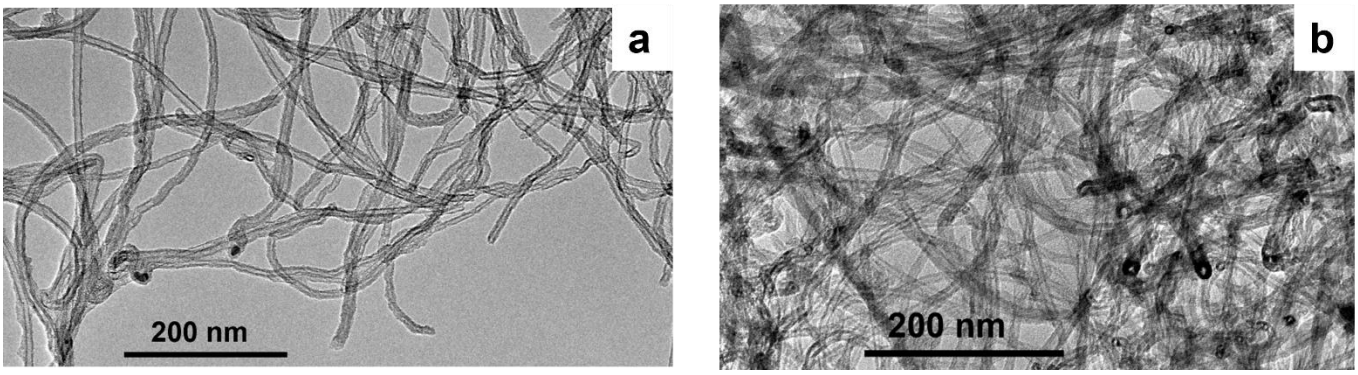

Figure 5.3: TEM images of (a) CNTs and (b) *f*-CNTs

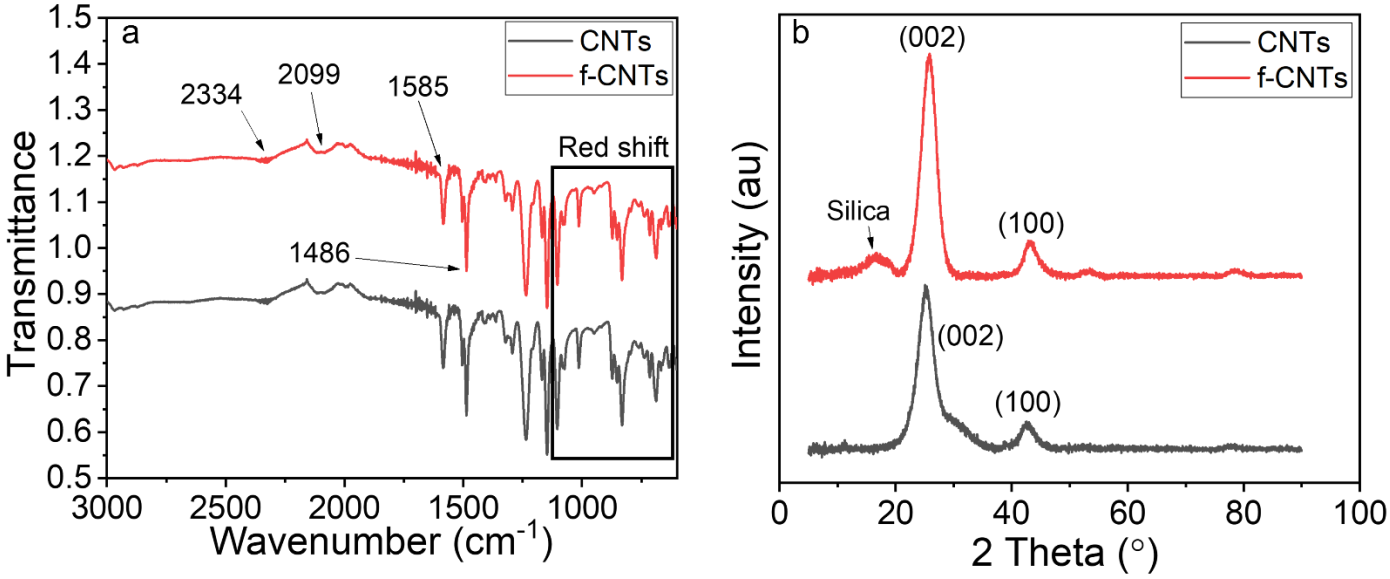

Figure 5.4: FTIR plot (a) and XRD plot (b) of CNTs and *f*-CNTs

b) EDS analysis of CNTs and *f*-CNTs

The elemental composition of CNTs and *f*-CNTs was studied using EDS (**Figure 5.5**). On both spectra, the presence of gold (Au) was attributed to Au/Pd, a chemical used to coat the samples prior to EDS analysis. This was done to minimize the charging of samples. For CNTs, the most predominant element was carbon, as CNTs are primarily composed of allotropic forms of carbon (Tiwari *et al.*, 2016). Upon functionalization with POTS, new peaks emerged, particularly for silicon, fluorine, and oxygen, confirming successful grafting.

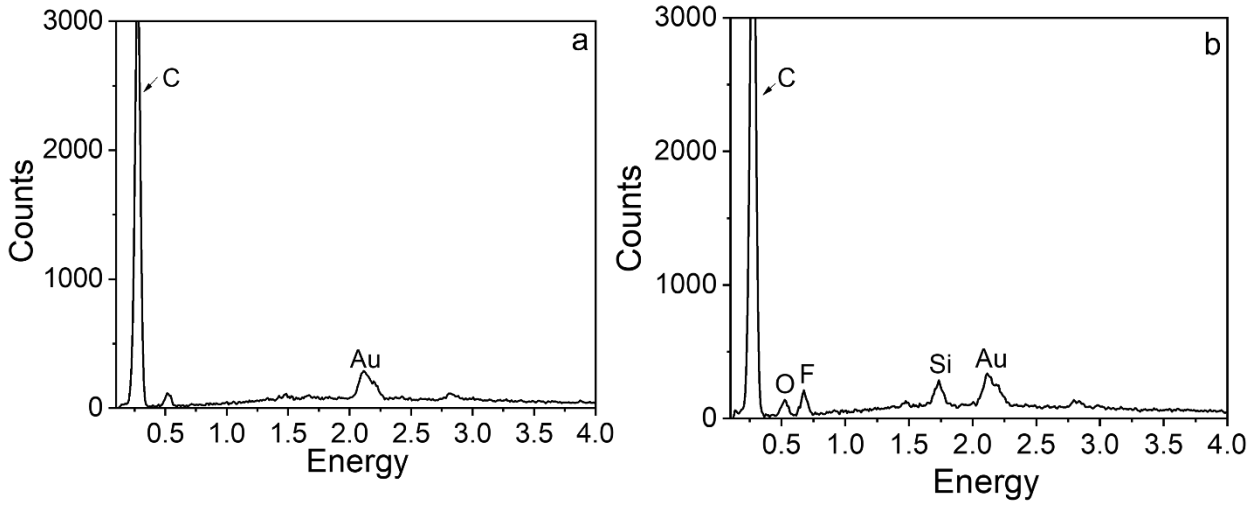

Figure 5.5: EDS Spectra of CNTs (a) and *f*-CNTs (b)

5.3.2 Physiochemical properties of PVDF membranes

a) Chemical composition of PVDF membranes

FTIR analysis of the as-synthesized membranes was conducted to understand their chemical composition. The individual membranes exhibited peaks of similar position (**Figure 5.6**), with the C-C stretching peak displayed at 1078 cm^{-1}, the intense C-F stretching peak at 1174 cm^{-1}, and the C-H wagging and stretching vibration at 1401 cm^{-1} (Tan *et al.*, 2020; Lu *et al.*, 2021). Indeed, the fingerprint region of PVDF has been

reported to be between 600 – 1500 cm^{-1} (Teoh *et al.*, 2021). The weak stretch at 1676 cm^{-1} caused by the presence of C=O for M2, M3 and M4 confirmed the presence of PVP within the modified membranes. CNC/AgNP-modified PVDF membrane displayed the α and β phases of PVDF at 838 cm^{-1} and 871 cm^{-1}, respectively, with the β phase existing in the highest intensity. This was attributed to AgNPs' interaction with the membrane (Issa *et al.*, 2017).

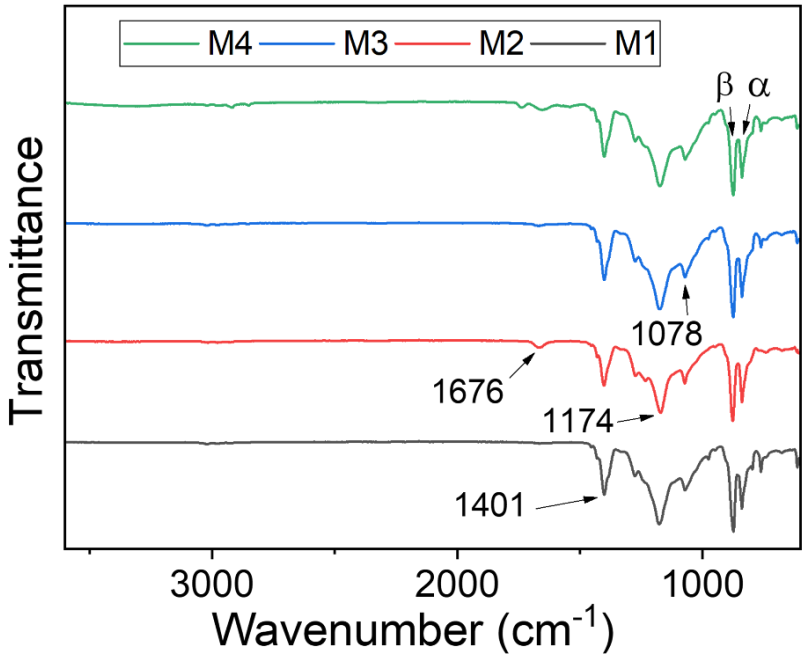

Figure 5.6: FTIR spectra of the as-synthesised membranes

b) Morphological properties of PVDF membranes

The SEM micrographs of the PVDF membranes illustrating their morphological properties is presented in **Figure 5.7**. The top surfaces of all membranes appeared sponge-like, with highly compact surfaces. The sponge-like structure is necessary as it contributes towards the mechanical strength of the membrane (Lai *et al.*, 2014). No evidence of membrane deformation was observed. Incorporation of CNC-capped AgNPs on PVDF resulted in minimal particle agglomeration (**Figure 5.7 – M4**). This is desirable as agglomeration reduces the activity of the NPs. Since all membrane surfaces appeared dense, structural variations were assessed using cross-sectional images and AFM.

Based on the cross-sectional images, the membranes were asymmetric and exhibited heterogenous structures containing distinct macro-voids of different shapes and sizes. Although the addition of PVP induced the formation of finger-like macropores (M2) due to its hydrophilicity, addition of *f*-CNTs lowered the size and number of these structures (M3). This was envisaged to be due to a rise in the viscosity of the polymer solution and a subsequent decrease in the solvent/non-solvent exchange rate during phase inversion (Nejati *et al.*, 2015). Water was used as the coagulating agent during synthesis because of its ability to rapidly facilitate the solvent/non-solvent exchange rate (Teoh *et al.*, 2021). Further addition of CNC-capped AgNPs increased pore elongation, especially for the top layer of the membrane, due to the hydrophilicity of the NPs (Xu *et al.*, 2020). Asymmetric structures of membranes generally translate to enhanced permeability (Wu *et al.*, 2015).

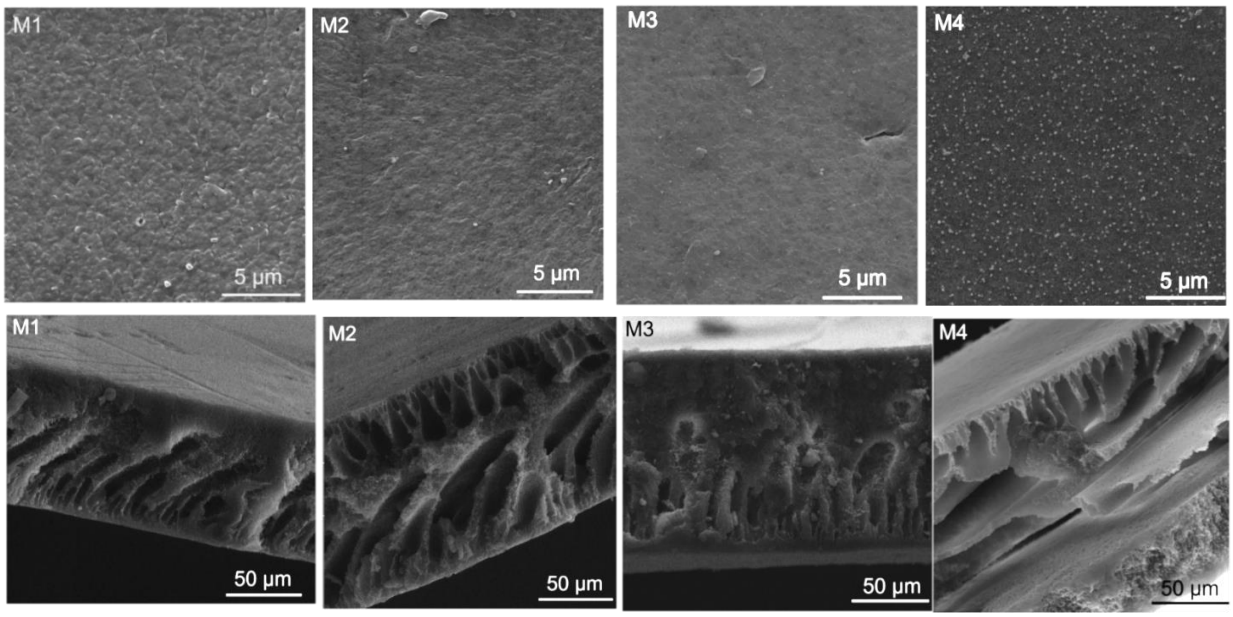

Figure 5.7: SEM micrographs of PVDF membranes: Top surface and corresponding cross-sectional morphology

c) Physical properties of PVDF membranes

Functionalization of PVDF with *f*-CNTs and CNC-capped AgNPs improved membranes' resistance to wetting as seen from **Table 5.2** below, where the LEP of M2 increased from 280 kPa ± 3 to 340 kPa ± 6 (M3) and 330 kPa ± 1 (M4). According to Chiu et al (2021), the addition of *f*-CNTs increases the viscosity of the PVDF polymer solution, leading to a decreased exchange rate of the solvent (DMac/DMF 3:2 v/v ratio) and non-solvent (water) during phase inversion (Chiu *et al.*, 2021). Herein, a decreased exchange rate resulted in an increase in LEP as stated prior and an overall decline in membrane porosity and pore size, especially for M3 (**Table 5.2**). A high LEP in MD is desired as it leads to high salt rejection efficiency. Nanofillers such as *f*-CNTs reduce the membrane pores and porosity by filling the macro-voids, increasing the LEP (Zhou *et al.*, 2019). The decrease in LEP and contact angle from M1 to M2 was attributed to the addition of PVP, largely due to its high polarity (Rawat *et al.*, 2014). This was simultaneously proven by an increase in membrane pore size (M2 – 0.21 µm) (Tofighy, Mohammadi and Sadeghi, 2021). It is worth noting that the overall porosity was inversely proportional to LEP, a relation directly confirmed by Ardeshiri *et al.,* (2018).

Table 5.2: Physical properties of the PVDF membranes

	Overall porosity (%)	LEP (kPa)	Overall Thickness (µm)	Mean pore size (µm)
M1	72.6 ± 0.84	310 ± 7	86	0.17
M2	84.3 ± 1.15	280 ± 3	112	0.21
M3	71.1 ± 2.99	340 ± 6	124	0.10
M4	70.4 ± 1.09	330 ± 1	135	0.10

d) Membrane-solvent water contact angle (WCA) of PVDF membranes

The degree of membrane hydrophobicity was determined using WCA measurements, where the interaction of water with the membrane surface was measured. Results are plotted in **Figure 5.8**, below. The WCA of pristine PVDF membrane was 91.1º ± 0.80. Similar results were reported by Isya *et al.,* (2020). It is the fluorinated carbons of PVDF that afford the desirable contact angle of >90º, lessening the surface energy and increasing propensity for MD application (Sinha Ray, Dangayach and Kwon, 2021). Modification of pristine PVDF (M1) with PVP caused a decrease in the water contact angle (from 91.1º ± 0.80 to 82.6º ± 0.95) due to PVP's inherent hydrophilicity and pore-forming capability. Upon the addition of *f*-CNTs and CNC-capped AgNPs, the WCA increased to 92.9º ± 0.35, implying enhanced hydrophobicity. This was attributed to the hydrophobic nature of the *f*-CNTs, and the increased surface roughness as confirmed by AFM results (**Figure 5.9**). The direct correlation between hydrophobicity and surface roughness was noted elsewhere (Zheng *et al.*, 2016).

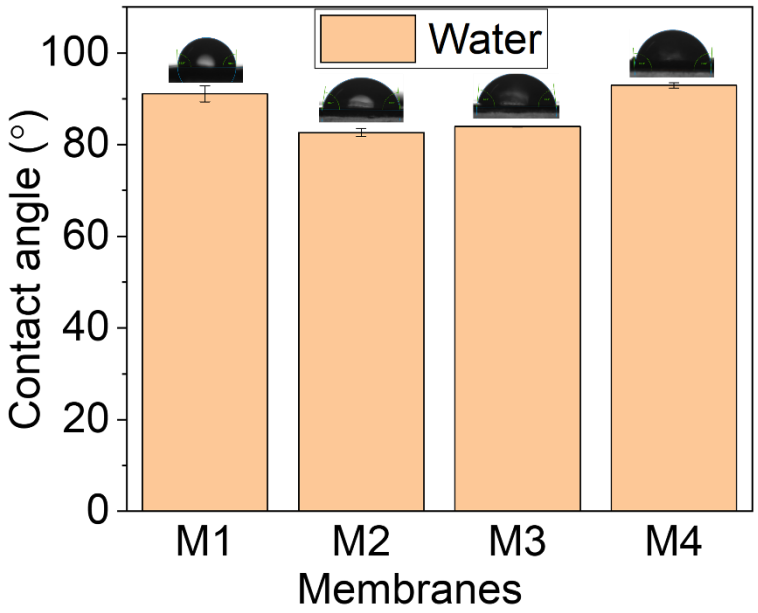

Figure 5.8: Contact angle measurements of the as-synthesized membranes

e) Roughness characteristics of PVDF membranes

AFM analysis was conducted to evaluate membrane surface roughness. The AFM micrographs are presented in **Figure 5.9** and display bright regions (signifying peaks) and dark regions (signifying valleys). According to the Cassie Baxter phenomenon, it is the dark valleys that house air-pockets that promote increased surface hydrophobicity through decreasing membrane contact with water (Teoh *et al.*, 2021). The extent of membrane surface roughness is usually measured through assessing the average surface roughness (Ra) and root mean square roughness (Rq), which are presented in **Figure 5.9**. It is evident that average surface roughness decreased from M1 (15.95 nm) to M2 (13.37 nm) due to PVP addition, which facilitated the formation of a smooth layer. However, average surface roughness increased drastically upon addition of *f*-CNTs and CNC-capped AgNPs to 68.43 nm (M4). This was attributed to the adherence of the NPs to the network of the polymer. These changes in membrane roughness cohere with results obtained from contact angle measurements. In MD, rough membranes are desired as a rough membrane increases the turbulence of the feed solution and lowers the heat transfer resistance at the boundary layer, facilitating better vapor transport (Pagliero *et al.*, 2021).

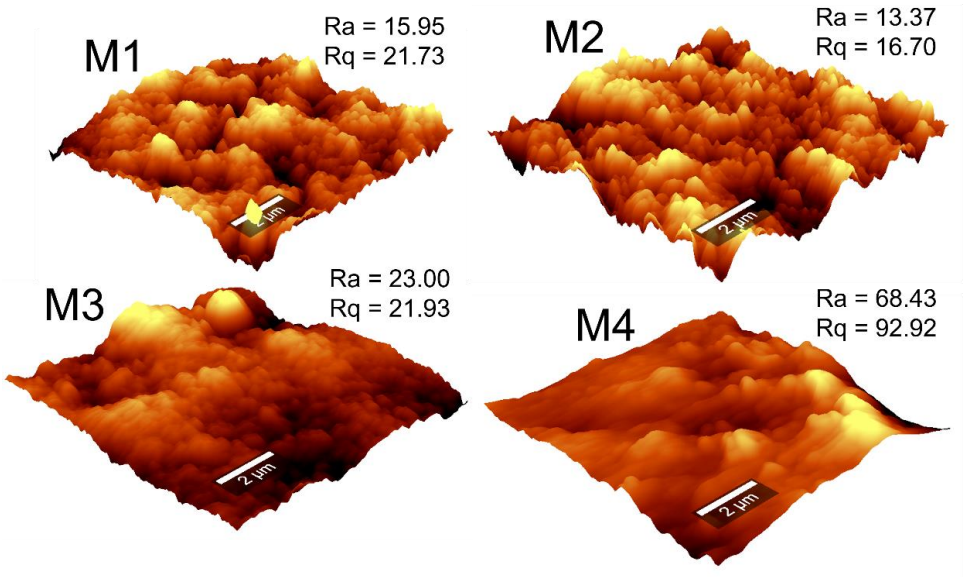

Figure 5.9: Surface roughness characteristics of the as-synthesised membranes

f) Mechanical properties of the PVDF membranes

Evaluation of membrane mechanical properties to determine their suitability in MD systems is key as membrane durability affects costs of operation (Lalia *et al.*, 2014). Herein, tensile strength (MPa), elongation stretch (%), and yield strength (MPa) were used to analyze the mechanical properties of the as-synthesised membranes (**Figure 5.10 and Table 5.3**). Based on the stress-strain plot, the mechanical strength for M1 (pristine PVDF) increased by 43% upon addition of PVP, *f*-CNTs and CNC-capped AgNPs (from 1.21 MPa to 2.13 MPa). This was due to their excellent dispersity within the PVDF matrix and higher affinity for PVDF (Nassrullah *et al.*, 2020; Tabhane and Giripunje, 2020). Excellent dispersity transfers the load from PVDF to the NPs, thus incurring higher strength (Dlamini, Mamba and Li, 2019). Owing to their high mechanical strength, *f*-CNTs and CNCs were eminent in increasing the tensile strength of the PVDF membranes (Grishkewich *et al.*, 2017).

Table 5.3: Mechanical properties of the PVDF membranes

Membranes	Ultimate tensile strength (MPa)	Young's modulus (MPa)	Elongation stretch (%)	Yield strength (MPa)
M1	1.477	0.2694	15.56	0.9576
M2	1.9121	0.4637	15.65	1.422
M3	1.7747	0.4606	5.95	1.578
M4	2.4740	1.0811	9.31	2.075

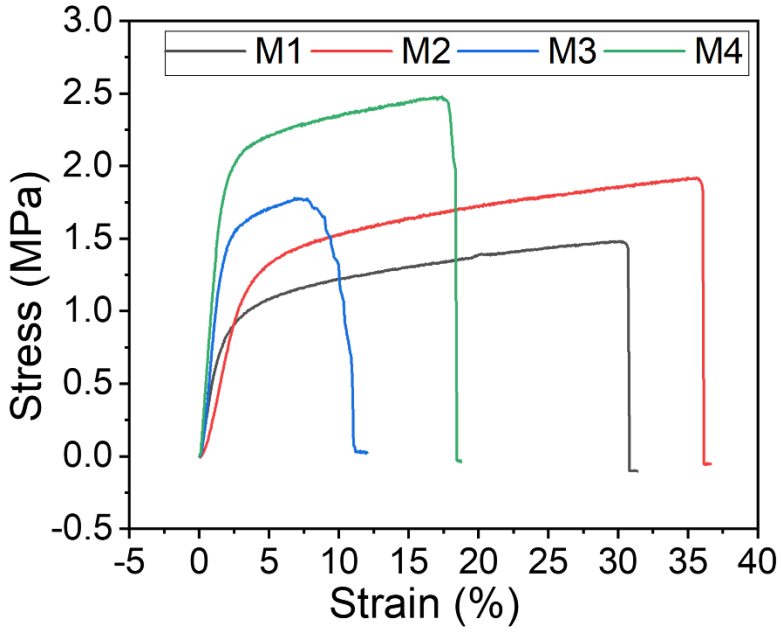

Figure 5.10: Stress-strain plot of the as-synthesised membranes

5.3.3 Leaching studies of AgNPs

To assess the stability of capped AgNPs on M4, leaching tests were evaluated using DI water. While silver release from the membrane is a requirement for the achievement of anti-microbial activity, excessive silver release may: (1) reduce the effectiveness of the membrane against bacteria within a short time, (2) contaminate the distillate stream, and (3) cause regular membrane replacements due to activity deterioration, further increasing operational expenditure (Barrios *et al.*, 2020). In addition, since silver has a certain level of toxicity, the study of its leachability is crucial for risk assessment purposes. The leaching of AgNPs from M4 was evaluated at various intervals for 72 h (**Figure 5.11).** A maximum of 0.378 ± 0.063 ppm leached out from the membrane over the period, with gradual slowing down at higher leaching times. This suggests sustained durability of silver release (Xuan *et al.*, 2020). The release of high concentrations of silver at the initial stages was induced by weakly bound AgNPs (Qi *et al.*, 2021). A minimal release of Ag^{+} ions from a polysulfone membrane was similarly reported by Maharubin *et al.*, (2018), noting a 0.918 ppm concentration in the distillate stream.

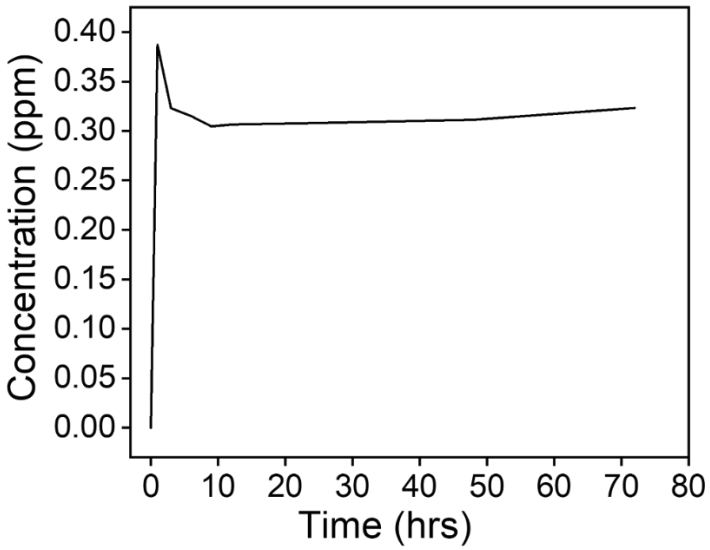

Figure 5.11: Concentration of silver released from CNC/AgNP-modified PVDF membrane (M4) following a 72-h leaching period.

5.3.4 Membrane performance evaluation using DCMD

The performance of the membranes (M1, M2, M3, M4) was evaluated in a DCMD lab-scale set-up where artificial seawater was used as the feed solution. Water flux and conductivity plots are presented in **Figure 5.12**. The average water flux for the pristine membrane (M1 - 0.528 ± 0.084 kg/m^2/hr) remained stable for a period of 24 h. However, distillate conductivity gradually increased without exceeding 85 µS/cm. This demonstrated excellent salt rejection efficiency, averaging 99.8%. M2 had the highest flux compared to the other membranes (0.603 ± 0.157 kg/m^2/hr), specifically due to high membrane porosity and low LEP (**Table 5.2**) caused by the presence of PVP. Similar to the water flux, conductivity was also high and increased to 166.2 µS/cm. The high conductivity implies that membrane wetting occurred and permitted the passage of salts through the membrane pores. It has been reported that when the conductivity of the distillate stream at any given point in time begins to be >20 µS/cm, membrane wetting is already commencing (Teoh *et al.*, 2021). Ahn *et al*., (2021) reported similar results, where analysis of PVDF performance in a DCMD set up yielded low salt rejection efficiency with

high water flux. Even though the conductivity of M2 over a period of 24 h averaged the highest, the separation efficiency was still excellent (99.6%), largely due to the inherent hydrophobicity of PVDF.

While M4 was characterized by high WCA and high LEP, the average water flux obtained was the lowest (0.179 ± 0.030 kg/m^2/hr). This was attributed to the blockage of pores induced by the presence of the CNC-capped AgNPs on the surface and the inner pores of the membrane. The nanoparticles contributed towards a decrease in the size of the walls of the pores and a subsequent increase in the mass transfer resistance of the vapor (Huang *et al*., 2021). However, the salt rejection efficiency of M4 was excellent (99.8%), with the conductivity over a period of 24 h only reaching a peak of 68.2 µS/cm. This was attributed to high contact angle (**Figure 5.8**) induced by increased surface roughness (**Figure 5.9**). The possibility of the formation of a hydration layer (induced by hydrophilic CNC-capped AgNPs) on the surface of M4 that could have prevented the passage of vapor was highly unlikely due to the high salt rejection efficiency of the membrane.

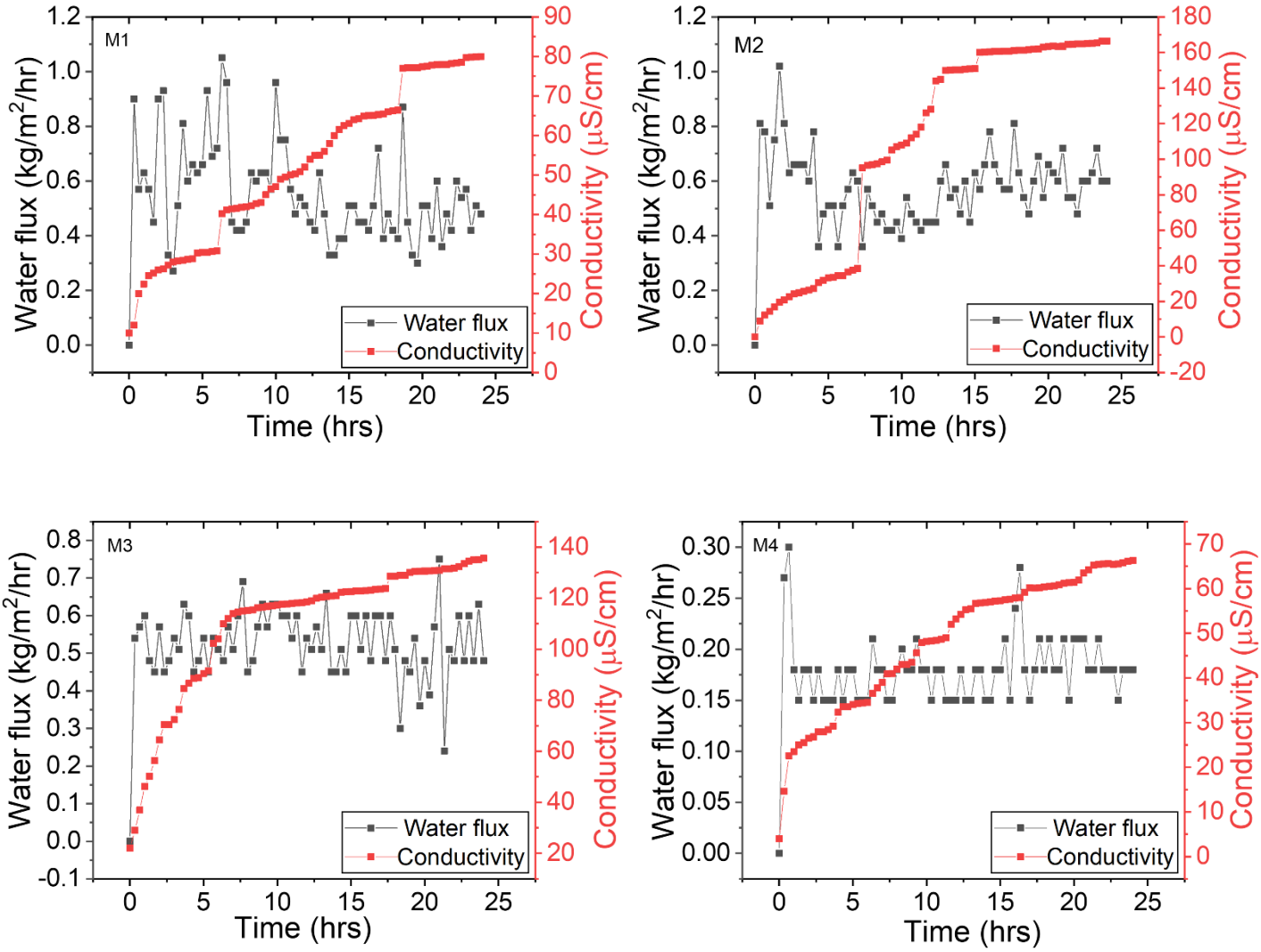

Figure 5.12: Water flux and distillate salinity results for M1, M2, M3 and M4 as obtained from DCMD operations where artificial seawater was used as the feed stream

5.4 Conclusion

In this work, PVDF was synthesized using the phase inversion technique and functionalized with *f*-CNTs, PVP and CNC-capped AgNPs for improvement of overall membrane properties. From the results, CNC/AgNP-modified PVDF membrane (M4) presented superior properties, displaying a 43.0% and a 75% increase in mechanical strength and surface roughness, respectively. This translates to a membrane possessing excellent properties for MD application. Although better membrane properties were

attained, the water flux of the CNC/AgNP-modified PVDF membrane remained low. This was attributed to the low rate of vaporization caused by the blockage of pores. Salt rejection efficiency, however, remained excellent, markedly at 99.8%. From the silver leaching tests, only less than 380 ppb of silver leached from the membrane, indicating good adherence of silver.

5.5 References

1. Abdalla, S., Obaid, A. and Al-Marzouki, F. M. (2016) 'Preparation and characterization of poly(vinylidene fluoride): A high dielectric performance nano-composite for electrical storage', *Results in Physics*, 6, pp. 617–626. doi: 10.1016/j.rinp.2016.09.003.
2. Ahn, M. *et al.* (2021) 'Analysis of polyvinylidene fluoride membranes fabricated for membrane distillation', *Membranes*, 11(6). doi: 10.3390/membranes11060437.
3. Alibakhshi, S. *et al.* (2019) 'Tuning morphology and transport in ultrafiltration membranes derived from polyethersulfone through exploration of dope formulation and characteristics', *Materials Research Express*, 6(12), pp. 1–14. doi: 10.1088/2053-1591/ab56c3.
4. Aqel, A. *et al.* (2012) 'Carbon nanotubes, science and technology part (I) structure, synthesis and characterisation', *Arabian Journal of Chemistry*, 5(1), pp. 1–23. doi: 10.1016/j.arabjc.2010.08.022.
5. Ardeshiri, F. *et al.* (2018) 'PVDF membrane assisted by modified hydrophobic ZnO nanoparticle for membrane distillation', *Asia-Pacific Journal of Chemical Engineering*, 13(3), pp. 1–12. doi: 10.1002/apj.2196.
6. Barrios, A. C. *et al.* (2020) 'Prolonging the antibacterial activity of nanosilver-coated membranes through partial sulfidation', *Environmental Science: Nano*, 7(9), pp. 2607–2617. doi: 10.1039/d0en00300j.
7. Biswas, S., Kar, G. P. and Bose, S. (2015) 'Attenuating microwave radiation by absorption through controlled nanoparticle localization in PC/PVDF blends', *Physical Chemistry Chemical Physics*, 17(41), pp. 27698–27712. doi: 10.1039/c5cp05189d.

8. Bottino, A., Capannelli, G. and Comite, A. (2005) ‘Novel porous poly (vinylidene fluoride) membranes for membrane distillation’, *Desalination*, 183(1–3), pp. 375–382. doi: 10.1016/j.desal.2005.03.040.
9. Chiu, F. C. *et al.* (2021) ‘Polycarbonate/poly(Vinylidene fluoride)-blend-based nanocomposites—effect of adding different carbon nanofillers/organoclay’, *Polymers*, 13(16), pp. 1–15. doi: 10.3390/polym13162626.
10. Cui, X. *et al.* (2014) ‘The encapsulation of CdS in carbon nanotubes for stable and efficient photocatalysis’, *Journal of Materials Chemistry A*, 2(48), pp. 20939–20946. doi: 10.1039/c4ta04549a.
11. Demirel, E. and Dadashov, S. (2022) ‘Fabrication of a novel PVDF based silica coated multi-walled carbon nanotube embedded membrane with improved filtration performance’, *Chemical Engineering Communications*, 209(8), pp. 1009–1034. doi: 10.1080/00986445.2021.1935253.
12. Dlamini, D. S., Mamba, B. B. and Li, J. (2019) ‘The role of nanoparticles in the performance of nano-enabled composite membranes – A critical scientific perspective’, *Science of the Total Environment*, 656, pp. 723–731. doi: 10.1016/j.scitotenv.2018.11.421.
13. Drioli, E., Ali, A. and Macedonio, F. (2015) ‘Membrane distillation: Recent developments and perspectives’, *Desalination*, 356, pp. 56–84. doi: 10.1016/j.desal.2014.10.028.
14. Gao, C. *et al.* (2020) ‘Superhydrophobic electrospun PVDF membranes with silanization and fluorosilanization co-functionalized CNTs for improved direct contact membrane distillation’, *Engineered Science*, 9, pp. 35–43. doi: 10.30919/es8d905.
15. Grishkewich, N. *et al.* (2017) ‘Recent advances in the application of cellulose nanocrystals’, *Current Opinion in Colloid and Interface Science*, 29, pp. 32–45. doi: 10.1016/j.cocis.2017.01.005.
16. Huang, Y. X. *et al.* (2021) ‘Liquid-like surface modification for effective anti-scaling membrane distillation with uncompromised flux’, *Journal of Membrane Science*, 637(July), p. 119673. doi: 10.1016/j.memsci.2021.119673.
17. Issa, A. *et al.* (2017) ‘Physico-Mechanical, Dielectric, and Piezoelectric Properties

of PVDF Electrospun Mats Containing Silver Nanoparticles', *C*, 3(4), p. 30. doi: 10.3390/c3040030.

18. Ji, J. *et al.* (2021) 'Hydrophobic poly(vinylidene fluoride) / siloxene nanofiltration membranes', *Journal of Membrane Science*, 635(February), p. 119447. doi: 10.1016/j.memsci.2021.119447.
19. Kar, E. *et al.* (2018) 'MWCNT@SiO2 Heterogeneous Nanofiller-Based Polymer Composites: A Single Key to the High-Performance Piezoelectric Nanogenerator and X-band Microwave Shield', *ACS Applied Nano Materials*, 1(8), pp. 4005–4018. doi: 10.1021/acsanm.8b00770.
20. Lai, C. Y. *et al.* (2014) 'Preparation and characterization of poly(vinylidene fluoride)/nanoclay nanocomposite flat sheet membranes for abrasion resistance', *Water Research*, 57, pp. 56–66. doi: 10.1016/j.watres.2014.03.005.
21. Lalia, B. S. *et al.* (2014) 'Nanocrystalline cellulose reinforced PVDF-HFP membranes for membrane distillation application', *Desalination*, 332(1), pp. 134–141. doi: 10.1016/j.desal.2013.10.030.
22. Liu, F. *et al.* (2011) 'Progress in the production and modification of PVDF membranes', *Journal of Membrane Science*, 375(1–2), pp. 1–27. doi: 10.1016/j.memsci.2011.03.014.
23. Lu, Y. *et al.* (2021) 'Hydrophilic modification of PVDF membranes by in situ synthesis of nano-Ag with nano-ZrO2', *Green Processing and Synthesis*, 10(1), pp. 538–546. doi: 10.1515/gps-2021-0050.
24. Maharubin, S., Zhou, Y. and Tan, G. Z. (2018) 'Development and Investigation on a Silver Nanoparticle-Incorporated Electrofiltration System for Biofouling Control', *IEEE Transactions on Nanotechnology*, 17(5), pp. 948–954. doi: 10.1109/TNANO.2018.2832210.
25. Makanjuola, O., Anis, S. F. and Hashaikeh, R. (2021) 'Enhancing DCMD vapor flux of PVDF-HFP membrane with hydrophilic silica fibers', *Separation and Purification Technology*, 263, p. 118361. doi: 10.1016/j.seppur.2021.118361.
26. Nassrullah, H. *et al.* (2020) 'Incorporation of nanosized LTL zeolites in dual-layered PVDF-HFP/cellulose membrane for enhanced membrane distillation performance', *Journal of Membrane Science*, 611(April), p. 118298. doi:

10.1016/j.memsci.2020.118298.

27. Nejati, S. *et al.* (2015) ‘Engineering flat sheet microporous PVDF films for membrane distillation’, *Journal of Membrane Science*, 492, pp. 355–363. doi: 10.1016/j.memsci.2015.05.033.
28. Nofitri Da Conceicao Isya, H., Valadares Marcal, I. and Aquino, R. R. (2020) ‘Fabrication and Characterization of PVDF with an Additive of Nanozeolite via Electrospinning and Non-solvent Induced Phase Separation (NIPS) Process’, *MATEC Web of Conferences*, 319, p. 10002. doi: 10.1051/matecconf/202031910002.
29. Pagliero, M. *et al.* (2021) ‘Effect of support on PVDF membranes for distillation process’, *Journal of Membrane Science*, 635, p. 119528. doi: 10.1016/j.memsci.2021.119528.
30. Qi, L. *et al.* (2021) ‘Polymeric membrane ion-selective electrodes with anti-biofouling properties by surface modification of silver nanoparticles’, *Sensors and Actuators, B: Chemical*, 328, p. 129014. doi: 10.1016/j.snb.2020.129014.
31. Rabie, M., Elkady, M. F. and El-Shazly, A. H. (2021) ‘Effect of channel height on the overall performance of direct contact membrane distillation’, *Applied Thermal Engineering*, 196, p. 117262. doi: 10.1016/j.applthermaleng.2021.117262.
32. Rawat, A. *et al.* (2014) ‘Study of electrical properties of polyvinylpyrrolidone/polyacrylamide blend thin films’, *Bulletin of Materials Science*, 37(2), pp. 273–279. doi: 10.1007/s12034-014-0639-4.
33. Ruiz-Aguirre, A., Andrés-Mañas, J. A. and Zaragoza, G. (2019) ‘Evaluation of permeate quality in pilot scale membrane distillation systems’, *Membranes*, 9(6), pp. 1–14. doi: 10.3390/membranes9060069.
34. Sinha Ray, S., Dangayach, R. and Kwon, Y. N. (2021) ‘Surface engineering for anti-wetting and antibacterial membrane for enhanced and fouling resistant membrane distillation performance’, *Chemical Engineering Journal*, 405(June 2020), p. 126702. doi: 10.1016/j.cej.2020.126702.
35. Tabhane, G. H. and Giripunje, S. M. (2020) ‘Robust flower-like ZnO assembled β-PVDF/BT hybrid nanocomposite: Excellent energy harvester’, *Polymer Testing*, 88(April), p. 106564. doi: 10.1016/j.polymertesting.2020.106564.

36. Tan, H. F. *et al.* (2020) ‘Membrane distillation crystallization using PVDF membrane incorporated with TiO2 nanoparticles and nanocellulose’, *Water Science and Technology: Water Supply*, 20(5), pp. 1629–1642. doi: 10.2166/ws.2020.068.
37. Teoh, G. H. *et al.* (2021) ‘Impacts of PVDF polymorphism and surface printing micro-roughness on superhydrophobic membrane to desalinate high saline water’, *Journal of Environmental Chemical Engineering*, 9(4), p. 105418. doi: 10.1016/j.jece.2021.105418.
38. Tijing, L. D. *et al.* (2015) ‘Fouling and its control in membrane distillation-A review’, *Journal of Membrane Science*, 475, pp. 215–244. doi: 10.1016/j.memsci.2014.09.042.
39. Tiwari, S. K. *et al.* (2016) ‘Magical Allotropes of Carbon: Prospects and Applications’, *Critical Reviews in Solid State and Materials Sciences*, 41(4), pp. 257–317. doi: 10.1080/10408436.2015.1127206.
40. Tofighy, M. A., Mohammadi, T. and Sadeghi, M. H. (2021) ‘High-flux PVDF/PVP nanocomposite ultrafiltration membrane incorporated with graphene oxide nanoribbones with improved antifouling properties’, *Journal of Applied Polymer Science*, 138(4), pp. 1–15. doi: 10.1002/app.49718.
41. Wu, T. *et al.* (2015) ‘Facile and low-cost approach towards a PVDF ultrafiltration membrane with enhanced hydrophilicity and antifouling performance via graphene oxide/water-bath coagulation’, *RSC Advances*, 5(11), pp. 7880–7889. doi: 10.1039/c4ra13476a.
42. Wu, X. *et al.* (2018) ‘Superhydrophobic PVDF membrane induced by hydrophobic SiO2 nanoparticles and its use for CO2 absorption’, *Separation and Purification Technology*, 190, pp. 108–116. doi: 10.1016/j.seppur.2017.07.076.
43. Xu, C. *et al.* (2020) ‘Cellulose nanocrystal/silver (CNC/Ag) thin-film nanocomposite nanofiltration membranes with multifunctional properties’, *Environmental Science: Nano*, 7(3), pp. 803–816. doi: 10.1039/c9en01367a.
44. Xuan, L. *et al.* (2020) ‘In situ synthesizing silver nanoparticels by bio-derived gallic acid to enhance antimicrobial performance of PVDF membrane’, *Separation and Purification Technology*, 251, p. 117381. doi: 10.1016/j.seppur.2020.117381.

45. Zheng, L. *et al.* (2016) ‘Preparation of PVDF-CTFE hydrophobic membranes for MD application: Effect of LiCl-based mixed additives’, *Journal of Membrane Science*, 506, pp. 71–85. doi: 10.1016/j.memsci.2016.01.044.
46. Zhou, R. *et al.* (2019) ‘Effects of multi-walled carbon nanotubes (MWCNTs) and integrated MWCNTs/SiO 2 nano-additives on PVDF polymeric membranes for vacuum membrane distillation’, *Separation and Purification Technology*, 217, pp. 154–163. doi: 10.1016/j.seppur.2019.02.013.

Chapter 6: Evaluation of biofouling control in membrane distillation against *G. Stearothermophilus*

6.1 Introduction

Temperature is a crucial parameter to consider when tackling fouling in MD. This is because feed solution heating is a significant part of the process, affecting performance dynamics. Although mesophilic bacteria induce biofouling to an extent, thermophilic bacteria significantly exacerbate it, since they have a better propensity to thrive under MD feed operating temperatures (40 ºC – 80 ºC) (Zodrow *et al.*, 2014). The challenges associated with thermophiles include microbial community succession following exposure to heat, inducing irreversible biofilm formation and increased EPS secretion (Costa *et al.*, 2021). In addition, thermophiles auto-regulate their metabolic processes under high temperatures to adhere more on the surface and withstand heat. Additional factors affecting microbial adherence are presented in **Figure 6.1**.

Elcik *et al.,* (2022) evaluated biofouling development in MD and reported that biofilms formed at 45 ºC consisted of low bacterial concentrations than biofilms formed at 55 ºC and 65 ºC. There was an additional shift in the microbial community on the membrane surface as the feed temperature increased. This resulted in performance declines induced by an increased secretion of EPS. Strategies used for biofouling prevention include membrane cleaning, pretreatment of the feed solution and membrane modification (Mpala *et al.*, 2022). Membrane modification with AgNPs is a useful tool to minimize biofouling. The use of AgNPs does not produce disinfection byproducts that are harmful (Zhou *et al.*, 2018). In this work, the biofouling resistance of the synthesized PVDF membranes was assessed in a MD operation using artificial seawater spiked with a monoculture of *G. stearothermophilus* as the feed stream. *G. Stearothermophilus* is a rod-shaped, gram-positive bacteria thriving at temperatures between 55ºC – 65ºC (Burgess *et al.*, 2017). Widely distributed in the soil, ocean sediment and hot spring, the bacterium is a member of the phylum *Bacillota* (Burgess *et al.*, 2017).

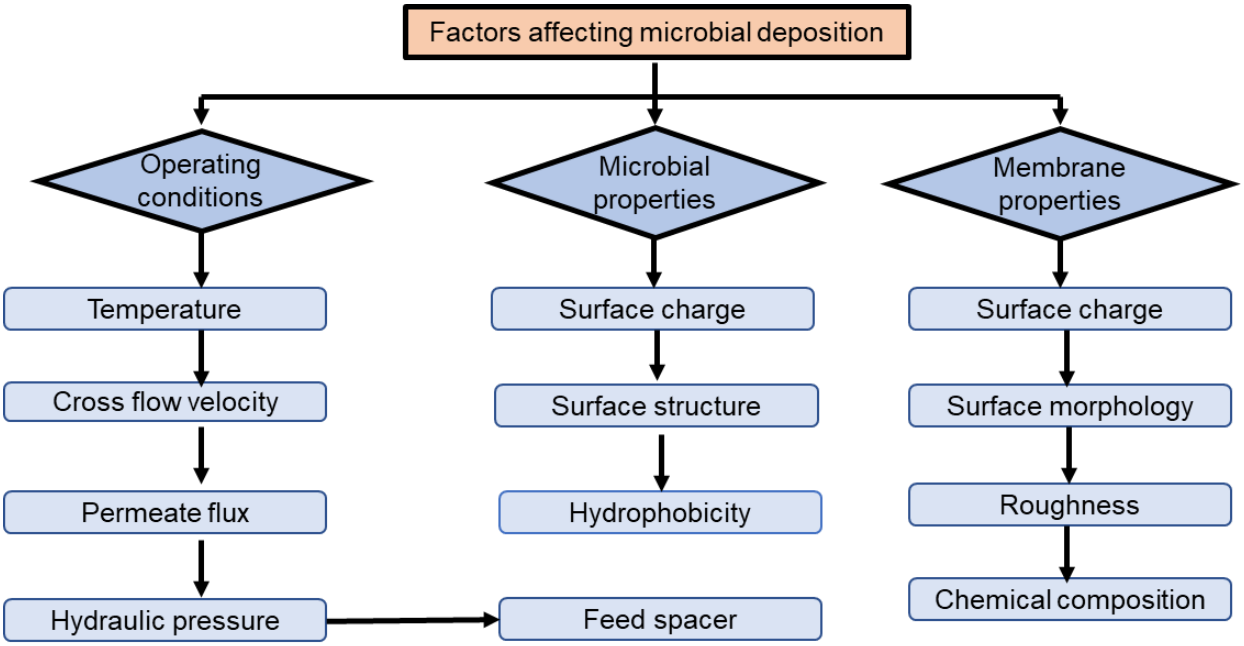

Figure 6.1: Factors affecting microbial deposition (Jiang, Li and Ladewig, 2017a)

6.2 Materials and methods

6.2.1 Materials

Sodium chloride (NaCl, Mw = 58.44 g/mol), magnesium chloride ($MgCl_2$, Mw = 95.21 g/mol), sodium sulphate ($NaSO_4$, Mw = 142.04 g/mol), calcium chloride ($CaCl_2$, Mw = 110.99 g/mol), potassium chloride (KCl, Mw = 74.56 g/mol), and ethanol (ACS reagent, 99%) were procured from Sigma Aldrich. The thermophilic strain of bacteria (*G. Stearothermophilus*) and the 0.5 McFarland standard were purchased from Davies Diagnostics (Pty) Ltd South Africa. Glutaraldehyde (liquid) was procured from Promark Chemicals (South Africa). MHB (Mueller Hinton broth, powder) and MHA (Mueller Hinton agar, powder) were purchased from Sisco Research Laboratories (Pvt) Ltd.

6.2.2 Methods

a) Feed solution composition (including spiking)

Artificial seawater used as the feed stream consisted of 24.5 g/L NaCl, 5.2 g/L $MgCl_2$, 4.1 g/L $NaSO_4$, 1.1 g/L $CaCl_2$, and 0.69 g/L KCl. Distilled water (approx. conductivity of 0.691 µS/cm) was used as the distillate stream. Prior to operation, the feed solution was spiked with *G. Stearothermophilus* and the DCMD operation ran for 24 h. To prepare *G. Stearothermophilus*, the unopened vial containing the bacterium was equilibrated to room temperature (from 4 ºC). Afterwards, one LYFO DISK of *G. Stearothermophilus* was removed aseptically from the vial and placed in sterile water (0.5 mL). The disk was crushed with a sterile swab until the suspension became homogenous. Immediately, the swab was heavily saturated with the suspension and transferred to a MH agar medium. The swab was rolled one-third of the plate and streaked to isolate colonies using a sterile loop. Lastly, the agar plate was incubated at 60 ºC for 24 h. Further growth of the bacterial strain was conducted in MH broth where the 0.5 McFarland standard was used to obtain the optimal density of the cultured bacteria.

b) Membrane anti-microbial performance evaluation using DCMD

Lab-scale DCMD tests were conducted to evaluate the antibacterial activity of the synthesized membranes, where both the feed and distillate solutions were in direct contact with the membrane. The plate and frame module was applied during operation. The solutions were circulated in a counter-current direction at a crossflow velocity of 7 mL/sec using a peristaltic pump (Cole Parmer Ltd, Masterflex). The temperatures of the feed and distillate solutions were set at 60 ºC and 15 ºC, respectively. A water bath and chiller were used to maintain the feed and distillate solution temperatures. Salt rejection efficiency was measured using a conductivity meter and the water flux measured using a weighing balance, and the calculations done using the following equation:

$$R\% = \frac{k_f - k_p}{k_f} * 100\% \quad (1)$$

$$J = {}^{m}/_{A \times t}, \quad (2)$$

where *R%, k_f, k_p J, m, A,* and *t* represent the salt rejection efficiency (%), feed conductivity (µS/cm), distillate conductivity (µS/cm), water flux (kg/m^2/h), distillate mass obtained from the weighing balance (kg), effective membrane area (m^2) and time (h), respectively.

c) Characterization of the membranes

Membrane surface observation for the assessment of bacterial deposition was conducted using SEM. Briefly, a typical membrane was removed from the module after operation, washed with sterilized water, treated with 2.5% glutaraldehyde to facilitate the immobilization of bacteria, and stored at 4ºC in the fridge for analysis. In some instances, membranes were treated with glutaraldehyde followed by dehydration using various concentration of ethanol (25%, 50%, 75% and 100%) and dried.

6.3 Results and discussion

6.3.1 Membrane anti-microbial performance evaluation using DCMD

Water flux and distillate conductivity data obtained during treatment are presented in **Figure 6.2**, below. Herein, artificial seawater spiked with a monoculture of *G. Stearothermophilus* was used as the feed stream. For M1, the water flux decreased considerably as a function of time, with a final decline of 79.3%. Comparatively, minimal decline in water flux was obtained for M1 during preliminary tests (**Figure 5.12**), where there was no bacterial inoculation. Instead, the flux fluctuated over time. The 79.3% decline obtained herein was attributed to the development of a biofouling layer on the feed side of the membrane surface (**Figure 6.3**). As the operation progressed, bacteria adhered on the surface as evident in **Figure 6.4** and secreted EPS, which maintained the upkeep of the stagnant fouling layer. Adhesion of bacteria is caused by many factors, including hydrodynamic conditions, feed solution composition, physiochemical properties of the bacteria and membrane properties (Bogler, Lin and Bar-Zeev, 2017; Jiang, Li and Ladewig, 2017b). Herein, the 60 ºC feed temperature created an optimal growth

temperature for *G. Stearothermophilus*, enhancing interactions of the bacteria with the membrane (Burgess *et al.*, 2017).

In a similar study, Bogler & Bar-Zeev, (2018) sought to understand the impact of *Anoxybacillus sp*. on MD performance under different feed solution temperatures. At 55 ºC, a 78% decrease in water flux was observed, largely ascribed to the favored growth of *Anoxybacillus sp.* at that temperature. It is evident that the optimization of the parameters of operation for each study in MD is highly imperative, as different feed solution compositions affect the process performance differently. Once adhered, these fouling layers induce mass and heat transfer resistance, resulting in a reduction in the driving force of the operation and a decline in operation performance (Elcik *et al.*, 2022). The conductivity of M1, however, increased steadily overtime and peaked at 82 µS/cm, with an excellent salt rejection efficiency of 99.8%. In this instance, the impact of bacterial inoculation on salt rejection efficiency was minimal.

For M2 and M3, the water flux fluctuated considerably with time, albeit with minimal variation. In comparison to preliminary tests, a considerable rise in water flux was obtained for both membranes, where M2 increased by 20.6% (from 0.603 ± 0.157 kg/m^2/hr to 0.760 ± 0.105 kg/m^2/hr) and M3 increased by 19.3% (from 0.557 ± 0.176 kg/m^2/hr to 0.690 ± 0.169 kg/m^2/hr). Due to the concomitant increase in the distillate conductivity, possible membrane wetting may have caused the increase in water flux as M2 peaked at 188.9 µS/cm and M3 at 160.0 µS/cm. A study by Elcik *et al.,* (2022) elucidated biofouling in MD over spatial and thermal gradients. It was reported that membrane wetting occurred (conductivity of 140 ± 7 µS/cm at 65 ºC) during the first few hours of operation but gradually slowed down with time. Herein, wetting was further exacerbated by the low WCA's of M2 and M3, which gave 82.6 ± 0.1º and 83.9 ± 0.6º, respectively. The wetting phenomena is unique to MD and membrane pores should be significantly dry for the salt rejection efficiency of the system to remain high (Rezaei, 2017). Wetting results in overall process failure (Liao, Wang and Fane, 2013). Hence, dealing with fouling may have a positive impact on operation performance as it can also deal with membrane wetting.

For M4, the water flux was stable and did not decrease over time, averaging 0.165 ± 0.038 kg/m^2/hr. Distillate conductivity also remained relatively low with a minimal increase to 47 µS/cm. The insignificant increase in distillate conductivity presented considerable membrane resistance to wetting. Evidently, there was minimal variation between these results and preliminary results. That is, the performance of M4 was maintained, with or without bacteria inoculation. This was attributed to the presence CNC-capped AgNPs which inhibited the deposition of bacteria (**Figure 6.4**) and the subsequent formation of the stagnant layer (**Figure 6.3**).

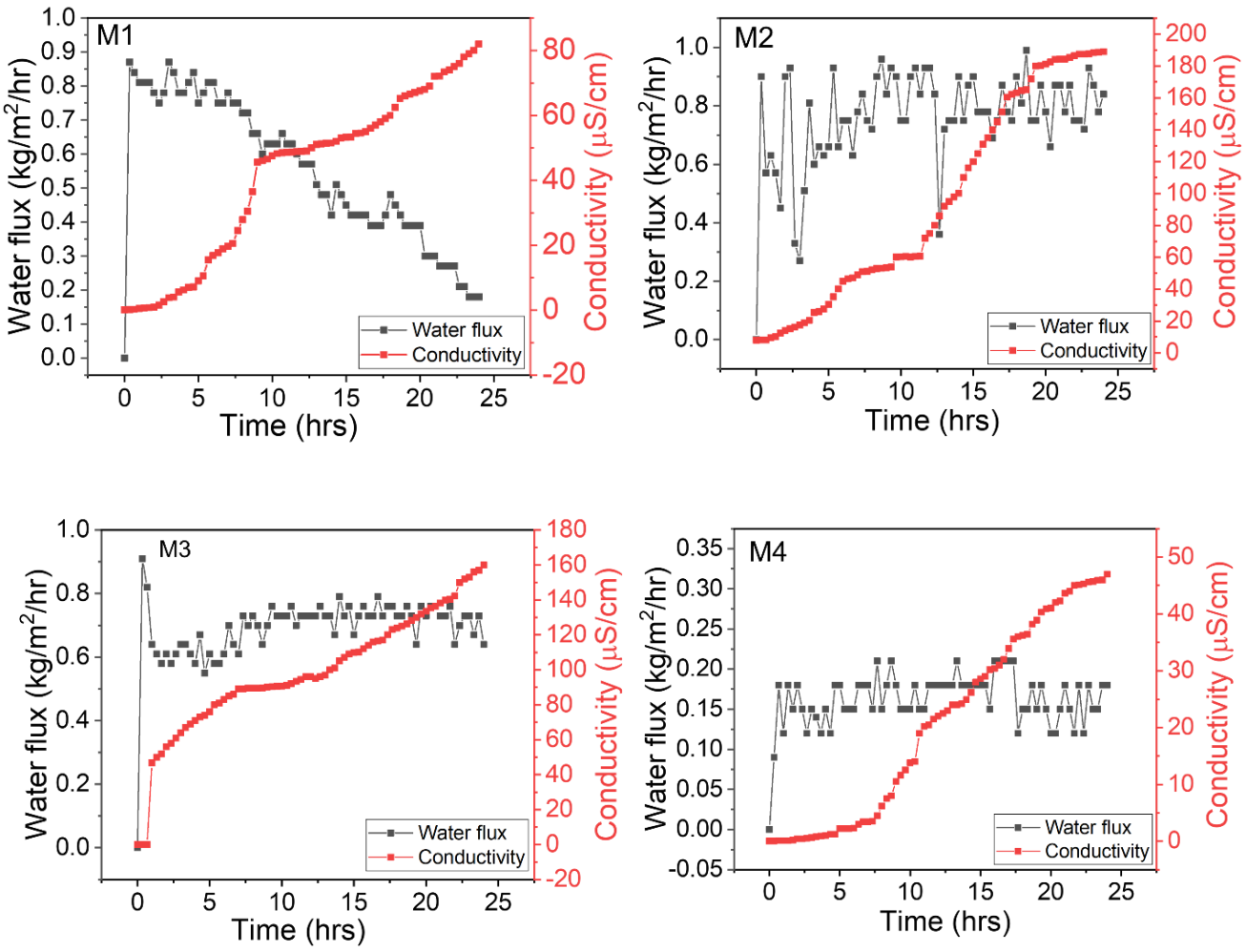

Figure 6.2: Water flux and distillate salinity results for M1, M2, M3 and M4 as obtained from DCMD operations where artificial seawater spiked with *G. Stearothermophilus* was used as the feed stream

6.3.2 Fouled membrane surface morphology analysis

Figure 6.3 illustrates SEM surface morphology images for M1, M2, M3 and M4 following MD process evaluation. The images were taken after the 24 h operation period. It is evident from **Figure 6.3** that unmodified M1 developed a connected cobweb-like microbial mat, largely covering the feed side of the membrane surface. Remarkably, EPS was released by the bacteria, enhancing the inter-connectedness of the fouling layer (Zheng

et al., 2022). A subsequent reduction in water flux resulted (**Figure 6.2**). A reduced production of water flux was attributed to an increase in the mass and heat transfer resistance induced by a rise in the restriction of flow of vapor across the membrane. M2 and M3 also recorded the connected fouling layer but with minimal bacterial growth. Additionally, surface morphology of the membranes changed considerably. For M4, however, no fouling layer was observed on the membrane surface, hence no water flux decline was evident. This was attributed to the modification of PVDF with CNC-capped AgNPs. We note here that the fouling layers displayed in **Figure 6.3** are a fractional representation of the membrane surfaces and do not represent the total fouling layer.

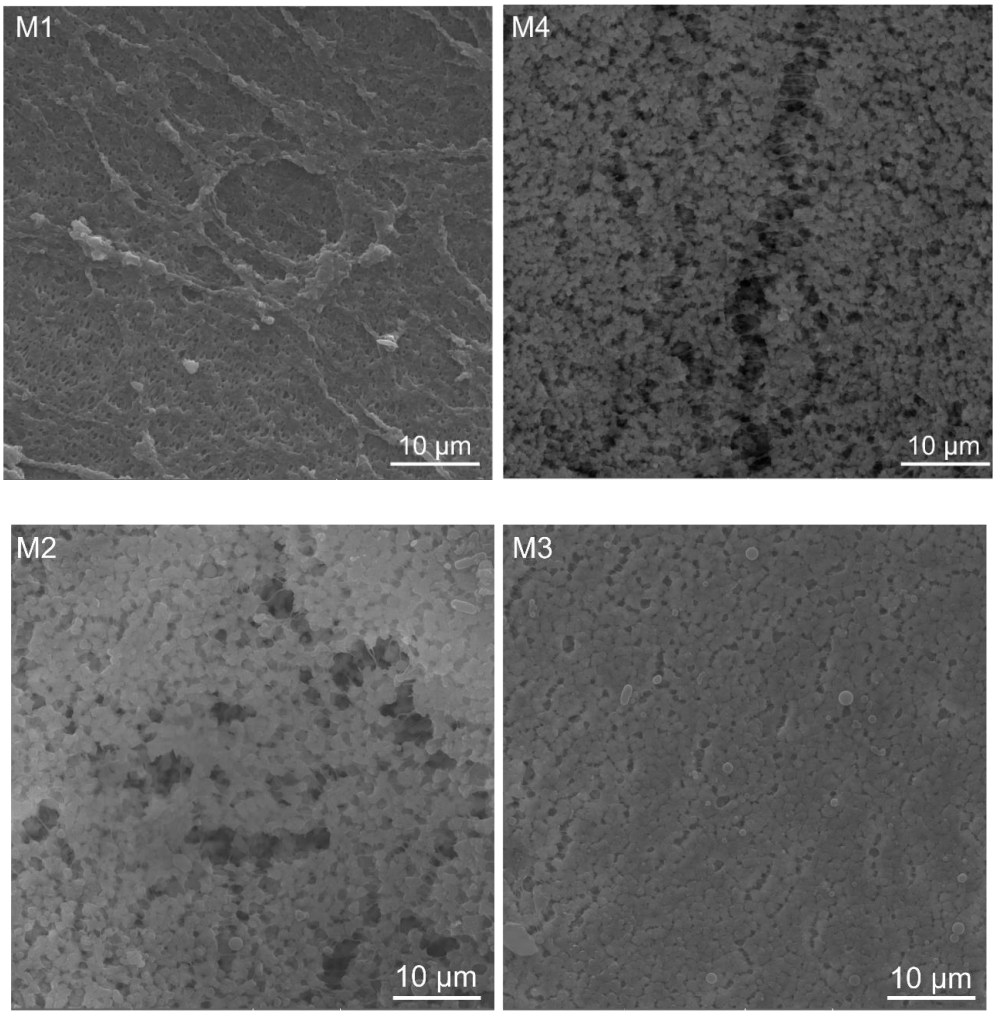

Figure 6.3: SEM images (at 10 µm). for M1, M4 and M2, M3 following DCMD operation

M1 and M4 were chosen for high resolution SEM evaluation of bacterial growth on the membrane surfaces. The SEM micrographs recorded after the 24 h MD experiments are presented in **Figure 6.4**. M1 presented a clear adherence of microbial cells on the surface of the membrane. The shape of the cells was largely rod-shaped, a confirmation of the growth of *G. Stearothermophilus* (Burgess *et al.*, 2017). A significant interaction between the cells was observed, producing a firmly connected layer (**Figure 6.3**). Comparable images were reported by Zheng *et al.,* (2022), who desulfurized wastewater using MD and concomitantly studied microbial distribution and succession on the membrane surface over time. However, M4 presented minimal bacterial growth. This was ascribed to the presence of AgNPs on the surface of the membrane. It is the continuous and steady dissolution of Ag^{+} ions that suppressed thermophilic bacteria from adherence (Qi *et al.*, 2021). As a result, there was no reduction in the water flux produced. The anti-microbial properties of AgNPs have been well-known (Barrios *et al.*, 2020; Xu *et al.*, 2020; Xuan *et al.*, 2020; Ma *et al.*, 2021). Moreover, AgNPs are desirable agents as they do not invoke microbial resistance over time (Susanti *et al.*, 2022), ensuring prolonged retainment of anti-microbial activity over a sustained period of time. In summary, these results display the tremendous potential of AgNPs for biofouling mitigation in water treatment systems for future application. Although considerable inferences were made from this work, the process of fouling (in MD) is time-dependent, and requires substantial operating time to fully comprehend its effect (Choudhury *et al.*, 2019).

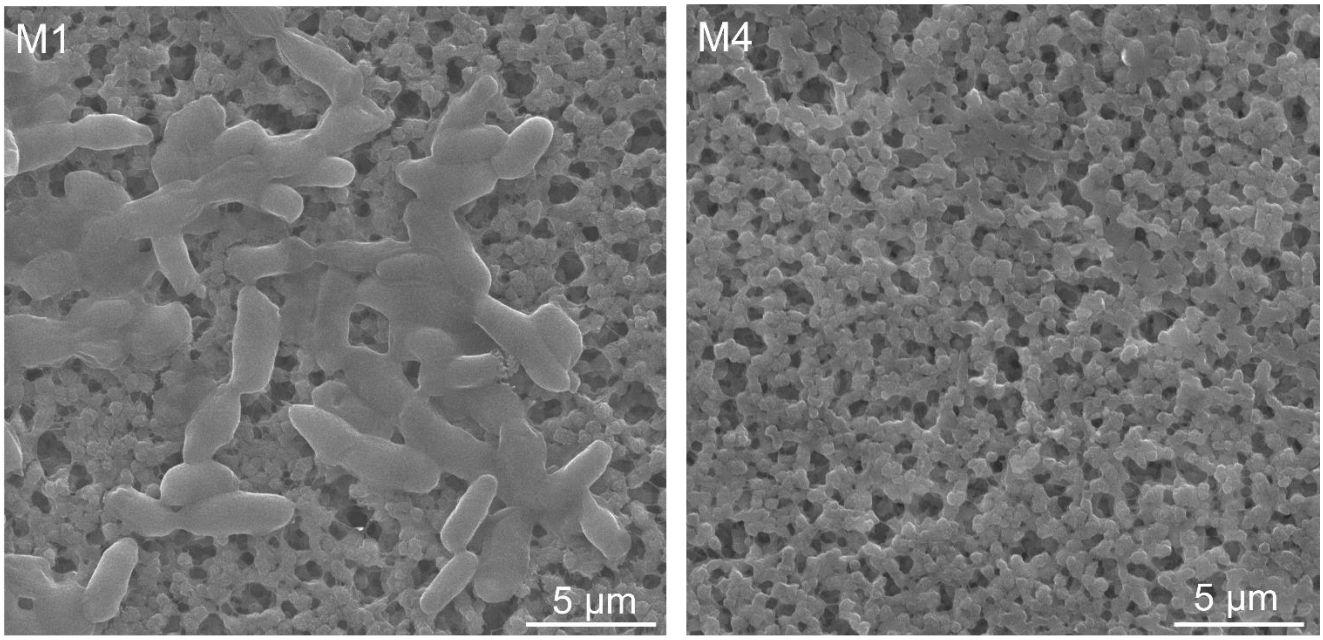

Figure 6.4: SEM images (at 5 µm) for M1 and M4 following DCMD operation

6.4 Conclusion

Herein, the ability of CNC/AgNP-modified PVDF membrane to minimize biofouling in MD was assessed. This was done through spiking the feed stream with *G. stearothermophilus,* a gram-positive thermophilic strain of bacteria. Evidently, CNC/AgNP-modified PVDF membrane largely inhibited bacterial deposition and subsequent fouling layer formation, dissimilar to PVDF whose surface was covered with bacteria and a fouling layer. The water flux of PVDF subsequently decreased overtime while CNC/AgNP-modified PVDF membrane's water flux remained stable. This was attributed to the oxidation of AgNPs on the membrane surface. Overall, membrane modification (using MNPs) is a useful tool to minimize biofouling in MD systems.

6.5 References

1. Barrios, A. C. *et al.* (2020) 'Prolonging the antibacterial activity of nanosilver-coated membranes through partial sulfidation', *Environmental Science: Nano*, 7(9), pp. 2607–2617. doi: 10.1039/d0en00300j.
2. Bogler, A. and Bar-Zeev, E. (2018) 'Membrane Distillation Biofouling: Impact of Feedwater Temperature on Biofilm Characteristics and Membrane Performance', *Environmental Science and Technology*, 52(17), pp. 10019–10029. doi: 10.1021/acs.est.8b02744.
3. Bogler, A., Lin, S. and Bar-Zeev, E. (2017) 'Biofouling of membrane distillation, forward osmosis and pressure retarded osmosis: Principles, impacts and future directions', *Journal of Membrane Science*, 542, pp. 378–398. doi: 10.1016/j.memsci.2017.08.001.
4. Burgess, S. A. *et al.* (2017) 'Insights into the Geobacillus stearothermophilus species based on phylogenomic principles', *BMC Microbiology*, 17(1), pp. 1–12. doi: 10.1186/s12866-017-1047-x.
5. Choudhury, M. R. *et al.* (2019) 'Fouling and wetting in the membrane distillation driven wastewater reclamation process – A review', *Advances in Colloid and Interface Science*, 269, pp. 370–399. doi: 10.1016/j.cis.2019.04.008.
6. Costa, F. C. R. *et al.* (2021) 'Biofouling in membrane distillation applications - a review', *Desalination*, 516. doi: 10.1016/j.desal.2021.115241.
7. Elcik, H. *et al.* (2022) 'Elucidating biofouling over thermal and spatial gradients in seawater membrane distillation in hot climatic conditions', *Water Research*, 223(May), p. 118983. doi: 10.1016/j.watres.2022.118983.
8. Jiang, S., Li, Y. and Ladewig, B. P. (2017a) 'A review of reverse osmosis membrane fouling and control strategies', *Science of the Total Environment*, 595, pp. 567–583. doi: 10.1016/j.scitotenv.2017.03.235.
9. Jiang, S., Li, Y. and Ladewig, B. P. (2017b) 'A review of reverse osmosis membrane fouling and control strategies', *Science of the Total Environment*, 595, pp. 567–583. doi: 10.1016/j.scitotenv.2017.03.235.
10. Liao, Y., Wang, R. and Fane, A. G. (2013) 'Engineering superhydrophobic surface

on poly(vinylidene fluoride) nanofiber membranes for direct contact membrane distillation', *Journal of Membrane Science*, 440, pp. 77–87. doi: 10.1016/j.memsci.2013.04.006.

11. Ma, Z. *et al.* (2021) 'In-situ synthesis and immobilization of silver nanoparticles on microfibrillated cellulose for long-term antibacterial applications', *Cellulose*, 28(10), pp. 6287–6303. doi: 10.1007/s10570-021-03941-4.
12. Mpala, T. J. *et al.* (2022) 'Biofouling phenomena in membrane distillation: mechanisms and mitigation strategies', *Environmental Science: Advances*, (2013). doi: 10.1039/d2va00161f.
13. Qi, L. *et al.* (2021) 'Polymeric membrane ion-selective electrodes with anti-biofouling properties by surface modification of silver nanoparticles', *Sensors and Actuators, B: Chemical*, 328(October 2020), p. 129014. doi: 10.1016/j.snb.2020.129014.
14. Rezaei, M. (2017) 'Wetting Prevention in Membrane Distillation'. Available at: https://epub.jku.at/obvulihs/content/titleinfo/2343597.
15. Susanti, D. *et al.* (2022) 'Natural Products-Based Metallic Nanoparticles as Antimicrobial Agents', *Frontiers in Pharmacology*, 13(June), pp. 1–14. doi: 10.3389/fphar.2022.895616.
16. Xu, C. *et al.* (2020) 'Cellulose nanocrystal/silver (CNC/Ag) thin-film nanocomposite nanofiltration membranes with multifunctional properties', *Environmental Science: Nano*, 7(3), pp. 803–816. doi: 10.1039/c9en01367a.
17. Xuan, L. *et al.* (2020) 'In situ synthesizing silver nanoparticels by bio-derived gallic acid to enhance antimicrobial performance of PVDF membrane', *Separation and Purification Technology*, 251, p. 117381. doi: 10.1016/j.seppur.2020.117381.
18. Zheng, L. *et al.* (2022) 'Insight into the microbial distribution and succession and biofouling mechanism in membrane distillation for desulfurization wastewater treatment', *Chemical Engineering Journal*, 428, p. 131097. doi: 10.1016/j.cej.2021.131097.
19. Zhou, Y. *et al.* (2018) 'Anti-biofilm AgNP-polyaniline-polysulfone composite membrane activated by low intensity direct/alternating current', *Environmental Science: Water Research and Technology*, 4(10), pp. 1511–1521. doi:

10.1039/c8ew00259b.

20. Zodrow, K. R. *et al.* (2014) ‘Biofouling and Microbial Communities in Membrane Distillation and Reverse Osmosis’, *Environmental Science and Technology*, 48(22), pp. 13155–13164. doi: 10.1021/es503051t.

Chapter 7: Overall conclusion and future work

7.1 Overall Conclusion

MD is an emerging membrane separation technology harnessed to recover fresh water from contaminated wastewaters. Although possessing attractive features, its industrial application is still limited by several factors, including fouling. In this study, PVDF was modified with PVP, *f*-CNTs and CNC-capped AgNPs to improve biofouling resistance while retaining excellent membrane properties for high MD process performance. From the findings of this study, the following conclusion can be drawn:

1. The synthesis of AgNPs via chemical reduction on the surface of CNCs was achieved successfully, with excellent dispersity and stability. The OH functional groups of CNCs played a critical role during adsorption and afforded AgNPs of 13.3 ± 3.94 nm average particle size. The presence of AgNPs increased the overall thermal stability of the nanocomposite (CNC-capped AgNPs).
2. Synthesis of the functionalized PVDF membranes was achieved successfully, with PVP, *f*-CNTs, and CNC-capped AgNPs addition affording an enhancement in membrane properties, including improved surface roughness, contact angle, and tensile strength, properties specifically desired for MD membranes.
3. Both CNC-capped AgNPs and CNC/AgNP-modified PVDF membrane displayed excellent anti-microbial activity against *E. Coli*, *P. Aeruginosa*, *S. Aureus*, *S. Epidermis*, *and S. Saprophyticus* (*in vitro*), mesophilic strains which have the potential to initiate biofouling.
4. During water desalination, CNC/AgNP-modified PVDF membrane minimized the adhesion of thermophilic *G. Stearothermophilus*, even under conditions that promote the growth of the bacteria. Despite producing low water fluxes, the anti-microbial properties of the membrane were excellent, thus opening new research directions for biofouling eradication in MD systems.

7.2 Future work

1. Since hydrophobicity is a requirement for MD membranes, exploring other hydrophobic nanoparticles capable of reducing and caping AgNPs would be imperative. Although CNCs presented strong capping properties, they are hydrophilic, and thus compromise the process performance of MD. Hydrophobic NPs will not only improve the overall membrane hydrophobicity but will also ensure high salt rejection with simultaneous biofouling minimization.

2. Experimental work elucidating the mechanisms of microbial deposition on membrane surfaces supported by mathematical simulations is an alternative dimension to consider. This will shed light into innovative solutions toward the minimization of bacterial deposition and afford minimal EPS secretion, further lessening the propensity for biofilm formation.

3. Halophilic and salt-resistant strains further need to be studied in-detail in MD biofouling tests due to their high prevalence in seawater. This will ensure better realization of the MD technology and increase its consideration for the sustainable production of fresh water. In this work, only mesophilic and thermophilic strains were assessed.

4. During the design and fabrication of MD membrane modules (either flat sheet or hollow fibre), silver nanoparticles can be incorporated within the process to ensure system improvement against bacterial growth. This may prevent bacteria from thriving during separation and hence prevent biofouling.

5. The performance of CNC/AgNP-modified PVDF membrane can be evaluated with real seawater samples to ascertain the retainment of its anti-microbial performance, conducting fouling tests for a minimum of at least 600 hrs since fouling is a time-dependent phenomenon.

6. Lastly, the investigation of the operational stability of the CNC/AgNP-modified PVDF membrane for MD desalination of seawater to understand its potential applicability commercially.